

COMPENSATION METHODS FOR QUASI-STATIC
ACCELERATION SENSITIVITY OF MEMS GYROSCOPES

A THESIS SUBMITTED TO
THE GRADUATE SCHOOL OF NATURAL AND APPLIED SCIENCES
OF
MIDDLE EAST TECHNICAL UNIVERSITY

BY

HASAN DOĞAN GAVCAR

IN PARTIAL FULFILLMENT OF THE REQUIREMENTS
FOR
THE DEGREE OF MASTER OF SCIENCE
IN
ELECTRICAL AND ELECTRONICS ENGINEERING

NOVEMBER 2014

Approval of the thesis:

**COMPENSATION METHODS FOR QUASI-STATIC
ACCELERATION SENSITIVITY OF MEMS GYROSCOPES**

submitted by **HASAN DOĞAN GAVCAR** in partial fulfillment of the requirements
for the degree of **Master of Science in Electrical and Electronics Engineering**
Department, Middle East Technical University by,

Prof. Dr. Gülbin Dural
Dean, Graduate School of **Natural and Applied Sciences**

Prof. Dr. Gönül Turhan Sayan
Head of Department, **Electrical and Electronics Eng.**

Prof. Dr. Tayfun Akın
Supervisor, **Electrical and Electronics Eng. Dept., METU**

Assist. Prof. Dr. Kıvanç Azgın
Co-Supervisor, **Mechanical Eng. Dept., METU**

Examining Committee Members

Assoc. Prof. Dr. Haluk Kulah
Electrical and Electronics Eng. Dept., METU

Prof. Dr. Tayfun Akın
Electrical and Electronics Eng. Dept., METU

Assist. Prof. Dr. Kıvanç Azgın
Mechanical Eng. Dept., METU

Dr. Fatih Koçer
Electrical and Electronics Eng. Dept., METU

Dr. Said Emre Alper
MEMS Research and Application Center, METU

Date:

I hereby declare that all information in this document has been obtained and presented in accordance with academic rules and ethical conduct. I also declare that, as required by these rules and conduct, I have fully cited and referenced all referenced material and results that are not original to this work.

Name, Surname: Hasan Dođan Gavcar

Signature:

ABSTRACT

COMPENSATION METHOD FOR QUASI-STATIC ACCELERATION SENSITIVITY OF MEMS GYROSCOPES

Gavcar, Hasan Dođan

M.S., Department of Electrical and Electronics Engineering

Supervisor: Prof. Dr. Tayfun Akın

Co-supervisor: Assist. Prof. Dr. Kıvanç Azgın

November 2014, 122 pages

This thesis presents the quasi-static acceleration compensation methods for a fully decoupled MEMS gyroscope. These methods are based on the utilization of the amplitude difference information between the residual quadrature signals on the differential sense mode electrodes to sense the static acceleration acting on the sense mode of the gyroscope. There are three different quasi-static acceleration compensation methods presented in this thesis. In the first method, the static acceleration is measured by comparing the amplitudes of the out of phase sustained residual quadrature signals. By using the experimental relation between the rate and acceleration outputs, the quasi-static acceleration sensitivity of the gyroscope is mitigated. This method requires the additional process of data collection. In the second method, in addition to the circuit proposed in the first method, a closed loop controller is implemented in the acceleration compensation system to suppress the effect of the acceleration. The generated feedback voltage is applied to the sense mode electrodes by using the non-inverting inputs of the sense mode preamplifiers.

The advantage of this method compared to the first one is that it does not require any additional data process thanks to the closed loop controller. However, this method cannot completely suppress the quasi-static acceleration of the gyroscope. Moreover, changing the voltage of the non-inverting inputs of the preamplifiers may affect the operation of all other control loops. In the third method, the additional acceleration cancellation electrodes are utilized in the mechanical design of the gyroscope. This method overcomes the problems encountered in the second acceleration compensation method. This study mainly focuses on the third acceleration compensation method which provides the best result. Therefore, a single-mass fully decoupled gyroscope including the dedicated acceleration cancellation electrodes is designed. FEM simulations are performed to determine the mode shapes and mode resonance frequencies of the designed gyroscope. The designed gyroscopes are fabricated using the modified silicon-on-glass (SOG) process and are packaged at the wafer level. The closed loop controllers are designed for the drive amplitude control, force-feedback, quadrature cancellation, and acceleration cancellation loops and are implemented on a printed circuit board (PCB). The acceleration compensation system consisting of vacuum packaged gyroscope and controller modules is populated on the same PCB, and the system level tests are performed.

Measurements show that the proposed acceleration compensation system operates as expected. Test results demonstrate that the g-sensitivity of the studied gyroscopes are substantially reduced from $0.31^{\circ}/s/g$ to $0.025^{\circ}/s/g$, and the effect of the static acceleration is highly-suppressed up to 12 times with the use of the third compensation method proposed in this work. Moreover, the nonlinearity in the scale factor is improved from 0.53% to 0.36% for $\pm 600^{\circ}/s$ range for centrifugal accelerations as much as 0.5g. Furthermore, the proposed acceleration compensation methods do not deteriorate the bias and noise performances of the gyroscopes.

To conclude, the proposed acceleration compensation methods improves the g-sensitivity of MEMS gyroscope by using the control electronics rather than employing complex mechanical design.

Keywords: MEMS Gyroscope, Acceleration Sensitivity, G-Sensitivity, Acceleration Sensitivity Compensation Techniques, MEMS Fabrication.

ÖZ

MEMS DÖNÜÖLÇERİN DURAĞAN İVME DUYARLILIĞINI AZALTMA YÖNTEMLERİ

Gavcar, Hasan Dođan

Yüksek Lisans, Elektrik ve Elektronik Mühendisliđi Bölümü

Tez Yöneticisi: Prof. Dr. Tayfun Akın

Ortak Tez Yöneticisi: Assist. Prof. Dr. Kıvanç Azgın

Kasım 2014, 122 sayfa

Bu tez, literatürde ilk defa, bir MEMS dönüölçerin okuma parmak yapıları üzerindeki zıt fazlı artık ofset hatası sinyallerinin genliklerini karşılaştırarak dönüölçerin okuma eksenine etkileyen ivmeyi algılamaya dayalı dönüölçerin durađan ivme duyarlılıđını azaltma yöntemleri sunmaktadır. Bu çalışmada, üç farklı g-duyarlılıđı düzeltme yöntemi önerilir. İlk yöntemde, zıt fazlı artık ofset hatası sinyallerinin genlik farkına bakarak dönüölçerin okuma eksenine etkileyen ivmeyi algılayan bir ivme algılama devresi kullanılır. Test sırasında, dönüölçerin ivme ve dönü verileri eş zamanlı olarak toplanır. Daha sonra bu iki veri arasındaki ilişki kurularak, ivmenin dönü çıkışı üzerindeki etkisi bilgisayar ortamında düzeltilir. İkinci yöntemde, birinci yöntemde önerilen devreye ek olarak kapalı-döngü kontrol devresi eklenir. Bu yöntemde, okuma önelektronisindeki yükselticilerin pozitif girişı vasıtasıyla okuma parmak yapılarına geri besleme uygulanır. Bu yöntemde amaç, dönüölçerin durađan ivmeye olan duyarlılıđını dönüölçerin çalışması sırasında azaltmaktır. Bu yöntem, dönüölçerin g-duyarlılıđını belli bir noktaya kadar

azaltmasına rağmen, ivme algılama yönteminin çalışma prensibinden dolayı bu hatayı tamamen ortadan kaldıramamaktadır. Ayrıca, okuma parmak yapılarına geri besleme uygulamak, diğer kontrol devrelerinin de çalışmasını etkilemektedir. İkinci yöntemde belirtilen sorunları çözmek için, üçüncü yöntemde ivmenin etkisini ortadan kaldırmak için geri besleme, özelleşmiş ivme durdurma parmak yapılarına uygulanır. Bu yöntem, algılama eksenine etkiyen ivme kuvvetini durdurmak için özel olarak tasarlanmış ivme durdurma parmak yapılarının kullanımını gerektirir. Bu çalışmada, özellikle son yöntem üzerinde yoğunlaşmıştır. Bu sebeple, özel ivme durdurma parmak yapıları içeren tek kütleli, tamamen etkileşimsiz bir dönüölçer tasarlanmıştır. Tasarlanan dönüölçerin mod analizi ve rezonans frekansları, sonlu eleman analiz yöntemi kullanılarak belirlenmiştir. Bu dönüölçerler, değiştirilmiş SOG üretim tekniği ve pul seviyesinde paketlenme yöntemi kullanılarak üretilmiştir. Bir sonraki adımda, sürüş genlik kontrol, güç geri besleme, ofset giderme ve ivme duyarlılığı azaltma işlemleri için kapalı döngü kontrol devreleri tasarlanmıştır. Bu devreler, duyarğa paketi ile bir baskı devre kartı (PCB) üzerinde birleştirilmiş ve sistem seviyesinde testler yürütülmüştür.

Testler, önerilen durağan ivme duyarlılığı azaltma yöntemlerinin istenilen şekilde çalışmakta olduğunu göstermiştir. Test sonuçları, önerilen üçüncü ivme duyarlılığı azaltma devre yapısını kullanarak, çalışılan MEMS dönüölçerin g-duyarlılığının $0.31^{\circ}/s/g$ 'den $0.025^{\circ}/s/g$ 'e düştüğünü ve durağan ivmenin etkisinin 12 kata kadar azaldığını göstermektedir. Ayrıca, dönüölçerin orantı katsayısındaki doğrusalsızlık, $\pm 600^{\circ}/s$ sınırındaki merkezkaç ivme testi için önerilen yöntem ile 0.53% 'den 0.36% 'a düşmektedir. Bunun dışında, önerilen ivme duyarlılığı azaltma yöntemin dönüölçerin performansını kötüleştirecek yönde bir etkisi olmadığı gözlemlenmiştir.

Sonuç olarak, önerilen durağan ivme duyarlılığı azaltma yöntemleri, karmaşık yapılı mekanik tasarımlar gerektirmeden, dönüölçerin kontrol elektroniğini değiştirerek sensörün durağan ivmeye olan duyarlılığını sensörün çalışma sırasında azaltmaktadır.

Anahtar Kelimeler: MEMS Dönüölçer, İvme Duyarlılığı, G-Duyarlılığı, İvme Duyarlılığı Azaltma Yöntemleri, MEMS Üretimi.

To My Family

ACKNOWLEDGEMENTS

First of all, I would like to thank to my thesis advisor Prof. Dr. Tayfun Akın for his support, guidance, and encouragement during my graduate studies. It is a great chance for me to work in his MEMS research group.

I also would like to thank to Assist. Prof. Kıvanç Azgın and Dr. Said Emre Alper for sharing their deep knowledge and experiences in all phases of this research. Without their guidance and helps, this study could not exist.

I would like to express my gratitude to M. Mert Torunbalcı, the master of process, for his worthy helps during gyroscope fabrication and endless discussions about life. Special thanks to Soner Sönmezoğlu, my smart research partner, for his valuable suggestions and helps in tests of the acceleration compensation system. I would like also thank Ferhat Yeşil, the master of readout, for his valuable discussions and suggestions during the design of the control electronics.

I would like to express my gratitude to Gülşah Demirhan, Yunus Terzioğlu, Ulaş Aykutlu, Serdar Tez, and Talha Köse for their helps in the fabrication phases of this study and fruitful discussions about the controller electronic design. I am very grateful to METU-MEMS center staff for their helps during the gyroscope fabrication, especially Orhan Şevket Akar. Special thanks to Selçuk Keskin, Ozan Ertürk, Ramazan Çetin, Başak Kebapçı and Osman Aydın for their friendship. Moreover, I would like to thank all members of the METU-MEMS VLSI research group for providing a nice research environment.

I would express my deepest gratitude to my parents for their endless support, love and encouragement throughout my whole life.

TABLE OF CONTENTS

ABSTRACT	v
ÖZ	vii
ACKNOWLEDGEMENTS	x
TABLE OF CONTENTS	xi
LIST OF FIGURES	xiv
LIST OF TABLES	xix
CHAPTERS	
1 INTRODUCTION	1
1.1 Operation Principle of MEMS Vibratory Gyroscopes	3
1.2 Metrics of MEMS Gyroscopes and Their Application Areas	4
1.3 Overview of the Micromachined Vibratory Gyroscopes	7
1.4 Gyroscopes Studied in This Thesis	9
1.5 Overview of Acceleration Sensitivity of MEMS Gyroscope and Compensation Techniques	12
1.6 Research Objectives and Thesis Organization	14
2 VIBRATORY GYROSCOPE THEORY AND MODELLING	17
2.1 Mechanical Model of the Gyroscope	17
2.1.1 Drive Mode Dynamics	19
2.1.2 Coriolis Coupling and Sense Mode Dynamics	20
2.2 Design of MEMS Vibratory Gyroscope and Model Parameters	23
2.2.1 Mechanical Spring Constant Estimation	23
2.2.2 Mass and Damping Factor Estimation	24

2.3	Electrostatic Actuation Using Parallel Plate Capacitor	24
2.4	Capacitive Sensing	25
2.5	Electrostatic Spring Effect.....	26
2.6	Quasi-static Acceleration Sensitivity.....	27
2.6.1	Effect of Static Acceleration on the Sense-Mode Electrodes	28
2.6.2	Effect of Static Acceleration on the Force-feedback Electrodes	30
2.6.3	Effect of Static Acceleration on the Quadrature Cancellation Electrodes and Sense Mode Springs	32
2.6.4	Design of Acceleration Cancellation Electrodes.....	34
2.7	Finite-Element Simulations	36
2.7.1	Modal Analysis	36
2.8	Summary.....	39
3	CONTROL ELECTRONICS FOR MEMS GYROSCOPES	41
3.1	Front-End Electronics.....	41
3.2	Drive Mode Controller Design for MEMS Gyroscope	43
3.3	Design of Closed Loop Rate Sensing Mechanism	51
3.4	Design of Quadrature Control Electronics	58
3.5	Design of Acceleration Sensing and Compensation Electronics.....	64
3.5.1	Open Loop Acceleration Compensation Electronics	65
3.5.2	Closed Loop Acceleration Cancellation Electronics Using Sense Mode Electrodes.....	69
3.5.3	Closed Loop Acceleration Cancellation Electronics Using Acceleration Cancellation Electrodes.....	73
4	FABRICATION OF MEMS GYROSCOPES	77
4.1	Fabrication of Sensor Wafer Using Modified SOG (M-SOG) Process.....	78
4.2	Wafer Level Hermetic Encapsulation of MEMS Gyroscopes using SOI Cap Wafers with Vertical Feedthroughs.....	82
4.3	Fabrication Results	85

4.4	Summary	88
5	TEST RESULTS.....	89
5.1	Characterization and Test Procedure of Gyroscopes.....	89
5.2	System Level Test Setup for the Acceleration and Performance Tests of the Studied MEMS Gyroscopes.....	92
5.3	Test Results of the Studied MEMS Gyroscopes for Static Acceleration Tests	93
5.4	Test Results of the Studied MEMS Gyroscopes for Centrifugal Acceleration Tests	102
5.5	Test Results of the Studied MEMS Gyroscopes for Performance Tests...	104
5.6	Summary	108
6	CONCLUSIONS AND FUTURE WORK	111
	REFERENCES.....	117

LIST OF FIGURES

FIGURES

Figure 1.1: Inertial frame showing Coriolis force.....	3
Figure 1.2: A conceptual view of the vibratory gyroscope.	4
Figure 1.3: Simplified view of the single-mass fully decoupled MEMS gyroscope without the dedicated acceleration cancellation electrodes studied in the scope of this thesis [30].	9
Figure 1.4: Simplified view of the single-mass fully decoupled MEMS gyroscope with the dedicated acceleration cancellation electrodes studied in the scope of this thesis.....	11
Figure 2.1: Three basic decoupling mechanisms: (a) simplest decoupling configuration with no special decoupling treatment, (b) improved decoupling configuration and (c) fully-decoupled configuration.	18
Figure 2.2: Conceptual view of the differential sense-mode electrodes under the conditions of (a) zero and (b) static acceleration. The sense mode output current increases in one side and decreases in the other under the static acceleration.	29
Figure 2.3: Conceptual view of the force-feedback electrodes under the conditions of (a) zero and (b) static acceleration.	31
Figure 2.4: Conceptual view of the quadrature cancellation electrodes under the conditions of (a) zero and (b) static acceleration.	33
Figure 2.5: Configuration of the acceleration cancellation electrodes.....	34
Figure 2.6: Mode shape for drive mode.	37
Figure 2.7: Mode shape for sense mode.....	38
Figure 2.8: Mode shape for the closest undesired higher order mode at 24.6 kHz....	38
Figure 3.1: Schematic of the transimpedance amplifier implemented in this study. .	42
Figure 3.2: Block diagram of the closed loop drive mode controller.	44
Figure 3.3: Simplified view of the drive mode resonance test schematic.....	45
Figure 3.4: Bode diagram of the drive mode open loop transfer function.	48
Figure 3.5: Step response of the closed loop drive mode controller.	49

Figure 3.6: SIMULINK model of the closed loop drive mode control electronics for the sample gyroscope.	50
Figure 3.7: Drive pick signal obtained using the realistic SIMULINK model of the drive mode control electronics.	50
Figure 3.8: Block diagram of the closed loop sense mode controller for the mismatch operation.	52
Figure 3.9: Bode diagram of the sense mode open loop transfer function.	54
Figure 3.10: Step response of the closed loop sense mode controller.	55
Figure 3.11: SIMULINK model of the closed loop sense mode control electronics for the sample gyroscope.	56
Figure 3.12: Settling behavior of the gyroscope rate output in response to $1^\circ/\text{s}$ angular rate input.	56
Figure 3.13: Transient behavior of the sense pick signal in response to $1^\circ/\text{s}$ angular rate input.	57
Figure 3.14: Response of the gyroscope rate output to a time varying rate which has amplitude of $1^\circ/\text{s}$	58
Figure 3.15: Block diagram of the closed loop quadrature cancellation controller for the mismatch operation.	59
Figure 3.16: Bode diagram of the open loop quadrature control electronics.	61
Figure 3.17: Step response of the closed loop quadrature cancellation controller.	61
Figure 3.18: SIMULINK model of the closed loop quadrature cancellation control electronics for the sample gyroscope.	62
Figure 3.19: Transient behavior of the sense pick signal in the presence of the quadrature error and closed loop quadrature control electronics.	63
Figure 3.20: Applied quadrature force to suppress the quadrature error exists in the system.	63
Figure 3.21: Block diagram of the acceleration sensing electronics for the mismatch operation.	65
Figure 3.22: SIMULINK model of the open loop acceleration sensing circuit with the force-feedback and quadrature cancellation loops.	67
Figure 3.23: Transient behavior of the acceleration output which is picked from the low pass filter output of the acceleration sensing circuit as response to 1 g acceleration using the first acceleration compensation method.	68

Figure 3.24: Transient behavior of the sense mode displacement which shifts when the 1g acceleration is applied using the first acceleration compensation method.....	69
Figure 3.25: Block diagram of the closed loop acceleration cancellation electronics which utilizes the sense mode electrodes for the generation of the acceleration cancellation voltage for the mismatch operation.....	70
Figure 3.26: SIMULINK model of closed loop acceleration compensation circuit which utilizes the sense mode electrodes for the generation of the acceleration cancellation voltage.....	71
Figure 3.27: Transient behavior of the acceleration controller output as response to 1 g acceleration using the second acceleration compensation method.	72
Figure 3.28: Transient behavior of the sense mode displacement as response to 1 g acceleration using the second acceleration compensation method.	72
Figure 3.29: Block diagram of the closed loop acceleration cancellation electronics which employs the dedicated electrodes for the generation of the acceleration cancellation voltage for the mismatch operation.....	73
Figure 3.30: SIMULINK model of closed loop acceleration compensation circuit which employs the dedicated electrodes for the generation of the acceleration cancellation voltage.....	74
Figure 3.31: Transient behavior of the acceleration controller output as response to 1 g acceleration using the third acceleration compensation method.	75
Figure 3.32: Transient behavior of the sense mode displacement for acceleration compensation method. In this method, the closed loop controller completely eliminates the effect of the static acceleration on the sense mode displacement.	75
Figure 4.1: Empty glass wafer.....	79
Figure 4.2: Anchor formation.....	79
Figure 4.3: Formation of the electrical interconnects	80
Figure 4.4: Empty SOI wafer	80
Figure 4.5: Shallow etch on the device layer	80
Figure 4.6: Formation of the sensor structure	81
Figure 4.7: Anodic bonding of glass and SOI wafers	81
Figure 4.8: Release of the device structure after anodic bonding	81
Figure 4.9: Empty SOI cap wafer.....	82
Figure 4.10: Formation of the via openings on the handle layer.....	83
Figure 4.11: Formation of the wire bonding pads	83

Figure 4.12: Formation of the vertical feedthroughs and sealing walls on the device layer.....	83
Figure 4.13: Getter deposition.....	84
Figure 4.14: Anodic/Eutectic bonding of cap wafer and sensor wafer for packaging.....	84
Figure 4.15: Final view of the wafer level vacuum packaged sensor wafer	84
Figure 4.16: SEM pictures of (a) double-folded, (b) half-folded, and (c) clamped guided springs after the fabrication.....	85
Figure 4.17: SEM pictures of (a) sense, (b) quadrature, and (c) acceleration cancellation electrodes after the fabrication.....	86
Figure 4.18: SEM picture of the fabricated single-mass fully-decoupled gyroscope including the acceleration cancellation electrodes.	87
Figure 4.19: SEM picture of the cross sectional view of the packaged sensor.....	88
Figure 5.1: Resonance test set-up for the die level gyroscope test.	90
Figure 5.2: Gyroscope integrated with the front-end electronics on the hybrid glass substrate.....	91
Figure 5.3: Test setup for the system level tests.	93
Figure 5.4: (a) Schematic and (b) actual views of test setup for the static acceleration tests on the rotation table.....	94
Figure 5.5: Measured (blue one) and compensated (blue-dashed one) rate outputs, and acceleration output (red one) as a function of the rotation angle for the gyroscope (E02) using the compensation Method-1.	96
Figure 5.6: Rate outputs without (blue one) and with (blue-dashed one) acceleration cancellation circuit, and acceleration controller output (red one) as a function of the rotation angle for the gyroscope (H02) using the compensation Method-2.....	97
Figure 5.7: Rate outputs without (blue one) and with (blue-dashed one) acceleration cancellation circuit, and acceleration controller output (red one) as a function of the rotation angle for the gyroscope (0803) using the compensation Method-3.	99
Figure 5.8: Rate outputs without (blue one) and with (blue-dashed one) acceleration cancellation circuit, and acceleration controller output (red one) as a function of the rotation angle for the gyroscope (1207) using the compensation Method-3.	99
Figure 5.9: G-sensitivity of the gyroscope (1207) as a function of the quadrature controller set voltage using Method-3.....	101
Figure 5.10: (a) Schematic and (b) actual views of test setup for the centrifugal acceleration tests on the rate table.....	102

Figure 5.11: Rate output responses of the gyroscope (1207) to the angular rate in the centered and off-centered position on the rate table using the acceleration compensation Method-3.....	103
Figure 5.12: A typical Allan Variance graph.	104
Figure 5.13: Allan Variance graph of the gyroscope (1207) with and without the acceleration cancellation circuit for the mismatch operation.	106
Figure 5.14: Allan Variance graph of the acceleration controller output of the gyroscope (1207).....	108

LIST OF TABLES

TABLES

Table 1.1: Performance requirements for different type of gyroscope [10].	6
Table 2.1: Modal analysis results of the single-mass fully decoupled gyroscope designed in this work.	37
Table 3.1: Drive mode resonance characteristics of the sample gyroscope (Gyro 1207) used during the design of the closed loop drive mode controller for $14 V_{PM}$. ..	47
Table 5.1: Drive mode resonance characteristics of the vacuum packaged gyroscopes studied in this thesis.	91
Table 5.2: Sense mode resonance characteristics of the vacuum packaged gyroscopes studied in this thesis.	92
Table 5.3: Summary of the static acceleration test results for the gyroscopes studied in this thesis.....	100
Table 5.4: Measured g-sensitivity of the gyroscope (1207) with and without the acceleration cancellation electronics for the different quadrature set voltages.....	101
Table 5.5: Scale factor measurement results of the studied single-mass gyroscopes with and without the acceleration cancellation electronics for the mismatch operation.....	105
Table 5.6: ARW and bias instability performances of the single-mass fully decoupled MEMS gyroscopes studied in this thesis.	107
Table 5.7: ARW and bias instability performances of the acceleration outputs of the single-mass fully decoupled MEMS gyroscopes studied in this thesis.....	108

CHAPTER 1

INTRODUCTION

The adaptation of the IC processing technology for creating controllable, mechanical and movable micro structures in the past few decades has made the major contribution to the evolution of today's high-technology systems. The rapid growth of the micromachining technologies has generated various kinds of developments in many diverse fields, ranging from consumer products to communication, from inertial navigation systems to medicine and bioengineering. The great demand of the technology market for the low-cost high-performance miniaturized systems and challenging requirements for these systems have speeded up the efforts on the development of the different kinds of microsystems. In today's technology, many of the MEMS sensors have presented better performances than their macro scale counterparts. Similarly, MEMS gyroscopes are expected to take the place of the ring laser and fiber optic gyroscopes in many applications because of their high reliability, promising performance, small size, and low cost in the near future [1].

Over the last decade, significant performance improvements took place in the operation of vibratory MEMS gyroscopes, either by suppressing the undesired quadrature error between the resonance modes of the gyroscope or by matching the resonance mode frequencies [2], [3]. However, most of the high performance gyroscopes suffer from the environmental effects on the gyroscope output. The output of a high performance gyroscope should be independent of the environmental factors such as temperature, acceleration and vibration for a reliable operation. Particularly, the static acceleration acting along the sense axis of MEMS gyroscope is one of the considerable error sources for the micromachined gyroscopes [4]. Considering the application areas of high performance MEMS inertial sensors, these sensors are usually exposed to various vibrations and acceleration during the

operation. The external acceleration acting on the sense-axis of the gyroscope causes fluctuations in the output bias and shifts the scale factor, which directly degrade the reliability of the gyroscope output [5]. Therefore, the acceleration effect on the gyroscope output, or shortly its g-sensitivity, should be reduced for high reliability. This thesis mainly focuses on the compensation of the static acceleration sensitivity of MEMS gyroscopes.

This work proposes three different acceleration compensation methods based on the readout of the gyroscope rather than the mechanical design. The main working principle of all of the proposed methods is to sense the static acceleration acting along the sense axis of the gyroscope by comparing the amplitudes of the residual quadrature signals on the differential sense mode electrodes. The proposed methods are implemented in a logical order, i.e. each acceleration compensation study is an improved version of the previous one. In the first phase of the work, the acceleration sensing circuit is implemented without using any closed loop controller. In this method, the acceleration and rate outputs are simultaneously measured, and the effect of the acceleration on the rate output is compensated according to their experimental relations. In the second method, a controller is added to the acceleration sensing circuit by applying feedback to the sense mode electrodes to stop the motion of the sense axis caused by the static acceleration. Finally, special acceleration cancellation electrodes are added to the gyroscope structure by changing its mechanical design. In this technique, the feedback voltage is applied to these electrodes to cancel the effect of the static acceleration. In the scope of this thesis, closed loop drive, force-feedback, quadrature cancellation, and acceleration cancellation loops are designed and implemented to achieve the compensation of the static acceleration sensitivity of the gyroscope.

The organization of this chapter is as follows; Section 1.1 presents the fundamental operation principle of MEMS vibratory gyroscopes. Section 1.2 summarizes the performance parameters to evaluate the grade of the gyroscope and application areas of these sensors. Section 1.3 provides a brief overview of the micromachined gyroscopes reported in the literature. Section 1.4 demonstrates the gyroscope structure studied in this thesis. Section 1.5 gives information about the acceleration sensitivity of MEMS gyroscope and summarizes the different techniques used to

reduce the g-sensitivity. Finally, Section 1.6 presents the research objectives and thesis organization.

1.1 Operation Principle of MEMS Vibratory Gyroscopes

The fundamental operation principle of micromachined vibratory gyroscope relies on the Coriolis force. Figure 1.1 depicts an inertial frame to make the Coriolis force perceptible to the mind. To understand the Coriolis force, consider an object driven into a time-dependent motion along the x-axis. If the inertial frame is rotated along the z-axis with respect to a stationary frame, the Coriolis force exerts on the moving object. This fictitious force is orthogonal to both the oscillation and rotation axes. The Coriolis force can be expressed as [6]

$$F_C = -2m\Omega \times \dot{X} \quad 1.1$$

where m denotes the mass of the moving object, \dot{X} and Ω represent the velocity of the object and the rotation rate, respectively.

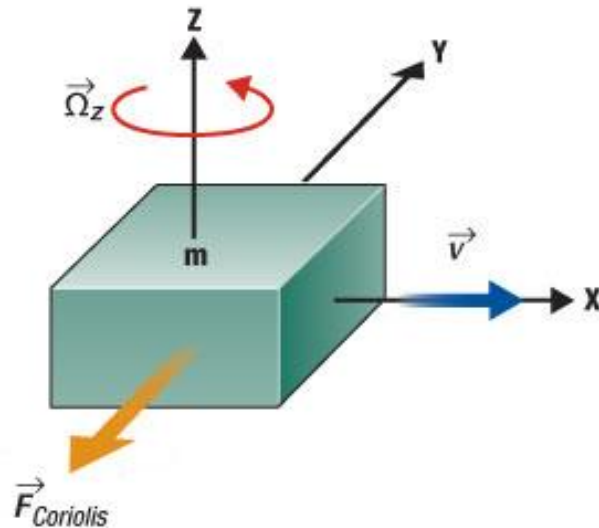


Figure 1.1: Inertial frame showing Coriolis force.

Figure 1.2 shows the conceptual view of the MEMS vibratory gyroscope. The MEMS vibratory gyroscope is basically comprised of three suspended frames which are drive frame, sense frame and proof mass. During the operation of the gyroscope, firstly, the movable proof mass is driven into the sustained oscillation along the drive axis of the gyro frame by means of electrostatic, piezoelectric, electromagnetic or electrothermal actuation mechanism [7]. If an angular rate is applied to the gyro frame in the sensitive axis of the gyroscope which is orthogonal to the drive and sense axes, a secondary oscillation, which amplitude is proportional to the applied angular rate, is induced along the sense axis. This oscillation can be detected by using capacitive, optical, piezoresistive, or piezoelectric sensing mechanisms [8].

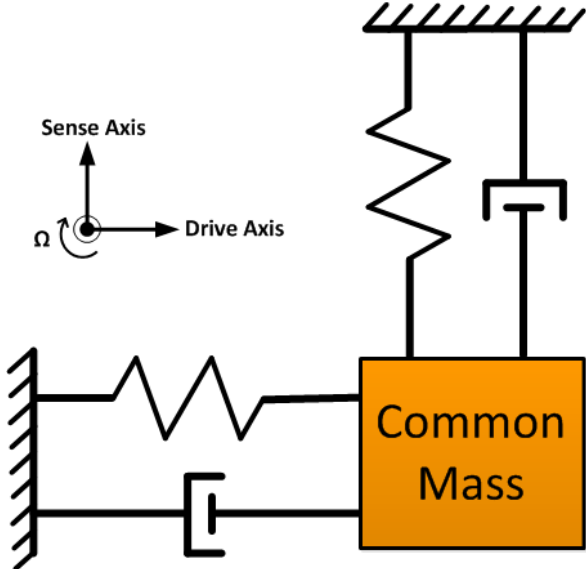


Figure 1.2: A conceptual view of the vibratory gyroscope.

1.2 Metrics of MEMS Gyroscopes and Their Application Areas

There are a number of parameters that determine the quality of a gyroscope. These parameters are bias instability, angle random walk, measurement range, scale factor and linearity, bandwidth, vibration sensitivity and g-sensitivity. Increasing the number of the performance specifications also makes the design more complex, and the importance of these parameters depends on the application. The whole definitions

and specifications to evaluate the performance of vibratory gyroscopes can be found in [9], some of which are briefly summarized below:

Angle Random Walk: It specifies the angular error increase with time because of the white noise in angular rate. The unit of angle random walk (ARW) is $^{\circ}/\sqrt{\text{hr}}$ or $^{\circ}/\sqrt{\text{Hz}}$.

Bias Instability: There exists a nonzero rate output in all gyroscopes even in the absence of angular rate input. This nonzero gyroscope output is called rate bias or zero-rate-output (ZRO). The stability of rate bias for a certain time is very important for a reliable gyroscope operation. Bias instability specifies the random variation in bias as computed over specified finite sample time and averaging time intervals, which is generally expressed in $^{\circ}/\text{hr}$.

Scale Factor: Scale factor represents the change of the gyroscope output to the applied angular rotation, typically expressed in $\text{mV}/^{\circ}/\text{s}$. Linearity (R^2) is another important parameter that shows how successful the fitted line expresses the variation of the measured data. It should be noted that nonlinearity is a different term which is used to express the systematic deviation from a specified output function.

Measurement Range: It is the maximum angular rate input that gyroscope can measure without saturation, which has unit of $\pm ^{\circ}/\text{sec}$.

Input Bandwidth: It is the maximum frequency of the angular rate input that gyroscope can detect without any loss. Input bandwidth depends on the settling time of the system, and it shows how fast gyroscope gives response to the input. It is typically expressed in the unit of Hz.

Vibration and Acceleration Sensitivity (G-Sensitivity): Vibration sensitivity is the ratio of the change in output because of the vibration about a sensor axis. Linear acceleration sensitivity or g-sensitivity is defined as the ratio of drift rate due to the acceleration about a gyro axis to the acceleration causing it.

While developing a complete rate sensor product, all of the design specifications discussed above should be considered, but the importance of these criteria depends on the application area of the gyroscope. In general, performance grades of the gyroscope are classified in three major categories according to the performance metrics; rate-grade, tactical-grade, and inertial-grade [10]. Table 1.1 shows the different requirements of these grades.

Table 1.1: Performance requirements for different type of gyroscope [10].

Parameter	Rate Grade	Tactical Grade	Inertial Grade
Angle Random Walk, $^{\circ}/\sqrt{\text{hr}}$	>0.5	0.5-0.05	<0.001
Bias Instability, $^{\circ}/\text{hr}$	10-1000	0.1-10	<0.01
Scale Factor Linearity, %	0.1-1	0.01-0.1	<0.001
Measurement Range, $^{\circ}/\text{sec}$	50-10000	>500	>400
Bandwidth, Hz	>70	~100	~100

Due to their small size, extremely low cost, and promising performances, micromachined gyroscopes have been becoming a feasible alternative to expensive and bulky conventional inertial sensors. In today's technology, MEMS gyroscopes have found applications in many different areas including military, automotive and consumer electronics market, aerospace industry [11]. In the automotive industry, MEMS gyroscopes are utilized in automotive safety systems such as the roll-over detection, ride stabilization, and advanced airbag and brake systems. Moreover, MEMS gyroscopes are used in the digital cameras for image stabilization, smart phones, and computer gaming industry. Miniaturization of gyroscopes provides the utilization of these sensors in the high-end applications such as micro-satellites and micro-robotics.

1.3 Overview of the Micromachined Vibratory Gyroscopes

The first micromachined gyroscope implementations were presented in the early 1980's with quartz gyroscopes, however their fabrication process was not adaptable to IC fabrication technology. In 1991, The Charles Stark Draper Laboratory reported the first IC compatible micromachined vibratory gyroscope, having a gimbal structure fabricated on a silicon wafer, with a resolution of $4^\circ/\text{sec}$ in 1 Hz measurement bandwidth [12]. In 1993, the Draper Laboratory developed an improved version of the silicon-on-glass tuning fork gyroscope fabricated through the dissolved wafer process, having an equivalent resolution of $0.19^\circ/\text{sec}$ in 1 Hz bandwidth [13].

In early 90's, many different fabrication methods and gyroscope structures were utilized to improve the performances of the micromachined gyroscopes. In 1994, University of Michigan demonstrated a vibrating ring gyroscope having a resolution of $0.5^\circ/\text{sec}$ in 25 Hz bandwidth. This gyroscope was fabricated by metal electroforming [14]. Then, they improved the performance of the vibrating ring gyroscope using the high-aspect ratio trench-refill technology [15]. In 1994, British Aerospace Systems also reported a single crystal ring gyroscope which was fabricated by deep dry etching of a $100\mu\text{m}$ silicon wafer on a glass wafer, with a resolution of $0.15^\circ/\text{sec}/\sqrt{\text{Hz}}$ in 30 Hz bandwidth [16]. In 2001, University of Michigan further developed the performance of the vibrating ring gyroscope through the high aspect-ratio combined poly and single-crystal silicon MEMS technology (HARPSS), achieving up to a resolution of $0.01^\circ/\text{sec}$ in a bandwidth of 1 Hz [17]. Although the vibrating ring gyroscopes have some certain advantages such as perfect matching between the drive and sense mode frequencies and minimum quadrature error between the corresponding modes compared to other gyroscope design, the limited actuation displacement is main drawback of this design. Therefore, the tuning fork type gyroscope structure had widely used to boost the performance of the MEMS gyroscopes by taking the advantage of large drive displacement. In 1997, Robert Bosch GmbH reported z-axis micromachined tuning fork gyroscope design which uses electromagnetic drive and capacitive sensing [18]. In 1997, Daimler Benz also developed a bulk-micromachined tuning-fork gyroscope with piezoelectric drive and piezoresistive detection [19]. In 2004, Honeywell presented commercial MEMS vibratory gyroscopes adapting the tuning fork architecture previously demonstrated

by Draper's Laboratory. These gyroscopes showed less than $30^\circ/\text{hr}$ of bias in-run stability performance and $0.05^\circ/\sqrt{\text{hr}}$ of angle random walk performance [20].

In mid-1990's, surface micromachined gyroscopes started to appear by the fabrication of the mechanical sensor element and readout on the same chip area. In 1995, Murata demonstrated the first surface micromachined gyroscope. Its resolution was about $2^\circ/\text{sec}/\sqrt{\text{Hz}}$ [21]. In 2001, Carnegie Mellon University demonstrated CMOS integrated z-axis gyroscopes with a noise floor of $0.5^\circ/\text{sec}/\sqrt{\text{Hz}}$ using a maskless post-CMOS micromachining process [22]. In 2002, Analog Device developed a dual resonator z-axis gyroscope fabricated by the iMEMS process. This gyroscope was the first commercial gyroscope with a bias instability of $50^\circ/\text{hr}$ and a resolution of $0.015^\circ/\text{sec}$ [23]. In 2003, Carnegie Mellon demonstrated a better version of the surfaced micromachined gyroscope which was fabricated on a thicker structural layer to decrease the Brownian noise by increasing the mass. The noise floor of this gyroscope was $0.02^\circ/\text{sec}/\sqrt{\text{Hz}}$ at 5 Hz [24]. Apart from these groups, Microsystem Laboratory at UC Irvine focused on the mechanical design of the gyroscopes and presented new design architecture of vibratory gyroscope in 2006. This gyroscope has 1-DOF drive mode and 2-DOF sense mode [25]. This gyroscope demonstrated a noise floor of $0.64^\circ/\text{sec}/\sqrt{\text{Hz}}$ at 50 Hz. In 2008, they further improved the design architecture, achieving a gyroscope with a resolution of $0.09^\circ/\text{sec}/\sqrt{\text{Hz}}$ and a bias instability of $0.08^\circ/\text{sec}$ [26]. Georgia Institute of Technology implemented mode-matched gyroscopes to achieve the bias instability less than $1^\circ/\text{hr}$ [27], [28]; however, the bandwidth of these gyroscopes was limited by the mechanical bandwidth of the gyroscope which was about a few Hz under mode-matched condition. In 2009, Thales Avionics demonstrated a mode-matched gyroscope with digital control system, achieving an ARW of $0.01^\circ/\sqrt{\text{hr}}$ and a bias instability of less than $0.1^\circ/\text{hr}$ [29]. In 2010, Draper Laboratories reported the gyroscope with bias instability of $0.03^\circ/\text{hr}$ and ARW of $0.002^\circ/\sqrt{\text{hr}}$, which has been one of the best performances in the recent times.

1.4 Gyroscopes Studied in This Thesis

Figure 1.3 depicts the simplified view of the single-mass fully decoupled MEMS gyroscope without additional acceleration cancellation electrodes studied in this thesis. Previously, this gyroscope was used to achieve the automatic mode-matching between the drive and sense mode resonance frequencies of the gyroscope by applying a feedback voltage to frequency tuning electrodes [30]. After the mode-matching study, it is also used for the implementation of the acceleration compensation methods in the first and second phases of this study [31].

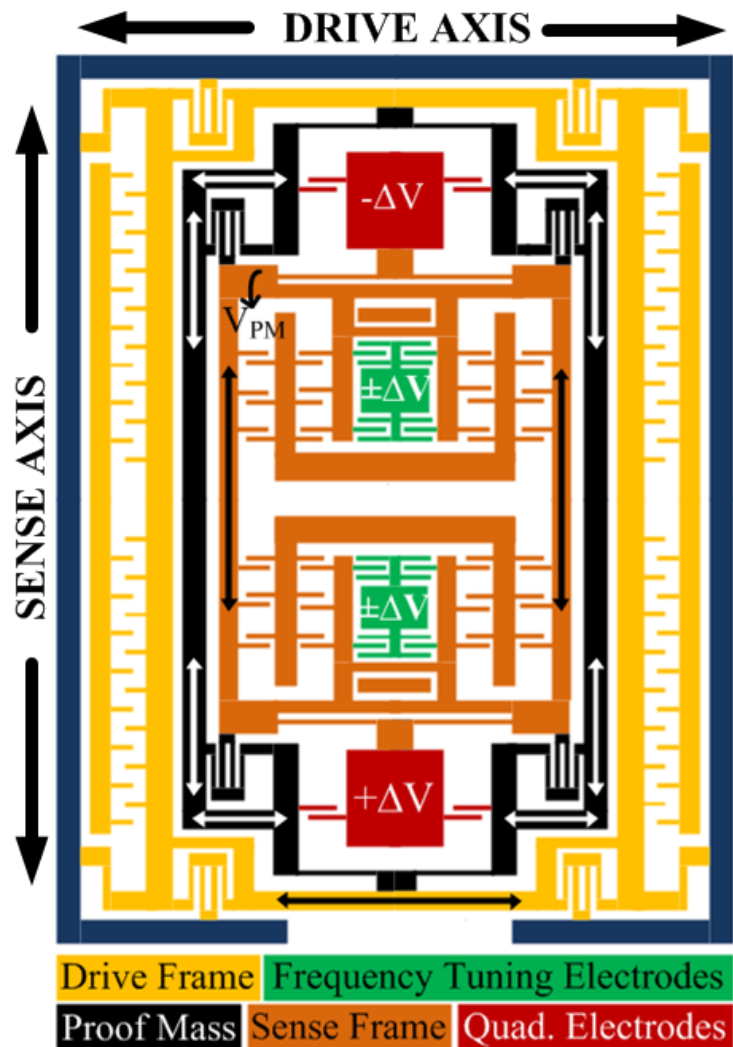


Figure 1.3: Simplified view of the single-mass fully decoupled MEMS gyroscope without the dedicated acceleration cancellation electrodes studied in the scope of this thesis [30].

The proposed acceleration sensing method uses the amplitude difference information of the quadrature signals on the differential sense mode electrodes; therefore, the sense mode of the gyroscope should have one resonance peak to exactly sense the amplitude of the quadrature signal. Thus, a single mass gyroscope or mechanically connected double mass gyroscope is required for the implementation of the proposed acceleration compensation techniques. The gyroscope shown in Figure 1.3 employs additional frequency tuning electrodes for the mode-matching operation; however, the mismatch operation is preferred in this study to ensure that there is no phase error exists due to the operation mode during the acceleration test. If the mode matching between the drive and sense mode resonance frequencies is not exactly achieved, additional phase error occurs during the modulation and demodulation steps in the control electronics, causing the leakage of the quadrature error to the rate output. Although the sensitivity of gyroscope is less in the mismatch mode, it provides more reliable operation in terms of stability and phase error.

In this study, the acceleration acting along the sense axis of the gyroscope is sensed by comparing the amplitudes of the differential quadrature signals which already exist in the system. In the first phase of this study, the acceleration and rate information are simultaneously collected during the acceleration tests. Then, the rate output is corrected by using the experimental relation between the rate and acceleration outputs [31]. In the second phase of this study, the effect of the acceleration on the rate output is suppressed during the operation by applying a DC feedback voltage to the sense mode electrodes using the non-inverting inputs of the sense mode preamplifiers.

Figure 1.4 shows the simplified view of the single-mass fully-decoupled MEMS gyroscope with the dedicated acceleration cancellation electrodes. In the third phase of this study, the compensation of the static acceleration sensitivity on the rate output of the gyroscope is achieved by applying a DC potential to the additional acceleration cancellation electrodes. Implementing additional electrodes for the acceleration cancellation provides the isolation of the acceleration cancellation circuit from the remaining part of the gyroscope; as a result, the acceleration cancellation controller does not affect the other control loops. The gyroscope is consisted of a single mass due to the reason discussed above. This gyroscope also includes the frequency tuning electrodes considering the mode-matching operation.

Two gyroscopes studied in this thesis are fabricated in METU using the modified SOG process [32]. While the first gyroscope is vacuum packaged at die level using the projection welder method, the second gyroscope is fabricated using wafer level vacuum packaging process [33].

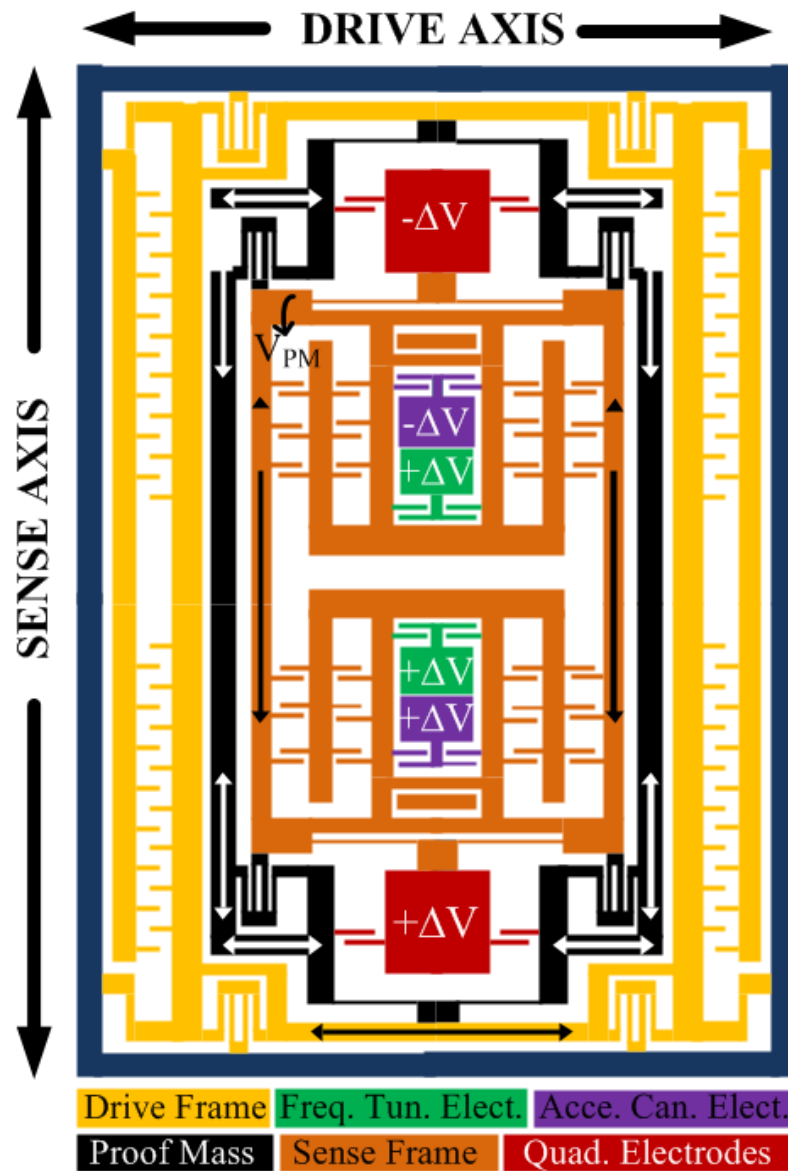


Figure 1.4: Simplified view of the single-mass fully decoupled MEMS gyroscope with the dedicated acceleration cancellation electrodes studied in the scope of this thesis.

The main purpose of this thesis is to compensate the effect of the quasi-static acceleration on the rate output of the gyroscope. Although a study was conducted on the static acceleration sensitivity of the MEMS gyroscope in METU [5], the acceleration compensation methods were proposed and implemented successfully for the first time. Before using these methods, the drive, sense and quadrature control loops were constructed and optimized. Then, the acceleration sensing and compensation cancellation circuits were successfully implemented using the gyroscope in Figure 1.3. Finally, the closed loop acceleration cancellation circuit was implemented on the gyroscope having additional acceleration cancellation electrodes, shown in Figure 1.4.

1.5 Overview of Acceleration Sensitivity of MEMS Gyroscope and Compensation Techniques

The operation of the MEMS vibratory gyroscopes relies on the Coriolis coupling, which enables the transfer of the energy from the drive to sense mode in the presence of an angular rotation. With the advance development in the gyroscope performance characteristics including the bias instability, resolution and bandwidth, the environmental effects such as vibration and acceleration acting on the gyroscope have a prominent impact on the reliability and robustness of the gyroscope [34], [35]. These effects causes an output error, namely ‘acceleration sensitivity’ or ‘acceleration output’.

In real applications, the outputs of all MEMS gyroscopes are affected from the acceleration because of the fabrication imperfections and asymmetry in their mechanical designs. The effect of acceleration on the gyroscope output can be seen in the different forms, the most significant ones are usually sensitivity to linear acceleration (or g sensitivity) and vibration rectification (or g^2 sensitivity). Since most of the gyroscopes are subjected to the Earth’s 1 g field of gravity in the application, the sensitivity acceleration exhibits one of the largest error sources [36].

The high frequency acceleration or vibration outputs are difficult to predict and very hard to compensate using electronics; thus, the compensation of the vibration rectification error is usually done by improving the mechanical design of gyroscope rather than the control electronics. A common method to reduce the effect of the

external acceleration or vibration is to use the tuning-fork type vibrating gyroscopes (TFG) which are believed to be insensitive to the common mode signals such as linear acceleration because these signals are mitigated by the differential reading of the sense mode signals coming from the two differentially-connected masses [24], [34], [37], [38]. However, it has been found that tuning fork type gyroscopes could still experience an output error caused by applying the linear acceleration along the sense axis to the gyros. University of Michigan made a study on the error sources causing the acceleration output in ideal fabricated TFGs and identified three major error sources which are the capacitive nonlinearity of the parallel plate sense electrodes, the unbalanced electrostatic force along the sense direction of the drive electrodes and the unbalanced electrostatic force along the drive direction of the drive electrodes [39]. The most significant error source has been reported as the acceleration along the sense direction. However, the analysis was based on the ideal fabricated TFG without considering the mismatch during fabrication. Due to the limitation of the technology, there are no perfectly ideal TFGs.

Implementing a micro-mechanical shock absorber under the sensor structure is another method to eliminate the effect of random high-frequency accelerations or vibrations [40]. Although this method provides a solution for the vibration sensitivity of a gyroscope, it does not eliminate the effects of static or low frequency accelerations. Acceleration sensitivity of the gyroscope can also be improved by calibrating the gyroscope output with the aid of an additional external accelerometer; however, the amount of the measured acceleration cannot always be the acceleration sensed by the gyroscope due to the difference in the physical locations of both sensors [36]. Quadruple mass gyroscope design is also implemented to make the sensor more immune to the external shock and vibration [41]. However, it is hard to realize a higher performance due to the complex structure of four-mass gyroscopes.

This thesis study focuses on the static or low frequency acceleration sensitivity of the MEMS gyroscopes. As opposed to the previously reported studies in the literature, it aims to improve quasi-static acceleration sensitivity of the gyroscope by modifying the control electronics instead of utilizing complex mechanical design. It should be noted that the high frequency acceleration or vibration sensitivity of the gyroscope is out of the concept of this thesis study.

1.6 Research Objectives and Thesis Organization

The fundamental object of this thesis study is to theoretically analyze the static acceleration sensitivity of the fully decoupled MEMS gyroscope and to successfully construct the acceleration sensing and compensation circuits to improve the quasi-static acceleration sensitivity of the gyroscope. The definite goals of this research can be listed in the following way:

1. Analysis of the effect of the static acceleration on the single mass gyroscope operation. The effect of the static acceleration on the sense-mode electrodes, force-feedback electrodes, quadrature cancellation electrodes and sense mode springs should be examined analytically to determine the main reason of the static acceleration sensitivity of the gyroscope. Moreover, the experimental data should be provided to show the effect on the acceleration on the rate output.
2. Design of single-mass fully-decoupled gyroscope including of acceleration cancellation electrodes. The acceleration cancellation electrodes are supposed to generate an electrostatic force to balance the acceleration force acting along the sense axis of the gyroscope. Using dedicated electrodes, the operation of the acceleration cancellation control loop should be isolated from the other control loops in the gyroscope system. Moreover, the number of the acceleration cancellation electrodes should be determined for the range of the g-cancellation circuit.
3. Fabrication of a designed single-mass gyroscope by using the modified SOG process and the corresponding wafer level hermetic encapsulation process. The problems related with process should be identified and solved. The process steps should be optimized to achieve a consistency between parameters of the fabricated and design sensor. The fabricated gyroscope wafer should be vacuum packaged, and the fabrication steps for the vacuum packaging process should also be optimized.
4. Design and implementation of the controller electronics. The controller electronics includes the drive, sense, quadrature and acceleration control loops. The controller values should be optimized by the simulation to achieve enough phase margin, fast settling time and small overshoot for all control loops. Each loop should be separately designed but their interactions to each other should also

be considered during the operation. As a final step, the control electronics should be integrated with the gyroscope on a PCB for the overall system evaluation.

The organization of the thesis and the contents of the following chapters are as follows.

Chapter 2 introduces mathematical modeling of vibratory MEMS gyroscopes. After presenting the related equations, the design of acceleration cancellation electrodes for the corresponding gyroscope structure is provided. Moreover, the effect of the static acceleration on the sense mode electrodes, force-feedback electrodes, quadrature cancellation electrodes and sense mode springs are investigated analytically. Finally FEM simulations for modal analysis are demonstrated.

Chapter 3 presents the control electronics design for drive control, force feedback, quadrature cancellation and acceleration cancellation loops. The details of the design steps are provide and the designed systems are evaluated in SIMULINK.

Chapter 4 gives the details of modified SOG process used for the fabrication of the sensor wafer. Moreover, wafer level vacuum packaging process is explained in details. Finally, the fabrication results are represented.

Chapter 5 gives the test results of the single mass gyroscopes for three different acceleration compensation methods. Firstly, static and centrifugal acceleration test results are represented with and without the acceleration compensation circuits. Then, the experimental data is provided to show the relation between the level of the quadrature error and g-sensitivity. Finally, the performance test results of the studied gyroscopes are given.

Finally, Chapter 6 summarizes this thesis study and highlights the achievements of this work. Future research topics are also suggested.

CHAPTER 2

VIBRATORY GYROSCOPE THEORY AND MODELLING

This chapter presents the vibratory gyroscope theory and describes the mechanical model of the gyroscopes studied in this thesis. Section 2.1 presents mechanical model of the gyroscope providing brief information about the drive and sense mode dynamics. Section 2.2 gives the extraction of the model parameters. Section 2.3 and 2.4 shows the capacitive actuation and sensing mechanism. Section 2.5 explains the electrostatic tuning effect used to tune the resonance frequencies. Section 2.6 provides information about the effect of the static acceleration on the gyroscope operation and presents the design of the g-cancellation electrodes for the fully decoupled gyroscope. Section 2.7 presents the FEM simulations used for the model analysis. Finally, Section 2.8 summarizes this chapter.

2.1 Mechanical Model of the Gyroscope

There is a trade-off between the angular rate sensitivity and mechanical crosstalk in the micromachined gyroscopes. As the coupling among the drive, sense and proof masses increases, both the sensitivity of gyroscope to angular rate input and the undesired mechanical crosstalk increase. However, the mechanical crosstalk should be minimized to achieve minimum zero-rate offset in a good gyroscope. Therefore, micromachined gyroscopes structures employ different decoupling mechanisms to decrease the mechanical crosstalk. Figure 2.1 shows three basic decoupling mechanisms. Figure 2.1-a describes the simplest configuration which the gyroscope is coupled. In this mechanism, the drive, sense and proof mass are connected to each other and they have 2DOF (Degree-of-Freedom) motion capability. Thus, any misalignment associated with the drive axis and drive actuation force causes a rate

error signal at the output. Figure 2.1-b shows an improved decoupling mechanism, in which the motion of the drive mass is restricted to 1DOF along the predetermined drive axis whereas the sense mass has 2DOF motion capability. Figure 2.1-c shows the fully-decoupled gyroscope structure, in which the drive and sense masses have 1DOF movement capability along their drive and sense axes, respectively. By keeping the drive and sense axes orthogonal to each other, the mechanical crosstalk is minimized in the expense of losing rate sensitivity this mechanism.

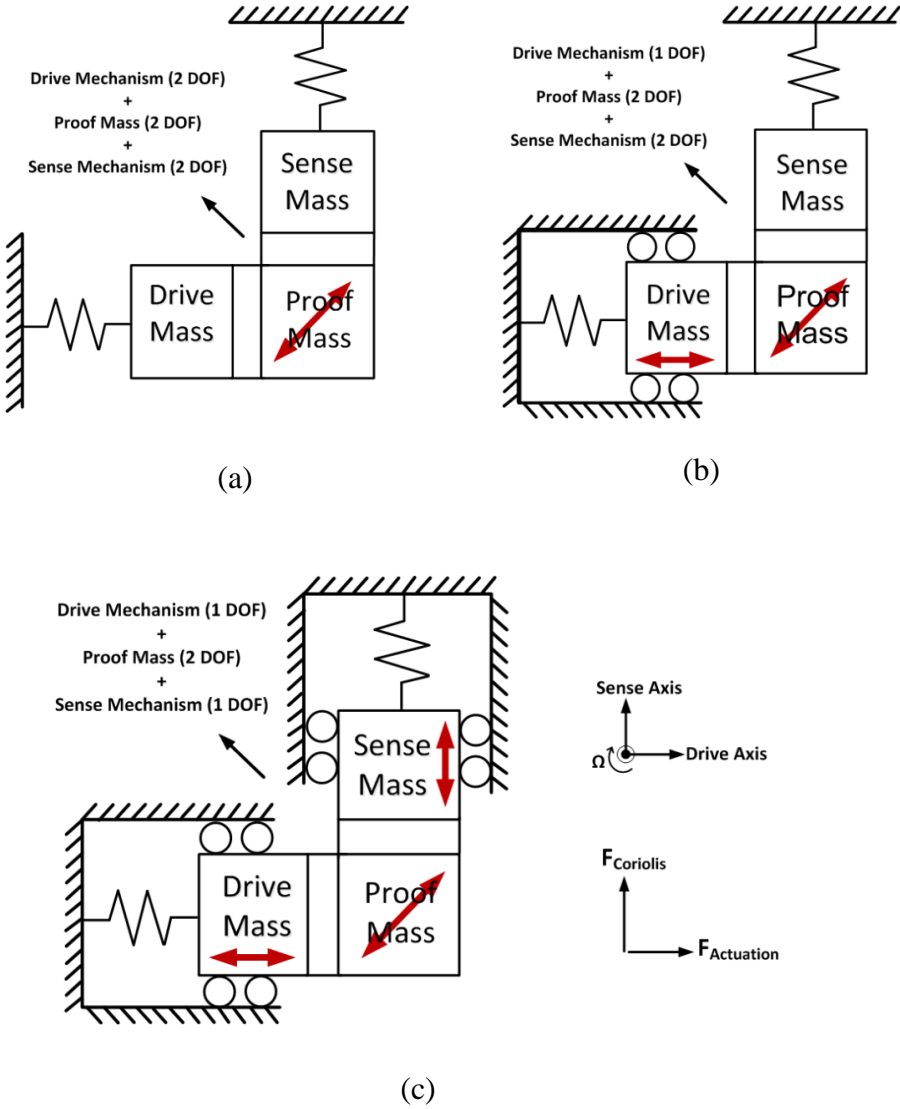


Figure 2.1: Three basic decoupling mechanisms: (a) simplest decoupling configuration with no special decoupling treatment, (b) improved decoupling configuration and (c) fully-decoupled configuration.

Figure 1.4 depicts the simplified view of the fully-decoupled gyroscopes studied in this thesis. The gyroscope structure is composed of drive frame, proof mass and sense frame. The drive and sense frames have 1DOF movement capability, whereas the proof mass frame have 2DOF movement capability to transfer Coriolis acceleration induced by rotation to the sense mode, as in Figure 2.1-c. In mechanical structure, the drive and sense axes are designed to be completely orthogonal. However, an undesired mechanical cross-talk, called quadrature error is inevitable between the drive and sense modes due to the fabrication imperfections.

2.1.1 Drive Mode Dynamics

The proof mass should be driven into a sustained oscillation along the drive axis for the generation of the Coriolis acceleration along sense axis of the gyroscope when an angular input is applied. The Coriolis force is directly proportional with the drive displacement. Therefore, the drive mode of the gyroscope should be well-modeled, and the drive mode oscillation should be kept constant over time for a stable operation. The mathematical model of drive mode resonator can be represented by the second order differential equation based on the mass-spring-damper system as follows:

$$f_D(t) = m_D \ddot{x}(t) + b_D \dot{x}(t) + k_D x(t) \quad 2.1$$

where f_D is the actuation force acting on drive resonator, m_D is the drive frame mass including the drive and proof masses, $x(t)$ is the displacement of the drive mode, b_D and k_D denote the damping factor and spring constant of the drive mode, respectively. The frequency domain representation of the time domain equation in Equation 2.1 is obtained by taking Laplace Transform, and the resultant relation can be expressed as

$$F_D(s) = m_D s^2 X_D(s) + b_D s X_D(s) + k_D X_D(s) \quad 2.2$$

By rearranging the terms in Equation 2.2, the direct relation between the force and displacement can be written in terms of the mechanical system parameters as follows:

$$\frac{X_D(s)}{F_D(s)} = \frac{1}{m_D(s^2 + \frac{w_D}{Q_D}s + w_D^2)} \quad 2.3$$

In equation 2.3, w_D is the resonance frequency of the drive mode, and Q_D is the quality factor of the drive mode. These parameters can be calculated by using the following relations:

$$w_D = \sqrt{\frac{k_D}{m_D}} \quad 2.4$$

$$Q_D = \frac{\sqrt{k_D m_D}}{b_D} \quad 2.5$$

If the operating frequency of the actuation force is equal to the mechanical resonance frequency of the system, i.e. under the resonance condition, Equation 2.3 is simplified to

$$\frac{X_D(jw)}{F_D(jw)} = \frac{1}{m_D \frac{w_D^2}{Q_D}} = \frac{1}{j} \frac{Q_D}{k_D} \quad 2.6$$

Equation 2.6 states that there is a phase shift of 90^0 between the drive mode displacement and the applied actuation force under the resonance condition. It also implies that the amplitude of the drive mode displacement is directly proportional with the quality factor. Under the resonance condition, the energy dissipation in the system is minimized; therefore, the maximum displacement with the minimum applied force is achieved under this condition.

2.1.2 Coriolis Coupling and Sense Mode Dynamics

The mechanical structure of the sense mode is similar to which of the drive mode, therefore; the sense mode dynamics can also be modeled with the second order differential equation based on the mass-spring-damper system by replacing the subscript “ D ” with “ s ” which indicates the sense mode parameters. As being different from the drive mode, an external actuation force is not required in the sense mode. Instead, the operation of the sense mode relies on the self-induced Coriolis force

which is directly proportional to the mass and the velocity of the drive mode as stated in Equation 1.1. While constructing the sense mode dynamics based on the Coriolis coupling, one should be careful about that the proof mass is the only element subject to the Coriolis force in a fully decoupled gyroscope. Therefore, the sense mode dynamics can be expressed as

$$-2m_{PM}\Omega_Z(t)\dot{x}(t) - m_{PM}\dot{\Omega}_Z(t)x(t) = m_S\ddot{y}(t) + b_S\dot{y}(t) + k_S y(t) \quad 2.7$$

In Equation 2.7, m_{PM} and m_S denote the proof mass and the total sense mass including the proof mass and the mass of the sense electrodes, respectively. Let assume a time-varying angular rate input and a time-varying displacement of drive mode in the following form:

$$x(t) = X_D \cos(w_D t) \quad 2.8$$

$$\Omega_Z(t) = \Omega_Z \cos(w_Z t) \quad 2.9$$

where w_Z is the frequency of applied angular rotation. After inserting the Equation 2.8 and 2.9 into Equation 2.7 and following the necessary mathematical calculations, the sense mode response can be obtained as separated its frequency components in the following form:

$$Y(w_D + w_Z) = \frac{\frac{m_{PM}}{m_S} X_D \Omega_Z \left(w_D + \frac{w_Z}{2} \right)}{(w_S^2 - (w_D + w_Z)^2) + j \frac{w_S}{Q_S} (w_D + w_Z)} \quad 2.10-a$$

$$Y(w_D - w_Z) = \frac{\frac{m_{PM}}{m_S} X_D \Omega_Z \left(w_D - \frac{w_Z}{2} \right)}{(w_S^2 - (w_D - w_Z)^2) + j \frac{w_S}{Q_S} (w_D - w_Z)} \quad 2.10-b$$

According to Equation 2.10, the sense mode output of the gyroscope has two frequency components as a response to a sinusoidal angular rate input. The sense mode response can be analyzed for two special cases, regarding the separation between the mechanical resonance frequencies of the drive mode and sense mode. If the frequency of the angular rate input is zero and there is a frequency mismatch

between the drive and sense mode resonance frequencies, Equation 2.10 can be simplified to

$$Y(w_D + w_z) + Y(w_D - w_z) \cong \frac{2X_D \Omega_z Q_S}{2w_D \Delta w - jw_D \frac{w_S}{Q_S}} \frac{m_{PM}}{m_S} \quad 2.11$$

where Δw denotes the frequency difference between the corresponding resonance mode frequencies. If the angular rate input is DC and the resonance frequencies of the drive mode and sense mode is very close to each other, i.e. $w_S \cong w_D$, then Equation 2.11 can be represented as

$$Y(w_D + w_z) + Y(w_D - w_z) \cong \frac{2X_D \Omega_z Q_S}{jw_D} \frac{m_{PM}}{m_S} \quad 2.12$$

Equation 2.11 implies that the displacement of the sense mode is boosted by the mechanical quality factor under the mode-matched condition. In other words, the sensitivity of the gyroscope is maximized when the resonance frequencies of the drive and sense modes are equal to each other. Under the mode-matched condition, there is 90° phase difference between the drive mode displacement and sense mode displacement. The mode-matched operation has some certain advantages but it gets difficult to achieve the exact mode-matching condition as the quality factor of the sense mode increases.

If the resonance frequencies of the drive and sense modes are highly separated from each other, i.e., $w_D \leq w_S$, and the frequency of the angular rate input is zero, Equation 2.11 can be simplified to

$$Y(w_D + w_z) + Y(w_D - w_z) \cong \frac{X_D \Omega_z}{\Delta w_D} \frac{m_{PM}}{m_S} \quad 2.13$$

When compared to the mode-matched operation, there is a significant decrease in the corresponding sensitivity under the mismatched operation. There is no phase difference between the drive and sense mode displacements under the mismatched condition.

It is possible to decide whether the operation condition of gyroscope is mode-matched or mismatch by looking at the denominator of Equation 2.11. As a rule of thumb, if the frequency mismatch between the corresponding resonance frequencies is smaller than 1/10 of the response bandwidth which is $\frac{f_s}{Q_s}$, the operation mode of the gyroscope can be considered as mode-matched. Similarly, if the frequency mismatch between the corresponding resonance frequencies is larger than 1/10 of the response bandwidth, the operation mode of the gyroscope can be considered as mismatched. The detailed information about the sense mode dynamics of the MEMS vibratory gyroscope can be found in [6].

2.2 Design of MEMS Vibratory Gyroscope and Model Parameters

Mechanical model parameters are should be identified to establish the governing equations of the MEMS gyroscope analyzed in Section 2.1. Fundamentally, these parameters are the spring constant, mass and damping factors, which are presented in the subsections below.

2.2.1 Mechanical Spring Constant Estimation

The degrees-of-freedom of the movable particles in the vibratory gyroscopes is identified by the mechanical springs. Moreover, mechanical spring constants are ones of the important design parameters, determining the drive and sense mode resonance frequencies. Three types of spring structures are utilized in the mechanical structure of the gyroscope. These springs connect the drive, proof mass and sense frames. The double-folded and half-folded spring structures are employed in the drive mode since the linearity is the main concern in this mode due to the large displacement in the order of μm . On the other side, the sense mode displacement can only reach to a few angstroms so the linearity is not a problem for this mode. Instead, the area of the springs is considered in the sense mode spring design; thus, the clamped-guided-end springs are employed in the sense mode. The detailed analysis on spring design and spring constant estimation can be found in [6].

2.2.2 Mass and Damping Factor Estimation

The mass of the movable parts can be calculated by using the following formula:

$$m = dV \quad 2.14$$

where d denotes the density of the material and V represents the volume that can be directly calculated from the structure. However, a fraction of the spring masses should be also added to this expression according to Rayleigh energy method to estimate the effective masses for the resonance frequency calculation [6].

The calculation of the damping factor is not easy since it depends on many parameters and requires a complicated analysis. Instead, the damping factor is estimated by the resonance tests.

2.3 Electrostatic Actuation Using Parallel Plate Capacitor

A parallel plate capacitor which is comprised of two isolated conductors is a simple and widely used configuration to generate electrostatic force for the actuation in the micromachined structures. If there is potential difference between the parallel plates, the energy is stored in the capacitor because of the charge accumulation. The stored energy causes a pulling electrostatic force between the stationary and movable conductors. The detailed analysis for the electrostatic actuation using the parallel plate configuration can be found in [6].

There are two fundamental parallel plate structures utilized for the actuation mechanism in the MEMS gyroscope studied in this thesis, namely varying-overlap area type capacitor and varying-gap type capacitor. In the varying-overlap type capacitor, the displacement occurs along the lateral direction by causing a change in the overlap area of the parallel plates. For this configuration, the acting force on the parallel plates can be expressed as

$$F = \frac{1}{2} \alpha N \epsilon_0 \frac{H_0}{D_0} V^2 \quad 2.15$$

where α is the correction factor for the fringing fields, N represents the number of the capacitor pairs, ϵ_0 is the permittivity of the free air, V is the voltage difference between

the parallel plates, H_0 and D_0 are the overlap height and gap spacing of the plates, respectively. Equation 2.15 implies that the electrostatic force does not depend on the position so the large displacement can be achieved without degrading the linearity using the varying-overlap are type capacitors. This is why they are generally utilized in drive mode actuation mechanism which requires large displacement to reduce the mechanical noise in the system.

In the varying-gap type capacitors, the motion occurs along the y direction by increasing the gap and decreasing the anti-gap between the parallel plates, or vice versa. For this configuration, the acting force on the parallel plates can written as

$$F = \frac{1}{2} \alpha N \epsilon_0 \frac{H_0 L_0}{(D_0 - y)^2} V^2 \quad 2.16$$

where L_0 is the overlap length of the plates and y is the displacement due to the electrostatic actuation. As seen in Equation 2.16, the generated electrostatic force shows a nonlinear behavior in y direction. The sensitivity for the varying-gap type capacitor is higher compared to the varying-overlap area type capacitor; however, the linearity gets worse. For small displacements, the force can be assumed to be constant by neglecting the displacement term in the denominator of Equation 2.16. In the sense mode of the gyroscopes, the displacement due to the angular rate input is not much more than a few angstroms which are much smaller than the capacitive gaps. Rather than the large actuation displacement, the sensitivity is the important parameter in the sense mode because it determines the resolution of the system. Thus, the varying-gap type capacitors are used in the sense mode of the gyroscopes.

2.4 Capacitive Sensing

The capacitive sensing mechanism is used to convert the movement of the mechanical structure to the electrical signal. In the gyroscope structure, there will be two motions which should be sensed by the capacitive sensing mechanism: the drive-mode oscillation which constitutes the basis of the self-resonance actuation of the drive-mode and sense-mode displacements which gives information about the angular rate inputs. In the capacitive sensing mechanism, firstly, the mechanical displacement is converted to the current by the capacitors; then, the current is fed to

the interface circuit to obtain the voltage equivalent of the displacement. The general expression of the current flowing through a capacitor is

$$I_{out} = \frac{dQ}{dt} = \frac{d(C(t)V(t))}{dt} = C \frac{dV(t)}{dt} + V \frac{dC(t)}{dt} \quad 2.17$$

For the actual gyroscope operation, $V(t)$ consists of the fixed proof mass voltage, V_{PM} , which is the potential difference between the detection electrodes and movable part and the time varying voltage which is caused by the displacement of the sensing capacitors. Since the time varying voltage is much smaller than the constant proof mass voltage in the real operation, the expression for the output current can be written in the following ways assuming sinusoidal drive and sense displacement

$$I_{out}(t) \cong V_{PM} \frac{dC}{dt} = V_{PM} \frac{\partial C}{\partial X} \frac{\partial X}{\partial t} \quad (\text{time domain}) \quad 2.18\text{-a}$$

$$I_{out}(j\omega) \cong V_{PM} \frac{\partial C}{\partial X} j\omega X(j\omega) \quad (\text{frequency domain}) \quad 2.18\text{-b}$$

2.5 Electrostatic Spring Effect

The drive and sense mode resonance frequencies are important in the operation of the gyroscope and determined by the springs. However, the width of the springs cannot be defined with a tolerance better than 10 % in a standard micromachining technology. Therefore, the electrostatic spring effect of the varying-gap type sense fingers is used to adjust the resonance frequency of the sense mode with respect to drive mode resonance frequency. By differentiating the expression given in Equation 2.16 with respect to displacement y , the following expression is obtained in the unit of N/m :

$$\delta k_{electrostatic} = \frac{\partial^2 E}{\partial y^2} = \frac{\partial F}{\partial y} = \alpha \epsilon_0 \frac{H_0 L_0}{(D_0 - y)^3} V^2 \quad 2.19$$

Equation 2.19 states that the spring constant in the sense direction is softened due to the applied voltage on the varying gap capacitors. Thus, the sense mode resonance frequency can be adjusted by varying the DC voltage applied to the proof mass. It

should be noted that the electrostatic softening effect is not valid for the varying-overlap area type capacitors because the derivative of the force expression in Equation 2.15 with respect to the displacement term is zero. In practice, the mechanical sense mode resonance frequency is intentionally designed to be larger than the resonance frequency of the drive mode, then, it is adjusted by the electrostatic tuning effect. The frequency of sense mode with the softening effect then can be calculated as

$$w_S = \sqrt{\frac{k_S - \delta k_{electrostatic}}{m_S}} \quad 2.20$$

In equation 2.20, the condition where $k_S = \delta k_{electrostatic}$ is critical for the gyroscope operation because if the proof voltage exceeds the critical point, the movable part of the capacitor collapses onto the stationary part. This critical voltage is called pull-in voltage, it can be expressed in [42] as

$$V_{pullin} = \sqrt{\frac{k_S D_{gap}^3 D_{antigap}^3}{\alpha \epsilon_0 H_0 L_0 (D_{antigap}^3 + D_{gap}^3)}} \quad 2.21$$

2.6 Quasi-static Acceleration Sensitivity

Static acceleration sensitivity is one of the important of the problems in MEMS gyroscopes due to their application areas and the working principle of the sensors. Most of high performance gyroscopes suffer from the effects of the static acceleration at the gyroscope output. The quasi-static acceleration acting on the sense axis of the gyroscope causes a shift in the vibration axis of the sense mode, changing the average gap spacing of the varying-gap fingers and the sense mode dynamics. As a result, a fluctuation in the output bias and a shift in the scale factor occur, which straightly reduces the reliability of the sensor output.

During the gyroscope operation, the static acceleration acting along the sense axis of the gyroscope affects the gyroscope operation in three ways. Firstly, the shift of the sense mode vibration axis does not equally affect the amplitude of the differential sense-mode channel outputs because of the nonlinearity in the capacitive detection.

Consequently, the positive and negative sense-mode channel outputs fluctuate, causing a variation at the rate output in a differential reading scheme. Secondly, the capacitive gap spacing of the force-feedback electrodes changes with the applied static acceleration. As a result, the scale factor of the gyroscope varies as well as the output bias. Furthermore, the static acceleration slightly alters the level of the residual quadrature signal by disturbing the position of the quadrature cancellation electrodes and sense mode springs. A portion of the quadrature error appears as the rate offset because of the phase error coming from the electronics. Hence, any change in the quadrature signal is reflected to the rate output.

2.6.1 Effect of Static Acceleration on the Sense-Mode Electrodes

In the gyroscope operation, the sense mode displacement which carries information about the angular rate input or quadrature signal is picked up by the differential sense-mode electrodes. In the capacitive sensing mechanism, firstly, the sense mode output current is obtained by these electrodes, then; the obtained current is converted to the voltage by the transimpedance amplifier in the front-end electronics. However, the static acceleration acting along the sense axis of the gyroscope causes a change in the amplitude of the differential sense-mode channel outputs due to the nonlinearity in the capacitive detection.

Figure 2.2 depicts the simplified view of the sense-mode electrodes which detect the sense-mode displacement. In the absence of the static acceleration, the sense-mode frame is kept stationary with the aid of the force-feedback electronics, as shown Figure 2.2-a. In this condition, the sense-mode channel output voltage can be approximately expressed as

$$V_{SP} \cong \frac{\varepsilon N_{SP} H_0 L_0 \dot{y} V_{PM} Z_{pre} A_{inst}}{d_{gap}^2} \quad 2.22$$

where N_{SP} is the total number of the sense-mode electrodes, \dot{y} is the derivative of the sense-mode displacement, i.e. the velocity of the sense-mode, V_{PM} is the DC voltage applied to the proof mass, Z_{pre} is the gain of the transimpedance amplifier (TIA), and A_{inst} is the gain of the instrumentational amplifier which is used for the differential reading.

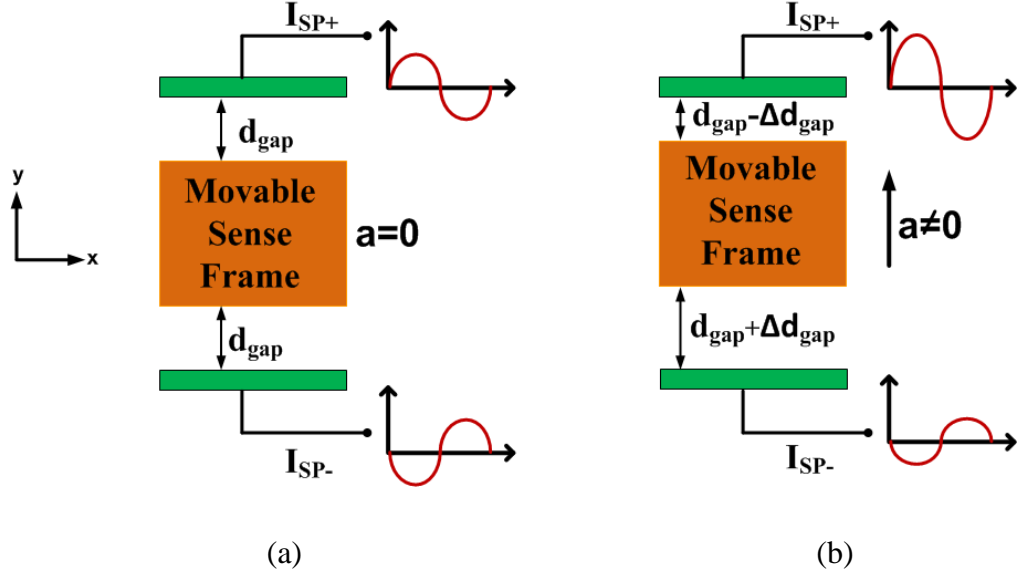


Figure 2.2: Conceptual view of the differential sense-mode electrodes under the conditions of (a) zero and (b) static acceleration. The sense mode output current increases in one side and decreases in the other under the static acceleration.

When a nonzero acceleration force acts on the movable sense frame as shown in Figure 2.2-b, the average gap spacing between the differential sense-mode electrodes decreases in one side and increases in the other. If the sense axis shifts Δd_{gap} due to the static acceleration a , the following relation can be derived for the sense-mode-channel output voltage:

$$V'_{SP} \cong \frac{\varepsilon N_{SP} H_0 L_0 \dot{\gamma} V_{PM} Z_{pre} A_{inst}}{d_{gap}^2} + \frac{N_{SP} \varepsilon H_0 L_0 \dot{\gamma} V_{PM} Z_{pre} A_{inst} \Delta d_{gap}^2}{d_{gap}^4} \quad 2.23$$

In equation 2.23, the change of the gap spacing Δd_{gap} can be written in terms of the sense mode resonance frequency w_s and the static acceleration a as follows:

$$\Delta d_{gap} \approx \frac{a}{w_s^2} \quad 2.24$$

By combining Equation 2.23 and 2.24, the change in the sense mode channel output signal, ΔV_{SP} , because of the static acceleration can be expressed as

$$\Delta V_{SP} \approx \frac{N_{SP} \cdot \varepsilon \cdot H \cdot L \cdot \dot{y} \cdot V_{PM} \cdot Z_{pre} \cdot A_{inst} \cdot a^2}{d_{gap}^4 \cdot \omega_s^4} \quad 2.25$$

However, the term ΔV_{SP} is very small compared to the term V_{SP} so the effect of the static acceleration on the sense mode electrodes is negligible. Moreover, if there is no angular rate input acting on the system, the sense-mode channel output voltage consists of only the quadrature signal. In this case, even if the AC sense signal output changes significantly due to the static acceleration, it does not affect the rate output because the closed-loop quadrature cancellation system holds the amount of the residual quadrature signal at a certain level, preventing the output bias from shifting.

2.6.2 Effect of Static Acceleration on the Force-feedback Electrodes

The function of the force-feedback electrodes is to stop the sense mode motion of the gyroscope caused by the angular rate input. The shift of the sense mode axis due to acceleration changes the force generated by the force-feedback electrodes, affecting directly the scale factor of the rate output. Figure 2.3 shows the conceptual view of the force-feedback electrodes. Under the stationary condition as shown in Figure 2.3-a, the force generated by the force-feedback electrodes can be expressed as

$$F_{FF} = V_{PM} \frac{\partial C_{FF}}{\partial y} V_{FF} \cong \frac{2\varepsilon H_0 L_0 V_{PM} V_{FF}}{d_{gap}^2} \quad 2.26$$

where $\partial C_{FF}/\partial y$ represents the sensitivity of the force-feedback electrodes, V_{PM} and V_{FF} denote the proof mass DC voltage and the amplitude of the AC signal applied to the force-feedback electrodes, respectively.

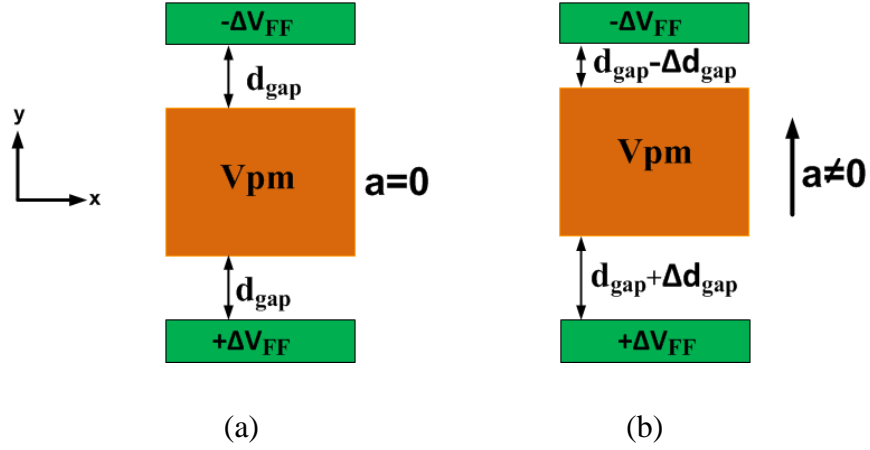


Figure 2.3: Conceptual view of the force-feedback electrodes under the conditions of (a) zero and (b) static acceleration.

If a nonzero static acceleration acts along the y -axis as depicted in Figure 2.3-b, the movable sense frame shifts in the direction of the acceleration, changing the gap spacing of the force-feedback electrodes. Under this condition, the electrostatic force generated by the force-feedback electrodes can be written as

$$F_{FF} \cong \frac{2\varepsilon H_0 L_0 V_{PM} V_{FF}}{d_{gap}^2} + \frac{2\varepsilon H_0 L_0 V_{PM} V_{FF} \Delta d_{gap}^2}{d_{gap}^4} \quad 2.27$$

By combining Equation 2.24 and 2.27, the change in force generated by force-feedback electrodes due to the static acceleration is found in terms of the sense mode resonance frequency ω_s and the static acceleration a as

$$\Delta F_{FF} \approx \frac{2\varepsilon H_0 L_0 V_{PM} V_{FF} a^2}{d_{gap}^4 \omega_s^4} \quad 2.28$$

Equation 2.28 implies that the force generation capability of the force-feedback electrodes increases with the applied static acceleration independently from the direction of the acceleration. This means that the same amount of the Coriolis acceleration is stopped by applying the smaller voltage to the force-feedback electrodes under the static acceleration, which directly causes the scale factor of the rate output to change.

2.6.3 Effect of Static Acceleration on the Quadrature Cancellation Electrodes and Sense Mode Springs

The quadrature error can be defined as the coupling of drive motion into the sense mode due to the mechanical spring imbalances. A ratio of the quadrature signal appears as the bias voltage at the output because of the phase error coming from the electronics. If it was only an offset, it would not create any problem because it could easily cancel by the electronics. However, the amount of the quadrature signal does not stay constant throughout the time. Moreover, the phase error in the system changes with the temperature, causing the offset at the rate output to vary. Therefore, the level of the quadrature error should be controlled to prevent the variation in the offset voltage. The function of the quadrature cancellation electrodes is to suppress the quadrature error with the help of the control electronics.

The static acceleration acting along the y -axis of the gyroscope affects the operation of the quadrature cancellation electrodes by changing the force generated by these electrodes. Figure 2.4 shows the simplified view of the quadrature cancellation electrodes. Under the stationary condition as depicted in Figure 2.4-a, the force generated by one quadrature cancellation electrode pair can be written as

$$F_q \approx -\frac{4\epsilon H_0 X V_{PM} \Delta V}{d_{gap}^2} \quad 2.29$$

where X represents the amplitude of the drive mode displacement, V_{PM} and ΔV denote the DC voltage applied to the proof mass and the DC voltage applied to the quadrature cancellation electrodes, respectively.

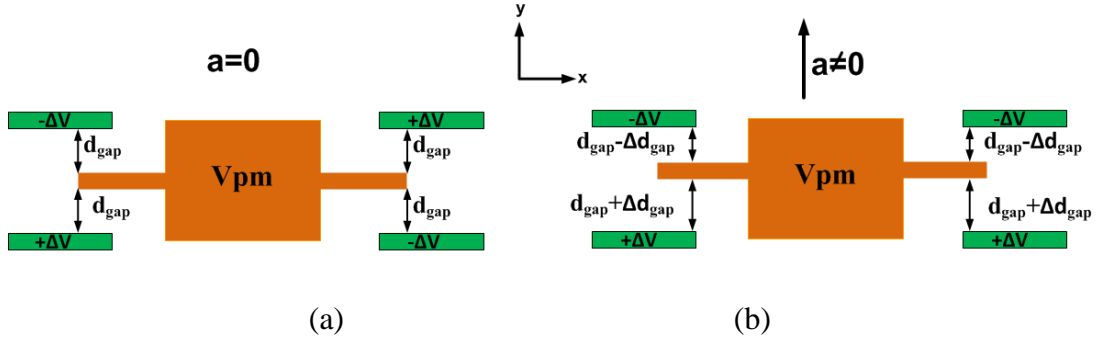


Figure 2.4: Conceptual view of the quadrature cancellation electrodes under the conditions of (a) zero and (b) static acceleration.

If the net force resulting from an applied quasi-static acceleration on the movable sense frame is different than zero as seen in Figure 2.4-b, the following relation can be derived for the force generated by one quadrature cancellation electrode pair:

$$F_q \approx -\frac{4\varepsilon H_0 X V_{PM} \Delta V}{d_{gap}^2} + \frac{4\varepsilon L_0 H_0 V_{PM}^2 \Delta d_{gap}}{d_{gap}^3} + \frac{4\varepsilon L_0 H_0 \Delta V^2 \Delta d_{gap}}{d_{gap}^3} - \frac{4\varepsilon H_0 X V_{PM} \Delta V \Delta d_{gap}^2}{d_{gap}^4} \quad 2.30$$

Equation 2.30 shows that the force generated by the quadrature cancellation electrodes to suppress the quadrature error decreases (or increases) with the static acceleration acting along the positive y-axis (the negative y-axis). This means that the voltage given to the quadrature cancellation electrodes should be increased (or decrease) to suppress the same amount of the quadrature signal under a static acceleration compared to the stationary case. By combining Equation 2.24 and Equation 2.30, the change in force generated by the quadrature cancellation electrodes, ΔF_q , due to the static acceleration can be expressed as follows:

$$\Delta F_q \approx \frac{4\varepsilon L_0 H_0 V_{PM}^2 a}{d_{gap}^3 w_s^2} + \frac{4\varepsilon L_0 H_0 \Delta V^2 a}{d_{gap}^3 w_s^2} - \frac{4\varepsilon H_0 X V_{PM} \Delta V a^2}{d_{gap}^4 w_s^4} \quad 2.31$$

In Equation 2.3, the first term is more dominant compared to the other terms. Moreover, the first term is linearly proportional with the acceleration. Thus, it is possible to measure the acceleration acting along the sense axis by observing the change in the quadrature cancellation controller output.

It is difficult to analytically determine the effect of the static acceleration on the sense mode springs but the change of the position of the springs with acting acceleration is supposed to be the main reason of the acceleration sensitivity. There is a relation between the amount of the quadrature error and the g -sensitivity of the gyroscope, which will be experimentally shown in Chapter 5. The main reason of the quadrature error is the imperfection in the spring transmitting the drive force from the drive frame to the sense frame [42]. As the gyroscope is subjected to the acceleration, the positions of the drive frame and sense frame with respect to each other may slightly change due to the effect of the accelerations on the springs. Despite the closed loop quadrature cancellation controller, the level of the residual quadrature signal change, resulting in a shift in the rate offset.

2.6.4 Design of Acceleration Cancellation Electrodes

In this thesis study, the acceleration cancellation electrodes are used to generate the electrostatic force which counterbalances the acceleration force acting on the sense mode without affecting the operation of the remaining part of the gyroscope. Figure 2.5 depicts the configuration of the acceleration cancellation electrodes.

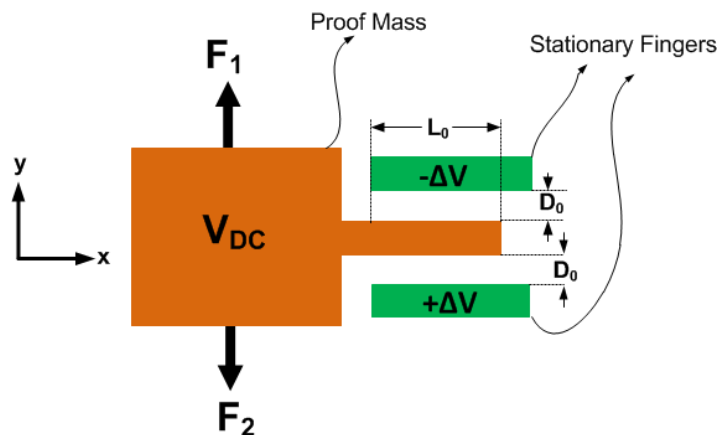


Figure 2.5: Configuration of the acceleration cancellation electrodes.

Considering Figure 2.5, there are two capacitors between the stationary fingers and proof mass, so the electrostatic force acting on the proof mass can be written as

$$F = F_1 + F_2 = \frac{1}{2} \varepsilon_0 \frac{H_0 L_0}{(D_0 - y)^2} (V_{DC} + \Delta V)^2 - \frac{1}{2} \varepsilon_0 \frac{H_0 L_0}{(D_0 + y)^2} (V_{DC} - \Delta V)^2 \quad 2.32$$

For small $y \ll D_0$,

$$F = \frac{1}{2} \varepsilon_0 \frac{H_0 L_0}{D_0^2} (V_{DC} + \Delta V)^2 - \frac{1}{2} \varepsilon_0 \frac{H_0 L_0}{D_0^2} (V_{DC} - \Delta V)^2 \quad 2.33$$

Then, the total force acting on the proof mass in y direction is expressed as;

$$F = 2 \varepsilon_0 \frac{H_0 L_0}{D_0^2} \Delta V V_{DC} \quad 2.34$$

If there is no acceleration force acting on the sense axis of the gyroscope, the voltage applied to the stationary acceleration cancellation electrodes is zero so the forces F_1 and F_2 are equal, resulting in a zero net force acting on the proof mass. Under the static acceleration acting along the y -axis, a nonzero voltage is applied to the acceleration cancellation electrodes, generating a nonzero net force on the proof mass, as shown in Equation 2.34, to balance the acceleration force. The sign of the DC voltage ΔV depends on the direction of the acceleration. Equation 2.34 shows the generated force by two capacitive pairs. In the actual gyroscope operation, the total electrostatic force generated by the acceleration cancellation electrodes can be expressed as

$$F = N \varepsilon_0 \frac{H_0 L_0}{D_0^2} \Delta V V_{DC} \quad 2.35$$

where N represents the total number of acceleration cancellation electrodes, ΔV is the DC potential applied to the acceleration cancellation electrodes and V_{DC} is the the proof mass voltage.

2.7 Finite-Element Simulations

Finite-element method (FEM) is a numerical technique for analyzing the behavior of the complex systems. In this method, the actual problem or mechanical system is modeled in the software environment. Then, the complex system is investigated analyzed using the constructed model. In this study, FEM simulations are conducted to see the mode shapes and corresponding modal frequencies of the MEMS vibratory gyroscope. Coventor, which is a simulation platform optimized for MEMS devices, is used to perform the FEM simulations.

2.7.1 Modal Analysis

Modal analysis is used to determine the mode resonance frequencies of the analyzed device. The drive and sense mode resonance frequencies are important for the gyroscope design, and these frequencies can be determined approximately by the hand calculation. However, it is quite difficult to calculate the resonance frequencies of the higher order modes without using a simulation tool. Thus, the out of plane modes which may deteriorate the operation of the gyroscope are identified by the modal analysis. For a reliable gyroscope operation, the resonance frequencies of the first two mode should be two times less than the frequency of the nearest undesired mode.

Modal simulations have been conducted for the first 10 modes. Table 2.1 provides the corresponding resonance frequencies of the first 10 modes the designed gyroscope. First two ones are the drive and sense mode resonance frequencies, and the other ones are the higher order parasitic mode frequencies which may affect the operation of the gyroscope. Figure 2.6, Figure 2.7 and Figure 2.8 show the drive, sense and undesired higher order mode shapes of the single-mass gyroscope, respectively.

Table 2.1: Modal analysis results of the single-mass fully decoupled gyroscope designed in this work.

Mode#	Resonance Frequency (Hz)	Generalized Mass (kg)
1	13733.5	1.137e-07
2	15899.9	1.011e-07
3	24569.9	7.893e-09
4	24938.1	8.932e-09
5	25906.0	1.351e-08
6	26707.1	6.582e-08
7	29661.6	2.583e-08
8	29826.3	1.180e-08
9	34198.6	2.539e-09
10	37487.5	1.724e-08

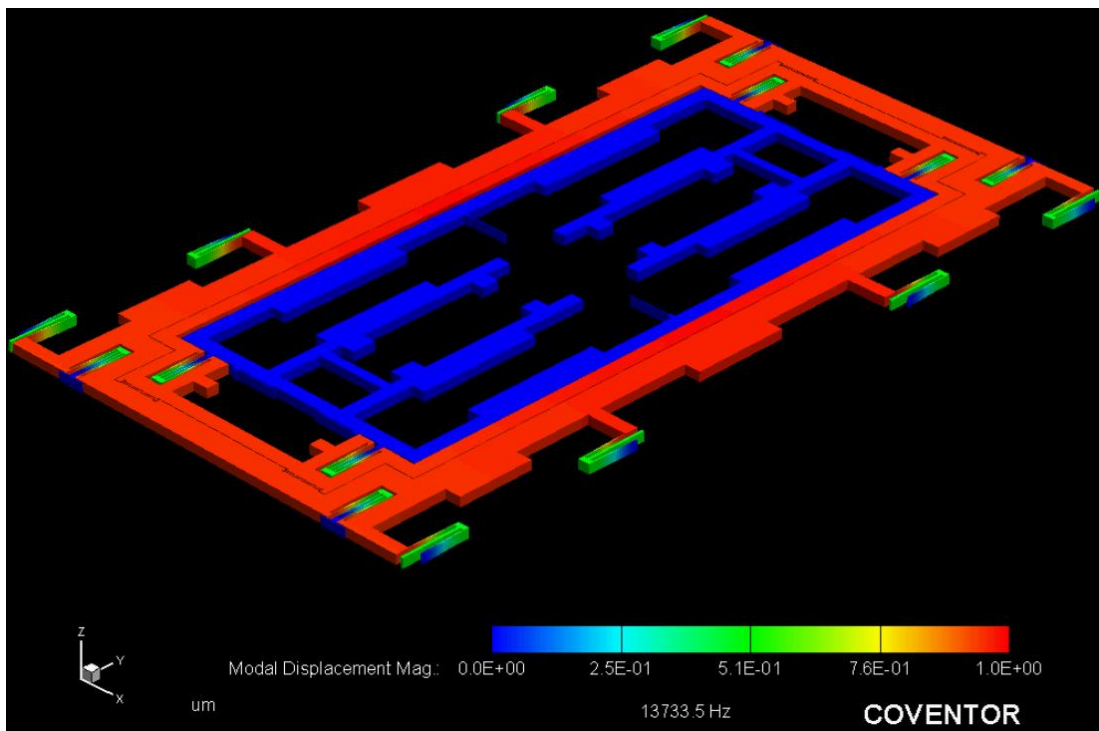


Figure 2.6: Mode shape for drive mode.

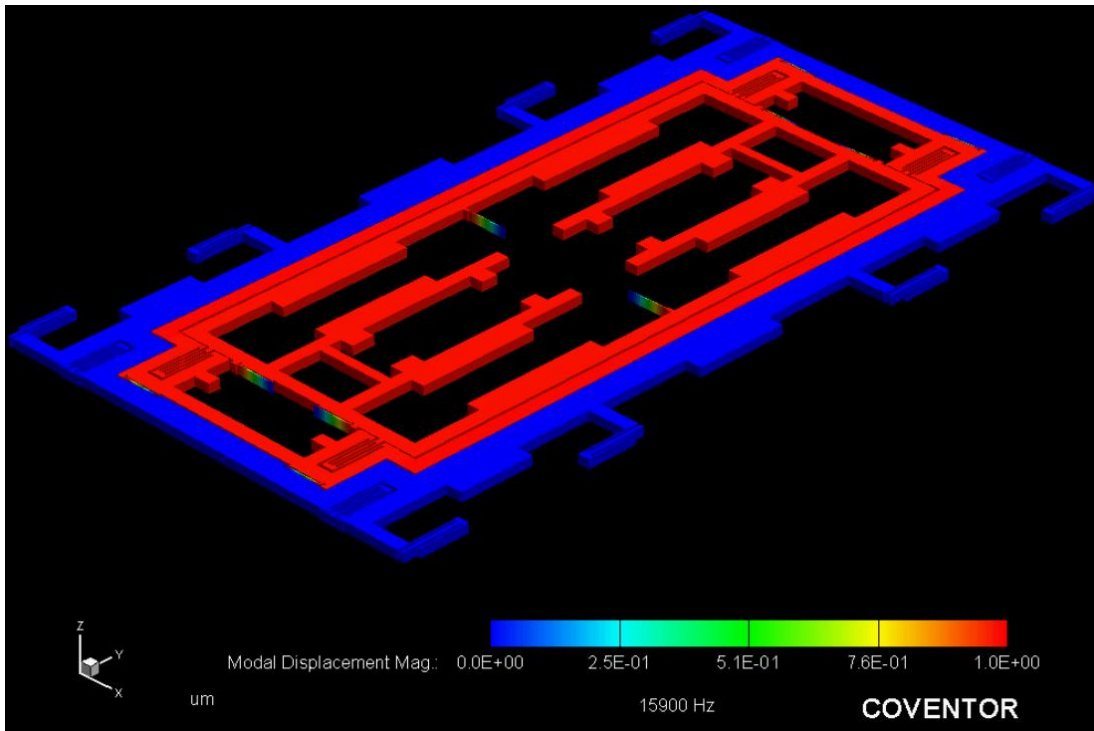


Figure 2.7: Mode shape for sense mode.

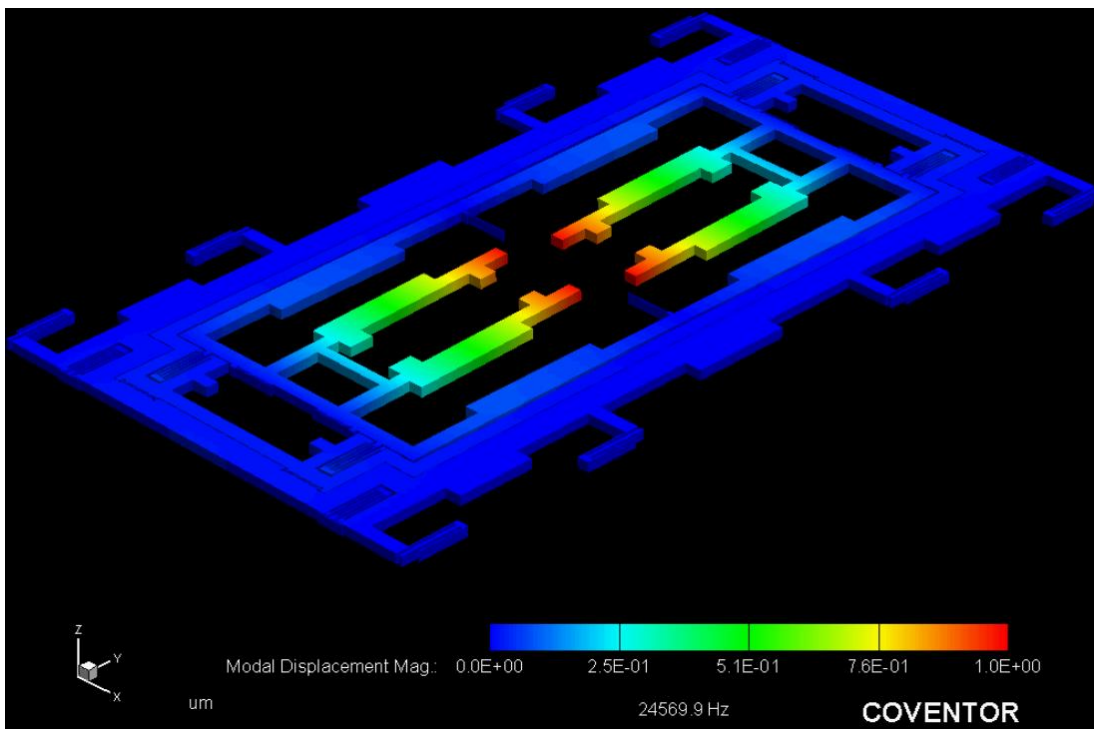


Figure 2.8: Mode shape for the closest undesired higher order mode at 24.6 kHz.

2.8 Summary

This chapter presents the mechanical model of the MEMS gyroscope studied in this thesis. The model parameter calculation, capacitive actuation and sensing mechanism for the MEMS gyroscope are briefly explained. The electrostatic spring effect on the sense resonance frequency is also examined. Then, the effects of the static acceleration on the operation of the sense, force-feedback and quadrature electrodes are investigated in details. Moreover, the design of the acceleration cancellation electrodes for the single-mass fully decoupled gyroscope is explained. Finally, the FEM simulations are conducted to determine the drive and sense mode resonance frequencies.

CHAPTER 3

CONTROL ELECTRONICS FOR MEMS GYROSCOPES

This chapter presents the details of control electronics for MEMS gyroscopes studied in this thesis. Section 3.1 explains the preamplifier stage that converts the output current of the gyroscope to the voltage. Section 3.2 explains the closed loop drive mode controller design. Section 3.3 introduces the closed loop rate sensing mechanism. Section 3.4 provides the design of the closed loop quadrature cancellation controller electronics. Section 3.5 presents the acceleration sensing circuit and closed loop acceleration compensation electronics implemented in this thesis. Section 3.6 gives a brief summary of the chapter.

3.1 Front-End Electronics

The output current of the gyroscope is converted to the voltage and amplified to a desired signal level by a preamplifier and instrumentation amplifier. In the preamplifier stage, transimpedance amplifier (TIA) is used because it is insensitive to parasitic capacitances and contact resistances. It presents low input impedance to the output of the sensor preventing the significant signal loss during the conversion from current to voltage. Figure 3.1 shows the schematic of the transimpedance implemented in this work.

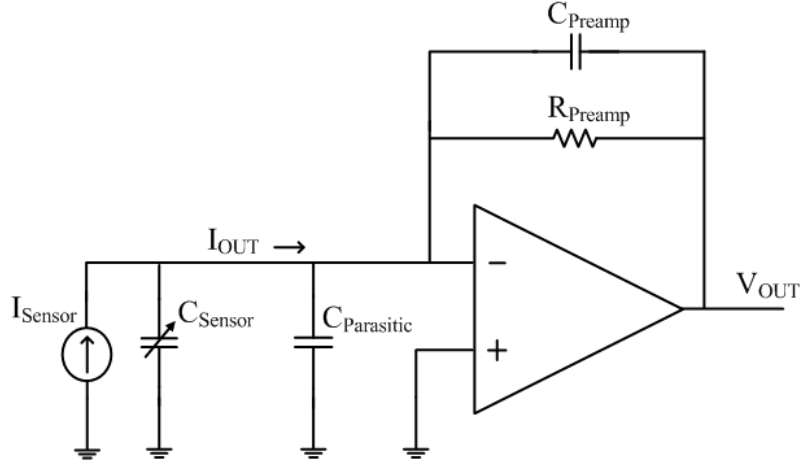


Figure 3.1: Schematic of the transimpedance amplifier implemented in this study.

The input-output relation of the TIA can be expressed as,

$$\left| \frac{V_o(s)}{I_o(s)} \right| = Z_{pre} = \frac{R_{pre}}{1 + sC_{pre}R_{pre}} \quad 3.1$$

In equation 3.1, the multiplication of $sC_{pre}R_{pre}$ determines whether the TIA is resistive or capacitive type. If the multiplication of $sC_{pre}R_{pre}$ is much greater than 1, the type of the preamplifier becomes capacitive. The capacitive type preamplifier is preferred in the sense mode because it provides low noise interface enhancing a high gain with a small resistance. In this case, the current coming from the sensor output is converted to the voltage multiplied by $1/sC_{pre}$.

If the multiplication of $sC_{pre}R_{pre}$ is much smaller than 1, then the type of the preamplifier becomes resistive. Resistive type preamplifier is preferred in the drive mode considering the system design considerations. In the resistive type preamplifier, the function of the capacitor connected parallel to the resistor is to compensate the parasitic effects coming from the sensor and op-amp, which significantly improves the stability of the drive mode oscillation [43]. The disadvantage of the resistive type preamplifier is that obtaining high gain is difficult because the noise of the system increases with increasing resistance.

3.2 Drive Mode Controller Design for MEMS Gyroscope

In the gyroscope operation, the quadrature and Coriolis signals are proportional with the drive displacement and its derivative, respectively. The stability of the drive mode oscillation is crucial for the short and long term stabilities of the gyroscope because any variation in the drive mode oscillation directly affects the scale factor stability, noise and bias performances of the gyroscope. Therefore, the drive mode displacement should be well controlled and kept constant over time for a reliable gyroscope operation.

The operation of the drive mode loop is based on an amplitude controlled positive feedback mechanism. The quality factor of the drive mode reaches to a few tens of thousands in vacuum; thus, it easily enters the self-oscillation by locking its resonance frequency with the help of the positive feedback mechanism. Then, the amplitude of the drive oscillation is adjusted to a desired level by the amplitude control mechanism.

Figure 3.2 shows the block diagram of the closed loop drive mode controller. In this system, the drive signal is first picked from the output of the drive mode preamplifier and demodulated with itself. A resistive type preamplifier is used in the drive mode front-end electronics to minimize the phase error coming from the modulation and demodulation. The output of the demodulator passes through a second-order low pass filter to obtain the DC part of the demodulator signal which gives information about the level of the drive displacement. The output of the low pass filter is compared with a reference DC voltage to adjust the amplitude of the drive displacement. In this step, a band gap reference is used as the reference voltage because the output of the band gap reference is quite insensitive to environmental variations; thus, in that way, the drive mode oscillation is kept constant over time. Then, the error signal is fed to a PI controller which stabilizes the circuit by diminishing the error signal. The DC output of the PI controller is modulated with the drive pick signal. The modulated drive motor signal is a square wave because of the switching type modulator. Since the drive mode system is a high-Q system in vacuum, it behaves like a sharp band-pass filter. Thus, all other harmonics except the first harmonic of the square wave is eliminated by the drive mode of the gyroscope.

Consequently, the amplitude controlled self-oscillation of the drive mode is achieved at the resonance frequency.

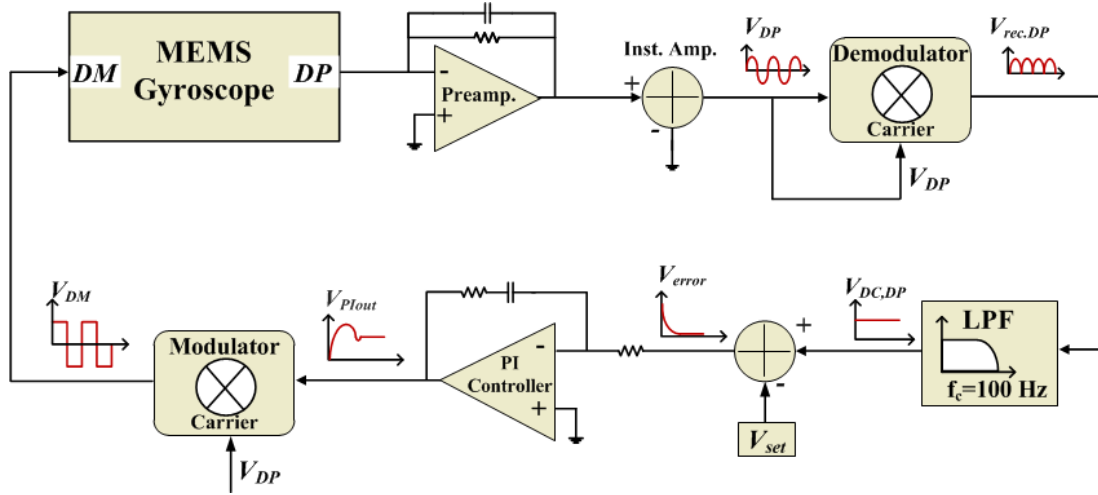


Figure 3.2: Block diagram of the closed loop drive mode controller.

There are important design parameters that should be considered to ensure the stability of the system while constructing the closed loop drive mode control circuit. These parameters are basically settling time, phase margin, overshoot and steady-state error. The settling time defines the response time of the system so it should be decreased for a high performance gyroscope. Moreover, there should be minimum 60° phase margin in the system for a reliable and stable operation. The amount of the overshoot is also critical in the closed loop drive mode controller design because the drive mode displacement should not exceed the maximum allowable range which is $8 \mu\text{m}$ for this study; otherwise, it may damage the gyroscope permanently. The steady-state error in the controller output should go to zero after the system is settled to achieve the desired drive mode displacement, which is satisfied by an integral based controller.

The open loop characteristic of the drive mode should be analyzed by the resonance tests to obtain the sensor parameters such as the resonance frequency, quality factor and gain before designing the closed loop drive mode controller. The resonance test gives the input-output ratio in frequency domain of the drive mode. Figure 3.3 shows the simplified view of the drive mode resonance block. The characteristic of the

drive mode can be explained in three blocks as seen in Figure 3.3. In the first stage, the actuation voltage is converted to the actuation force by the drive motor electrodes. Then, the actuation force provides the sustained displacement of the drive pick electrodes. Finally, the displacement is converted to the current by the capacitive sensing mechanism. The output of the sensor is the current, and this current is transformed to the voltage by the front-end electronics.

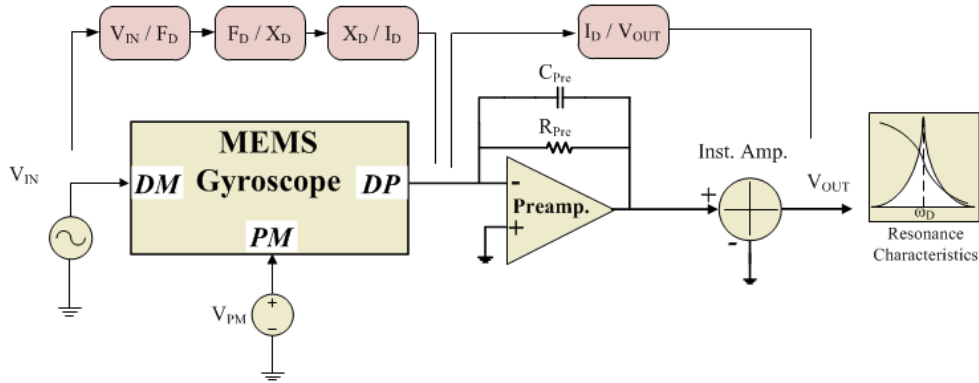


Figure 3.3: Simplified view of the drive mode resonance test schematic.

The open loop transfer function of the drive mode of the gyroscope can be written as the multiplication of the conversion blocks in the following way:

$$\frac{V_{out}(s)}{V_{in}(s)} = \frac{F_D(s)}{V_{in}(s)} \frac{X_D(s)}{F_D(s)} \frac{I_D(s)}{X_D(s)} \frac{V_{out}(s)}{I_D(s)} \quad 3.2$$

Inserting Equation 2.3, 2.15, 2.18 and 3.1 into Equation 3.2, the open loop transfer function of the drive mode can be expressed in terms of the sensor parameters as

$$\frac{V_{out}(s)}{V_{in}(s)} = V_{PM} \frac{\partial C_{DM}}{\partial x} \frac{1/m_D}{\left(s^2 + \frac{w_D}{Q_D} s + w_D^2\right)} V_{PM} \frac{\partial C_{DP}}{\partial x} s Z_{pre} A_{inst} \quad 3.3$$

In Equation 3.3, the multiplication of drive motor $\frac{\partial C_{DM}}{\partial x}$ and drive pick $\frac{\partial C_{DP}}{\partial x}$ sensitivity can be found by equating the resonance gain of the drive mode to the right side of the equation. The mass of the drive mode m_D is found by the hand calculation

using the design parameter of the gyroscope. The proof mass voltage V_{PM} , the preamplifier gain Z_{pre} and the instrumentation amplifier gain A_{inst} are known by the design. The drive mode resonance gain w_D and the drive mode quality factor Q_D are obtained from the resonance test. After finding the multiplication of the $\frac{\partial C_{DM}}{\partial x}$ and $\frac{\partial C_{DP}}{\partial x}$, these terms can be calculated individually according to their ratio in the design. Actually, the sensitivities of the drive motor and drive pick electrodes are adjusted to be equal in this study.

In the drive mode controller, the amplitude of the drive pick signal is controlled to set the drive displacement since the drive displacement is directly proportional with the drive pick signal. As the drive mode displacement gets larger, the noise performance of the gyroscope gets better because the mechanical noise of sensor decreases. However, adjusting the drive mode displacement, the overshoot in the controller output should be also considered for a safe gyroscope operation. Moreover, the drive mode frequency variation with temperature is also critical while adjusting the drive mode displacement. Since the drive pick signal stay constant instead of the drive displacement in Equation 3.4, any change in the resonance frequency directly affects the amplitude of the displacement. But, a few Hz frequency shift is negligible because the resonance frequency of the studied gyroscope is around 11 kHz.

$$V_{DP}(j\omega) = V_{PM} \frac{\partial C_{DP}}{\partial x} j\omega w_D X_D Z_{pre} A_{inst} \quad 3.4$$

The design parameters such as the settling time overshoot and phase margin of the drive mode are adjusted by analyzing the open loop response of the drive mode controller. The drive mode of the gyroscope has a second order model but this model makes the analysis very complicated. Instead, the drive mode dynamics between the modulator and demodulator is simplified to a first order system which is the enveloped model of the modulated system as,

$$H_D(s) = \frac{A_D}{1 + s(2Q_D/w_D)} \quad 3.5$$

where A_D represents the drive mode resonance gain of the gyroscope with the preamplifier stages, Q_D is the quality factor, and w_D is the resonance frequency of the drive mode.

The ‘‘Butterworth’’ type second order low pass filter with a multi-feedback topology is employed in all controllers in this study. The cut-off frequency of the filter is set to 100Hz for the drive mode. The low pass filter gain is adjusted considering the drive displacement. Under these conditions, the open loop transfer function of the drive mode controller can be written as

$$H_{OL}(s) = \frac{A_D}{1 + s(2Q_D/w_D)} K_{Demod} H_{LPF}(s) \frac{K_I(1 + sK_P/K_I)}{s} K_{Mod} \quad 3.6$$

where $H_{LPF}(s)$ is the transfer function the low pass filter, K_{Mod} and K_{Demod} are the gain of the modulator and demodulator, respectively. Moreover, K_I and K_P are the integral and proportional gain of the PI controller. In Equation 3.6, the pole coming from the envelope model of the gyroscope deteriorates the stability of the system. Thus, this pole is cancelled with the zero of the PI controller using the pole-zero cancellation method explained in [44]. After the pole-zero cancellation, the open loop transfer function of the drive mode becomes a third order system which has totally three poles.

The open loop characteristic should be simulated to optimize the phase margin, settling time and overshoot using the real sensor and controller parameters. The drive mode model parameters of the sample gyroscope (Gyro 1207) which are obtained through the resonance test are provided in Table 3.1.

Table 3.1: Drive mode resonance characteristics of the sample gyroscope (Gyro 1207) used during the design of the closed loop drive mode controller for 14 V_{PM}.

Model Parameter (Drive Mode)	Value
Resonance Frequency (f_D)	10813 Hz
Resonance Gain (A_D)	16.3dB (6.5)
Quality Factor (Q_D)	48000

The open loop transfer function in Equation 3.6 can be written using the real sensor and controller parameters as,

$$H_{OL}(s) = \frac{6.5}{1 + s(1/0.71)} * \frac{2}{\pi} * \frac{7.9 * 394784}{s^2 + 881.1s4394784} * \frac{K_I(1 + sK_P/K_I)}{s} * \frac{4}{\pi} \quad 3.7$$

As seen in Equation 3.7, the gain of the demodulator and low pass filter are adjusted to 1 and 7.9, respectively, to achieve 780 mV peak-to-peak drive pick signal which corresponds to 4 μ m drive displacement for the sample gyroscope. The factors of $2/\pi$ and $4/\pi$ are the RMS value of the rectified drive pick signal and the first harmonic of the square wave drive motor signal, respectively. After a few iterations in MATLAB, K_P is optimized as 5.4 and K_I is optimized as 3.8 to achieve the sufficient phase margin, minimum settling time and minimum overshoot for the design. Figure 3.4 depicts the bode diagram of the drive mode open loop transfer function, showing that the phase margin of the system is greater than 60°.

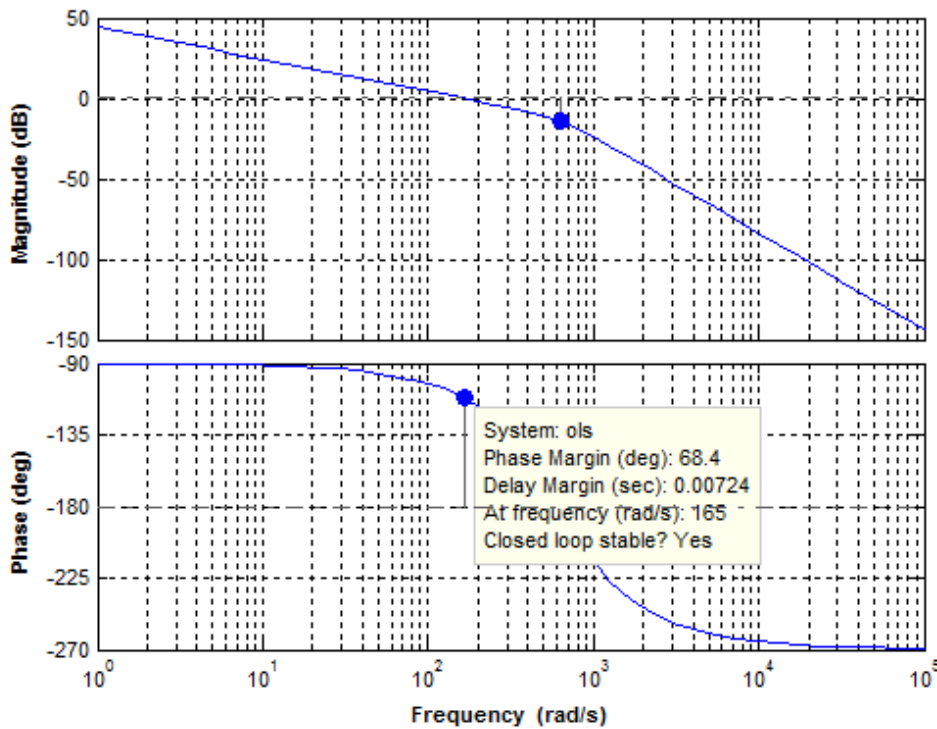


Figure 3.4: Bode diagram of the drive mode open loop transfer function.

The settling time and overshoot of the closed loop drive mode system can be obtained by analyzing the step response of the open loop transfer function in MATLAB. Figure 3.5 depicts the step response of the closed loop drive mode controller. As seen in Figure 3.5, the settling time of the system is around 16 msec without any overshoot.

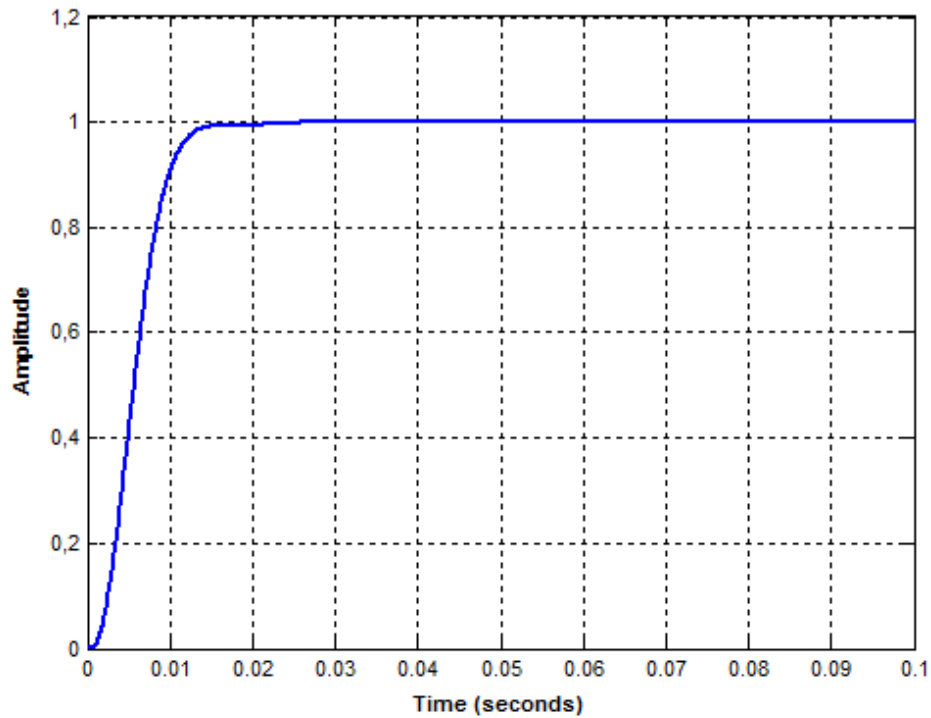


Figure 3.5: Step response of the closed loop drive mode controller.

The transient behavior of the closed loop drive control system is analyzed in MATLAB SIMULINK by modeling the drive system using the second order sensor model with the real sensor and controller values. Figure 3.6 shows the SIMULINK model for the closed loop drive mode controller circuit. Figure 3.7 depicts the transient behavior of the drive pick signal obtained using the SIMULINK model in Figure 3.6. As seen in Figure 3.7, the settling time of the system is around 15 msec which is consistent with the open loop analysis. Moreover, the peak to peak value of the drive pick signal is 780mV as calculated for 4 μm drive displacement.

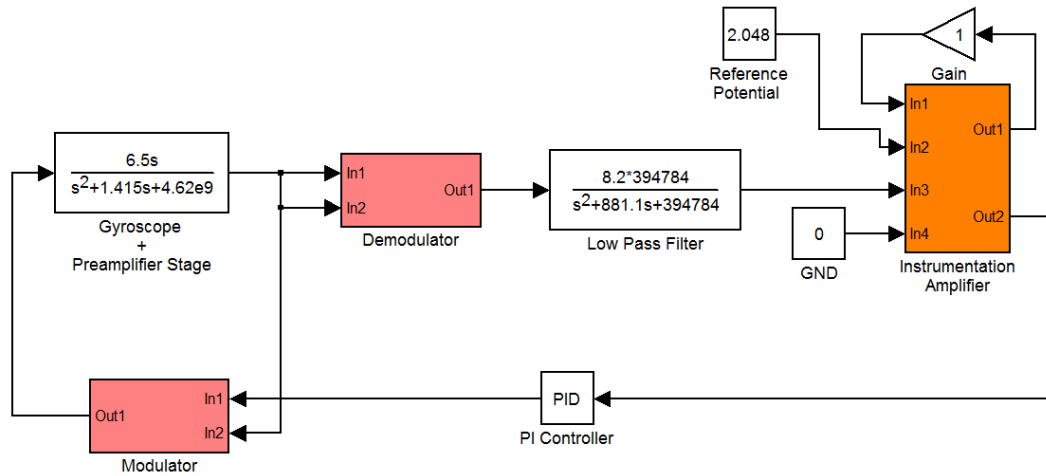


Figure 3.6: SIMULINK model of the closed loop drive mode control electronics for the sample gyroscope.

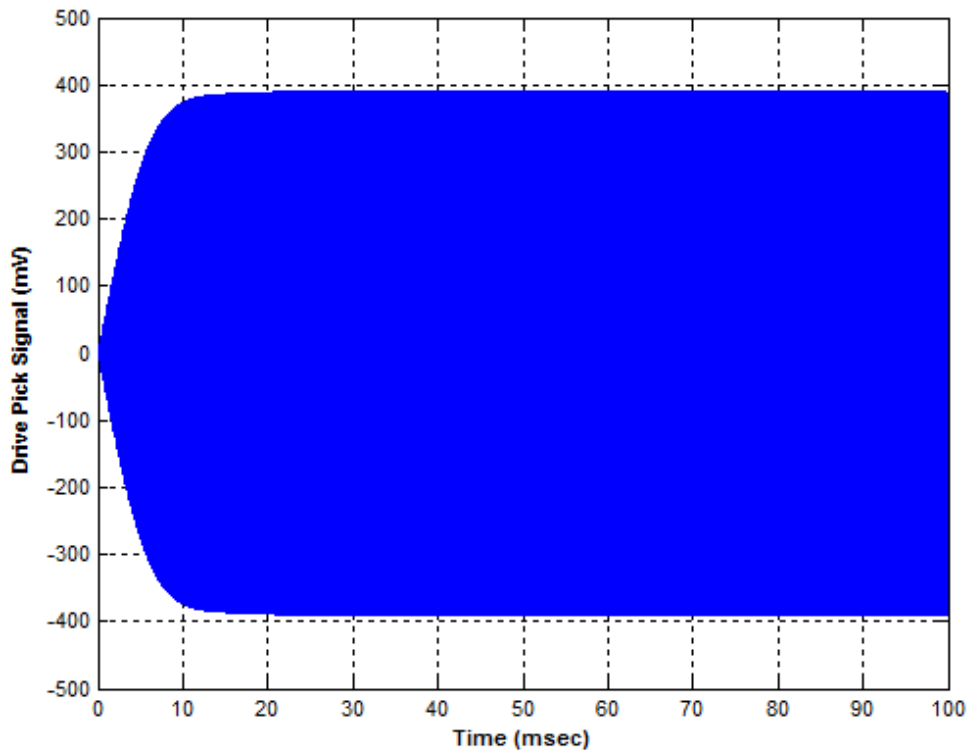


Figure 3.7: Drive pick signal obtained using the realistic SIMULINK model of the drive mode control electronics.

3.3 Design of Closed Loop Rate Sensing Mechanism

The purpose of the closed loop rate sensing system is to obtain the rate information by preventing the sense mode displacement of the gyroscope caused by Coriolis acceleration. In the open loop operation of the gyroscope, the bandwidth of the system is restricted by the mechanical bandwidth which is around a few Hz. Moreover, the scale factor may deviate due to the drift of the quality factor with time and the change of the capacitive gap spacing with the angular rate input. To get over the issues related with the open loop rate sensing mechanism, the closed loop rate sensing mechanism which does not deteriorate the scale factor stability and bandwidth is preferred to sense the induced Coriolis acceleration in the controller electronics of the gyroscope.

Force-feedback electrodes are generally preferred in the closed loop gyroscope operation to stop the movement of the proof mass caused by Coriolis force. The proposed closed loop rate sensing mechanism keeps the sense mode of the gyroscope stationary by generating the electrostatic force with the aid of the force-feedback electrodes to balance the Coriolis force. The condition to stop the sense mode displacement due to Coriolis acceleration is derived in [6] as

$$V_{PM} \frac{\partial C_{FF}}{\partial y} V_{FF} = 2m_{PM} \Omega j \omega_D X_D \quad 3.8-a$$

$$V_{FF} = \frac{2m_{PM} \Omega j \omega_D X_D}{V_{PM} \frac{\partial C_{FF}}{\partial y}} \quad 3.8-b$$

In Equation 3.8, $\partial C_{FF} / \partial y$ represents the sensitivity of the force-feedback electrodes, and V_{FF} denotes the amplitude of the AC signal applied to the force-feedback electrodes. As seen in Equation 3.8, the amplitude of V_{FF} is directly proportional with the applied rate, and it does not depend on the ambient conditions. Therefore, the scale factor of the gyroscope output is more stable in the closed loop operation compared to the open loop operation. Moreover, the bandwidth of system can be controlled independently from the mechanical sensor parameters with the help of the controller.

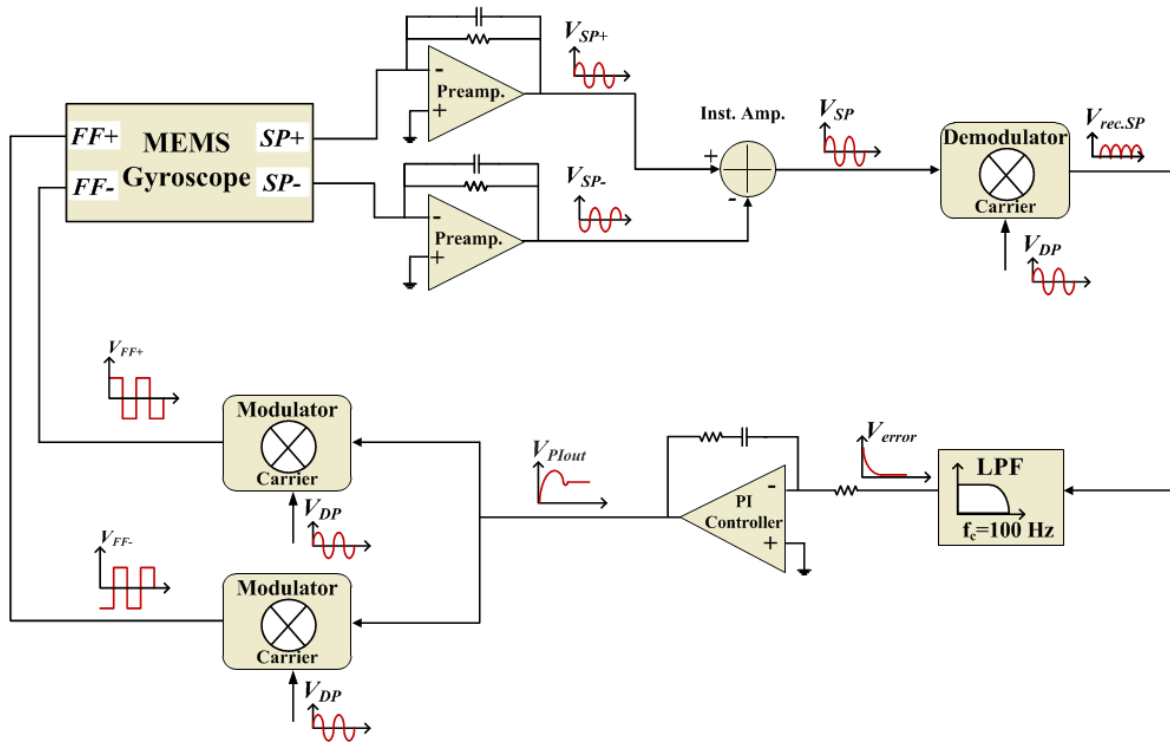


Figure 3.8: Block diagram of the closed loop sense mode controller for the mismatch operation.

Figure 3.8 shows the block diagram of the closed loop controller for the sense mode. In this system, the capacitive preamplifiers pick the sense mode signals caused by the Coriolis force differentially. Then, the sense signals are demodulated with the drive signal in the mismatch operation using the phase sensitive modulation and passes through the low-pass filter. The low pass filter output is fed to the controller. This controller generates a DC voltage proportional with the amplitude of the angular rotation. The output of the controller is modulated with the drive signal, and the modulated signals are differentially applied to the force-feedback electrodes in the gyroscope. In this system, the rate information is extracted from the output of the controller using a buffer or amplifier.

The open loop characteristic of the transfer function should be examined to optimize the controller parameters before analyzing the closed loop behavior of the system. The open loop transfer function of the sense mode can be expressed as,

$$H_{OL}(s) = \frac{V_{SP}(s)}{V_{FF}(s)} K_{Demod} H_{LPF}(s) \frac{(K_P s + K_I)}{s} K_{Mod} \quad 3.9$$

In Equation 3.10, K_{Demod} represents the gain of the demodulator, K_{Mod} denotes the gain of the modulator, $H_{LPF}(s)$ is the transfer function of the low pass filter. Since the gyroscope is operated in the mismatch condition, the second order model of the sense mode cannot be simplified to the first order model in this case. Instead, the sense mode dynamics is modeled as a constant gain stage under mismatch condition. The transfer function of the sense mode can be written as,

$$\frac{V_{SP}(s)}{V_{FF}(s)} = V_{PM} \frac{\partial C_{FF}}{\partial y} \frac{1/m_S}{\left(s^2 + \frac{w_S}{Q_S} s + w_S^2\right)} V_{PM} \frac{\partial C_{SP}}{\partial y} s Z_{pre} A_{inst} \quad 3.10$$

In Equation 3.10, $\frac{\partial C_{FF}}{\partial y}$ denotes the sensitivity of the force feedback electrodes and $\frac{\partial C_{SP}}{\partial y}$ represents the sensitivity of the sense pick electrodes. The multiplication of these two terms can be extracted from the resonance tests. At the off resonance condition, the $V_{SP}(s)/V_{FF}(s)$ can be considered as a constant gain stage, and its gain is calculated by inserting the drive mode resonance frequency instead of the frequency term in Equation 3.10. Then using the real sensor and circuit parameters, the open loop transfer function of the sense mode for the sample gyroscope can be written as,

$$H_{OL}(s) = 0.68 * \frac{4}{\pi} * \frac{6.56 * 394784}{s^2 + 881.1s + 394784} * \frac{(K_P s + K_I)}{s} * \frac{4}{\pi} \quad 3.11$$

In Equation 3.11, the first $\frac{4}{\pi}$ denotes the rms value of the rectified sinus with a demodulator gain of 2, the second $\frac{4}{\pi}$ represents the first harmonic of the square wave force feedback signal. The low pass filter has a gain of 6.56 and a cut-off frequency of 100Hz. An integral controller is preferred instead of the PI controller because introducing a zero to this system deteriorates the response of the low pass filter. After a few iterations in MATLAB, K_P is set to zero and K_I is optimized as 18 to achieve

the sufficient phase margin, minimum settling time and minimum overshoot for the design.

Figure 3.9 shows the bode plot of the open loop sense mode system. The system has a phase margin of 69° which is sufficient for a reliable gyroscope operation. Figure 3.10 shows the step response of the closed loop sense mode system. The settling time of the system is about 16 msec, which ensures that the bandwidth of the system is wider than 60 Hz.

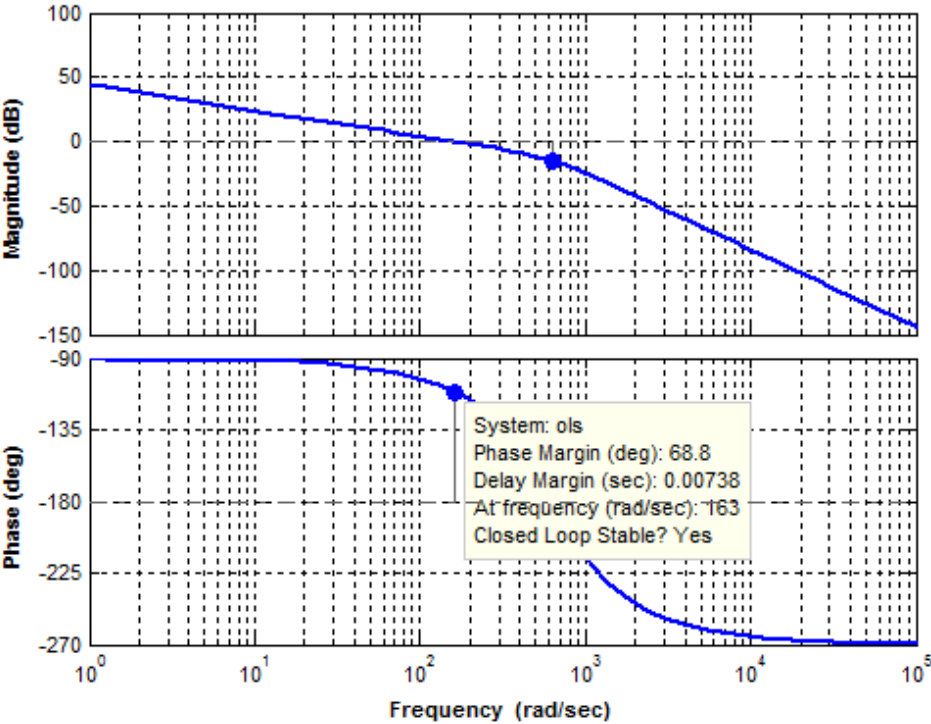


Figure 3.9: Bode diagram of the sense mode open loop transfer function.

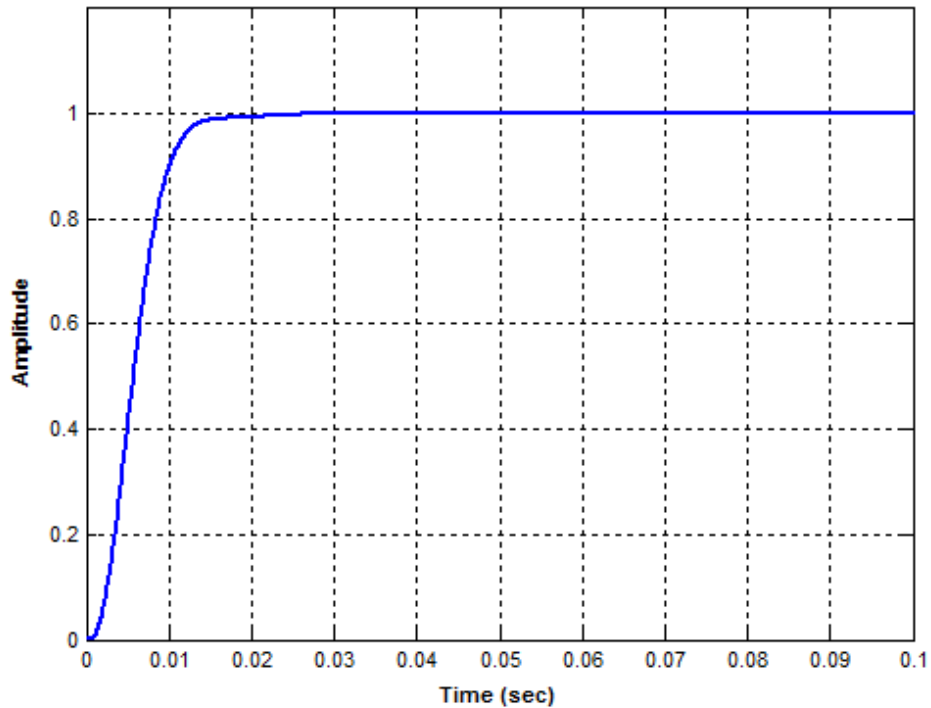


Figure 3.10: Step response of the closed loop sense mode controller.

The transient behavior of the closed loop sense mode control system is analyzed in MATLAB SIMULINK by modeling the sense system using the second order sensor model with the real sensor and controller values. Figure 3.11 shows the SIMULINK model of the closed loop sense mode controller circuit. In this model, the quadrature cancellation loop and acceleration control loop are also integrated to the system to take into account the effects of the other control loops on the force-feedback loop. During the simulation, $1^\circ/\text{s}$ angular rate input is applied to the gyroscope system. Figure 3.12 shows the response of the gyroscope rate output to the applied angular rate input, which corresponds to the scale factor of $2.1\text{mV}/^\circ/\text{s}$. Similarly, Figure 3.13 depicts the transient behavior of the sense pick signal as a response to the applied angular rate input. The sense pick signal carries information about the sense mode displacement. As the time passes, the amount of the sense pick signal diminishes thanks to the closed loop sense mode controller, which shows the effectiveness of the closed loop sense mode controller.

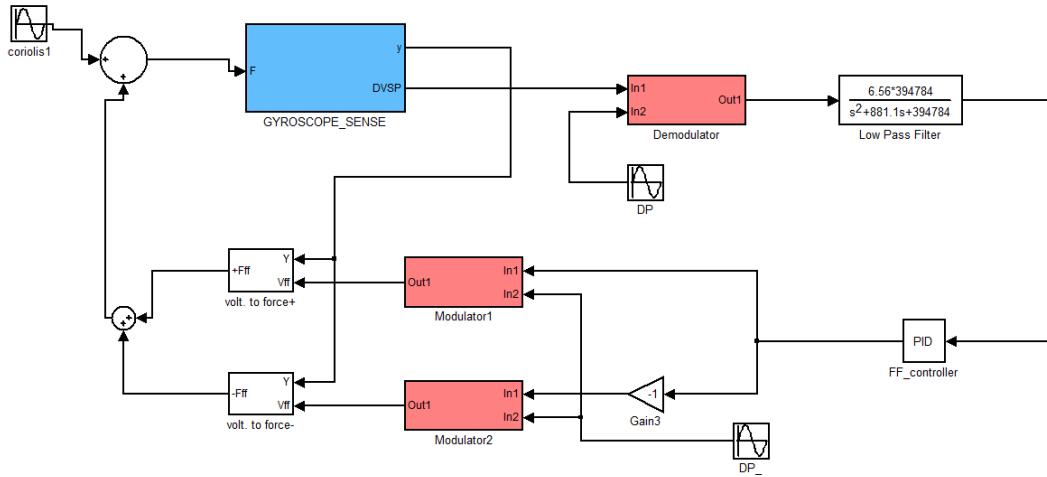


Figure 3.11: SIMULINK model of the closed loop sense mode control electronics for the sample gyroscope.

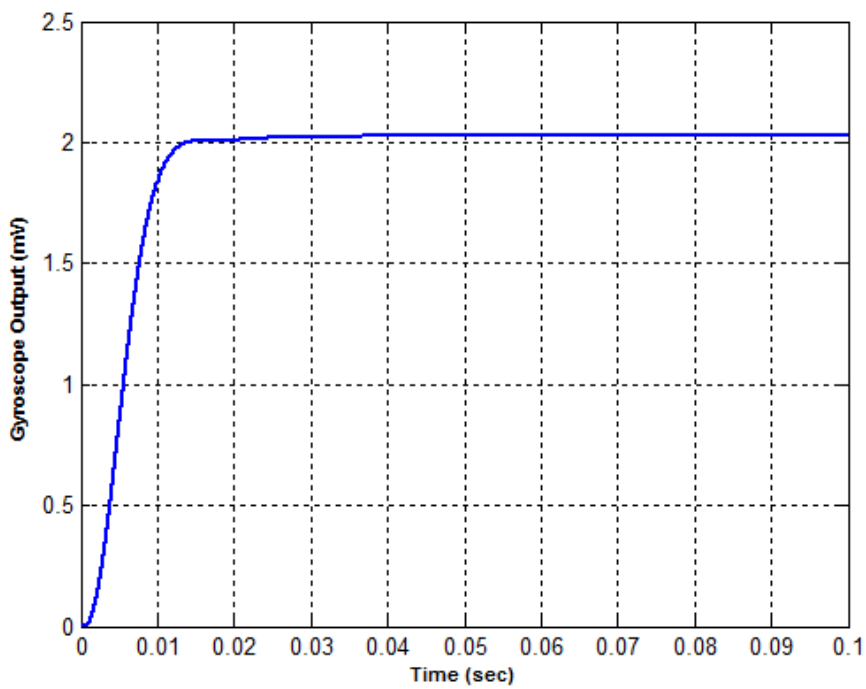


Figure 3.12: Settling behavior of the gyroscope rate output in response to 1°/s angular rate input.

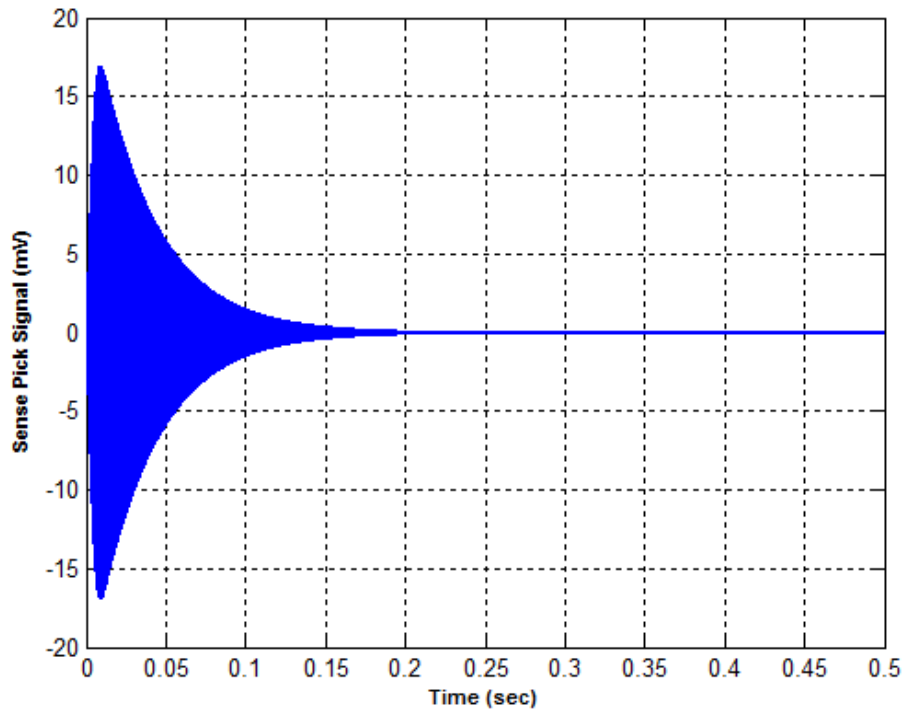


Figure 3.13: Transient behavior of the sense pick signal in response to $1^\circ/\text{s}$ angular rate input.

Bandwidth is also a critical design parameter for the sense mode controller, and it should be considered during the simulation. To measure the bandwidth of the closed loop controller, a sinusoidal angular rate input, whose frequency varies between 0 Hz and 70 Hz in time, is applied to the gyroscope system as a Coriolis signal. Figure 3.14 shows the frequency response characteristic of the rate output as a response to the varying frequency rate input. By using Figure 3.14, the bandwidth of the closed loop sense mode control system is calculated to be 60 Hz which corresponds to 3dB point on the graph.

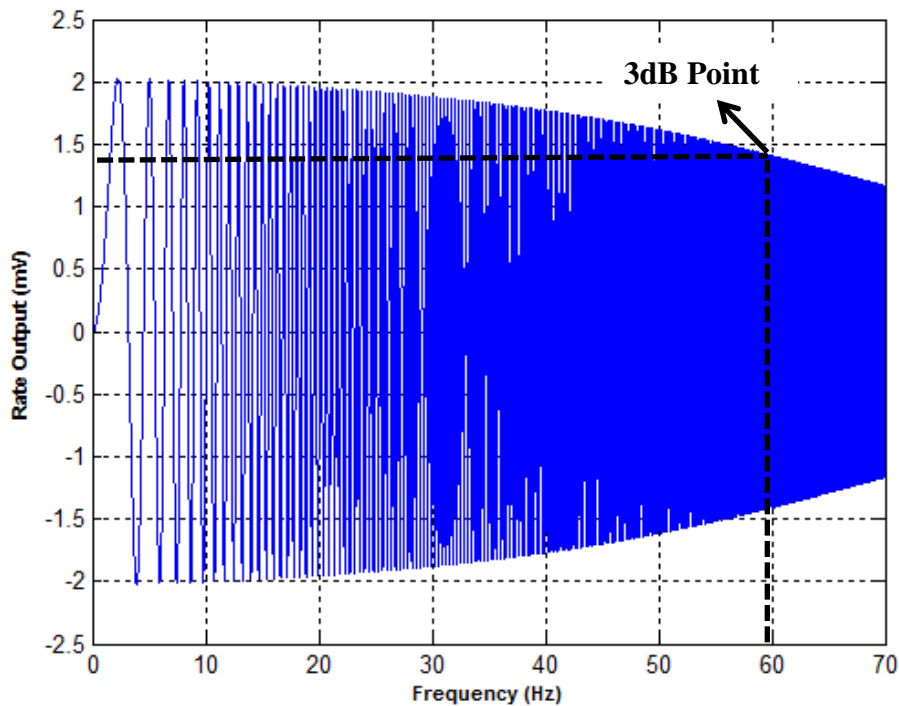


Figure 3.14: Response of the gyroscope rate output to a time varying rate which has amplitude of $1^\circ/\text{s}$.

3.4 Design of Quadrature Control Electronics

The operation of the quadrature control electronics relies on the phase sensitive modulation, which is similar to control mechanism used in the force feedback loop. Figure 3.15 depicts the block diagram of the quadrature control electronics. As opposed to the force feedback control loop, the sense pick signal including the quadrature signal is demodulated with the 90° phase shifted version of the drive pick signal in the quadrature control electronics. Then, the demodulated signal passes through the low pass filter. The low pass filter output is compared with a reference voltage, which enables to adjust the amount of the quadrature signal because a level controllable residual quadrature signal should always exist in the system for the operation of the acceleration cancellation electronics. The resultant error signal is given to the controller which produces a DC voltage that is applied to the quadrature cancellation electrodes differentially.

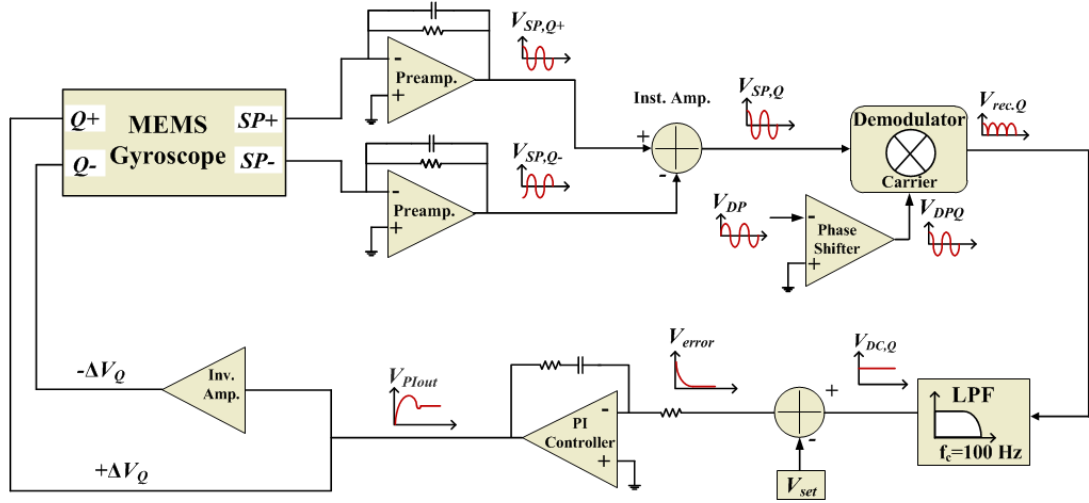


Figure 3.15: Block diagram of the closed loop quadrature cancellation controller for the mismatch operation.

The quadrature controller system utilizes the electrostatic forces which are produced by the differential quadrature cancellation electrodes. These forces generate a rotational torque on the proof mass to suppress the quadrature error. The electrostatic force generated by the quadrature cancellation is derived in [42] as

$$F_Q = n \frac{4V_{PM}\epsilon X H_0 \Delta V}{D_0^2} \quad 3.12$$

where n is the number of the quadrature cancellation electrode set, ΔV is the potential applied to the quadrature electrodes, H_0 and D_0 are the height and gap spacing of the quadrature electrodes, respectively.

The open loop characteristic of the system should be studied to determine the appropriate controller values before analyzing the closed loop behavior of the quadrature cancellation electrodes. The generated force by the quadrature cancellation electrodes acts on the sense mode of the gyroscope so the open loop transfer function of the system can be written as follow:

$$H_{OL}(s) = \frac{V_{SP}(s)}{F_Q(s)} K_{Demod} H_{LPF}(s) \frac{K_I(1 + sK_P/K_I)}{s} K_{Quad} \quad 3.13$$

In Equation 3.13, K_{Demod} is the gain of the demodulator, $H_{LPF}(s)$ is the transfer function of the low pass filter and K_{Quad} is the gain of the quadrature configuration which can be calculated by dividing F_Q by quadrature potential ΔV in Equation 3.12. Since the gyroscope is operated in the mismatch condition, $V_{SP}(s)/F_Q(s)$ is modeled as a constant gain stage using a similar approach as in the sense control loop. Using the appropriate conversion mechanisms, the gyroscope model for the quadrature loop can be expressed as

$$\frac{V_{SP}(s)}{F_Q(s)} = \frac{1/m_s}{\left(s^2 + \frac{w_s}{Q_s}s + w_s^2\right)} V_{PM} \frac{\partial C_{SP}}{\partial y} s Z_{pre} A_{inst} \quad 3.14$$

In Equation 3.13, $\frac{\partial C_{SP}}{\partial y}$ represents the sensitivity of the sense pick electrodes, and the other parameters are known from the resonance tests. In Equation 3.13, the gain of $V_{SP}(s)/F_Q(s)$ is calculated by inserting the drive mode resonance frequency instead of the frequency term in Equation 3.14. Then using the real sensor and circuit parameters, the open loop transfer function of the quadrature cancellation loop for the sample gyroscope can be written as,

$$H_{OL}(s) = 4.5 * 10^6 * \frac{2}{\pi} * \frac{1 * 394784}{s^2 + 881.1s + 394784} * \frac{(K_P s + K_I)}{s} * 1.9 * 10^{-7} \quad 3.15$$

Where $\frac{2}{\pi}$ denotes the rms value of the rectified sinus with a unity gain modulator. The low pass filter has the cut-off frequency of 100Hz with the unity gain. Using a similar approach with the sense mode controller design, an integral control is implemented instead of the PI controller not to degrade the low pass characteristic of the system. After a few iterations in MATLAB, K_P is set to zero and K_I is optimized as 52 to achieve the sufficient phase margin, minimum settling time and minimum overshoot for the design.

Figure 3.16 shows the bode plot of the open loop sense mode system. The system has a phase margin of 70 which is sufficient for a reliable gyroscope operation. Figure 3.17 depicts the step response of the closed loop sense mode system. The system has a settling time about 25 msec.

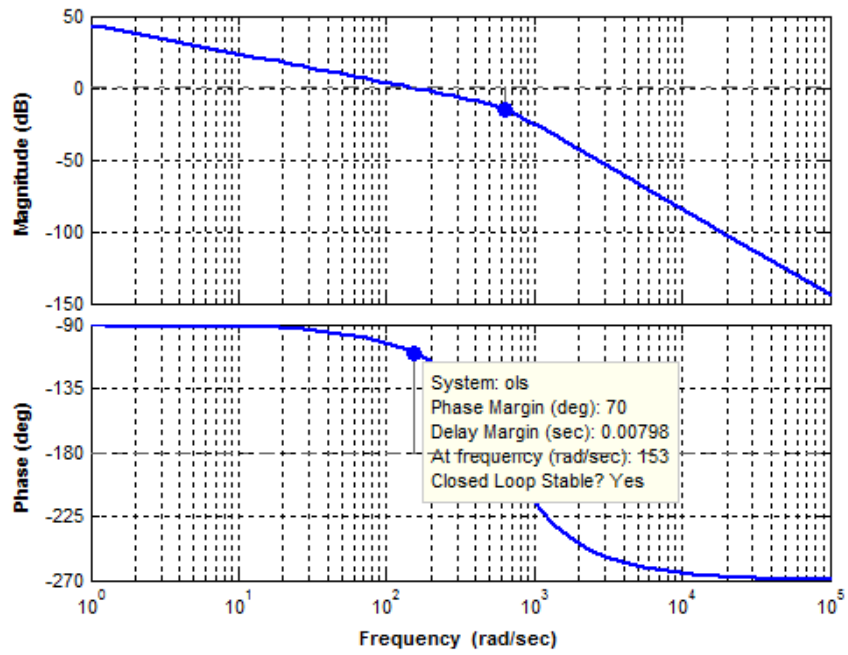


Figure 3.16: Bode diagram of the open loop quadrature control electronics.

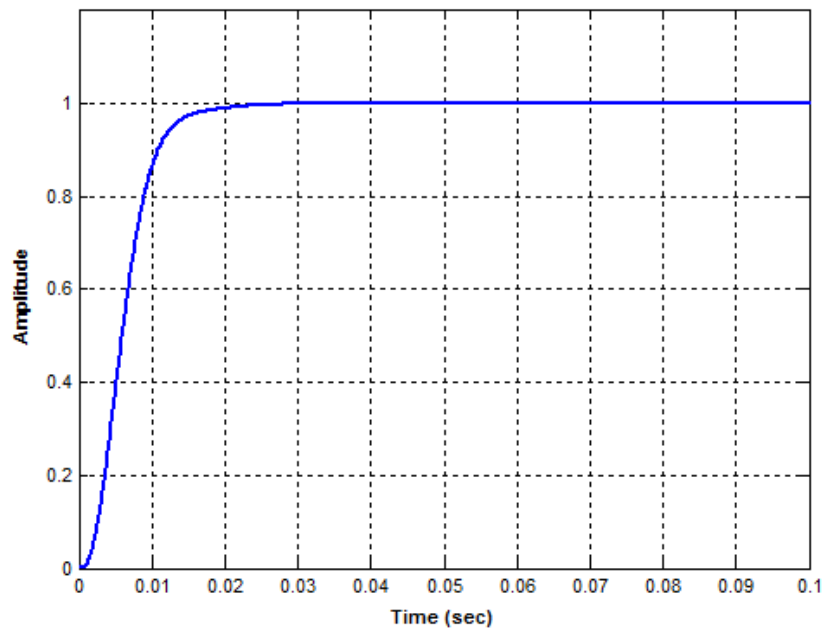


Figure 3.17: Step response of the closed loop quadrature cancellation controller.

The transient behavior of the closed loop quadrature cancellation system is analyzed in MATLAB SIMULINK by modeling the sense system using the second order sensor model with the real sensor and controller values. Figure 3.18 depicts the SIMULINK model for the closed loop quadrature cancellation circuit. In this model, 50 nN quadrature error is intentionally applied to the gyroscope system to observe the closed loop behavior of the quadrature cancellation controller.

Figure 3.19 depicts the transient behavior of the sense pick signal in the presence of the quadrature error. The sense pick signal carries information about the sense mode displacement, which maximizes while system is reaching to steady-state, and then it diminishes thanks to the closed loop quadrature cancellation controller.

Figure 3.20 shows the transient behavior of the output of the quadrature cancellation electrodes which generates quadrature force to suppress the quadrature error. These electrodes generate approximately 50 nN force out of phase with the quadrature error, which suppresses the quadrature error exists in the system.

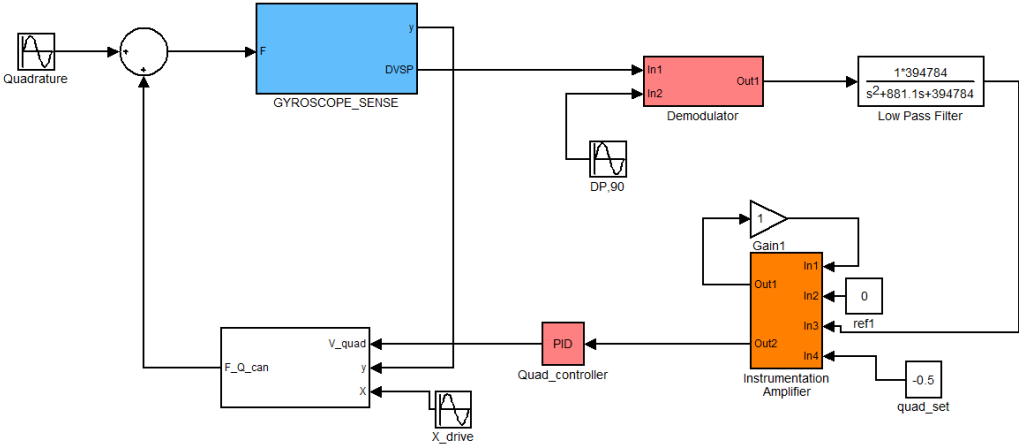


Figure 3.18: SIMULINK model of the closed loop quadrature cancellation control electronics for the sample gyroscope.

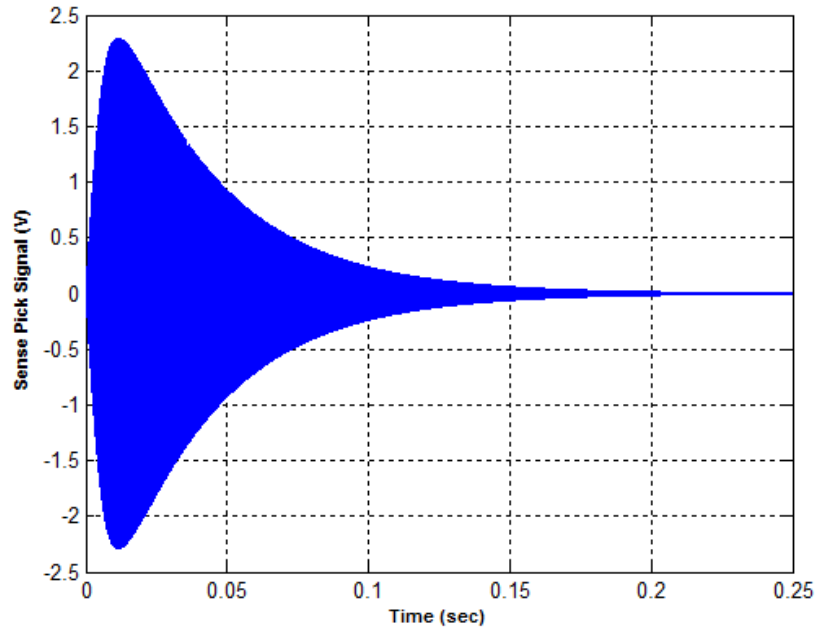


Figure 3.19: Transient behavior of the sense pick signal in the presence of the quadrature error and closed loop quadrature control electronics.

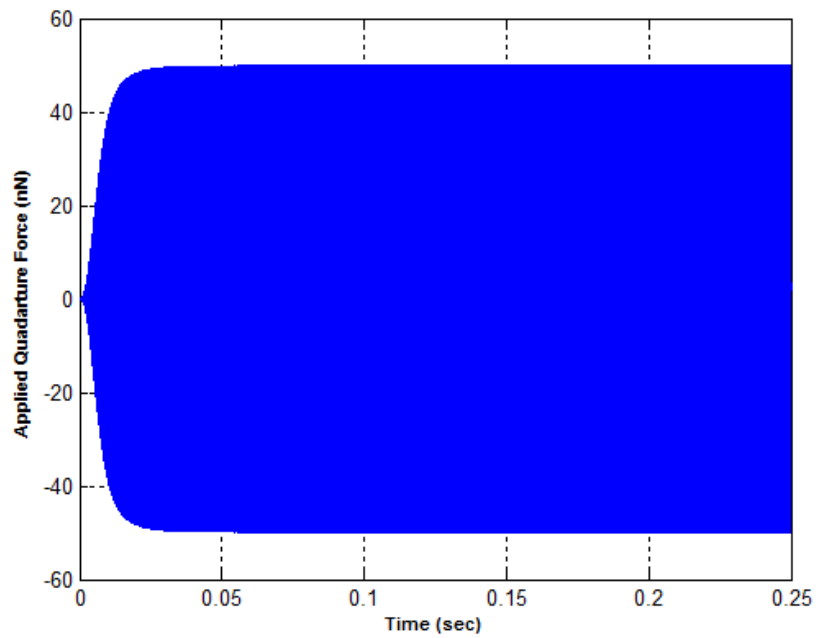


Figure 3.20: Applied quadrature force to suppress the quadrature error exists in the system.

3.5 Design of Acceleration Sensing and Compensation Electronics

The proposed acceleration sensing and compensation methods rely on the utilization of the amplitude difference information between the residual quadrature signals on the differential sense-mode electrodes. In these methods, the amplitudes of the sustained differential quadrature signals are compared to measure the linear acceleration acting on the sense-axis of the gyroscope, which requires no external accelerometer.

During the gyroscope operation, the sense mode frame is kept stationary with the aid of the force feedback electronics in the absence of the external acceleration, as depicted in Figure 2.4-a. However, it is seen from Figure 2.4-b that when the net force resulting from an applied quasi-static acceleration on the movable sense frame is different than zero, the capacitive gap spacing decreases on one side and increases on the other, resulting in a shift at the sense-mode vibration axis. This shift causes a variation at the amplitudes of the quadrature signals on the differential sense-mode electrodes, i.e., the amplitude of the quadrature signal increases (or decreases) with a decreasing (or increasing) capacitive gap under the condition of an applied static acceleration condition compared to the case when there is no acceleration. By comparing the amplitudes of the sustained differential residual quadrature signals, the amplitude of the acceleration is measured.

This thesis study is conducted in three phases. In the first phase of the study, only the acceleration sensing electronics is implemented to measure the acceleration acting on the sense axis of the gyroscope. In this method, the acceleration cancellation electronics is operated in open loop mode so no feedback is given to the gyroscope to eliminate the effect of the acceleration during the operation. By finding an experimental relation between the rate and acceleration outputs of the gyroscope in response to the applied quasi-static acceleration, the effect of the static acceleration on the gyroscope output is compensated by external calibration techniques. In the second phase of the study, a feedback voltage is applied to the sense mode electrodes by using the non-inverting inputs of the sense mode preamplifiers to stop the motion caused by the static acceleration on the sense axis, in addition to the acceleration sensing circuit. In this method, the sense mode electrodes are utilized for both sensing and actuation purposes. In the third phase of the study, the dedicated

acceleration cancellation electrodes are employed to isolate the operation of the acceleration control electronics from the remaining part of gyroscope system. In this method, the acceleration force acting along the sense axis of the gyroscope is counterbalanced in operation by generating an opposite force with the aid of the dedicated electrodes.

3.5.1 Open Loop Acceleration Compensation Electronics

The operation principle of the acceleration sensing mechanism is mainly based on the comparison of the amplitudes of the residual quadrature signals, directly picked from the differential sense-mode electrodes. Figure 3.21 shows the block diagram of the acceleration sensing electronics. In this method, the amplitudes of the sustained residual quadrature signals on the differential sense mode electrodes are compared using a summing amplifier. The output of the summing amplifier is then demodulated with the drive channel output (DP), and the resulting rectified signal is passed through a low pass filter (LPF) to get the amplitude information of the acceleration. It should be noted that the amplitude of the sustained quadrature signals of the gyroscope is adjusted to be a certain level to set the scale factor of the acceleration output of the gyroscope to a known level and to prevent saturation at the force-feedback electronics.

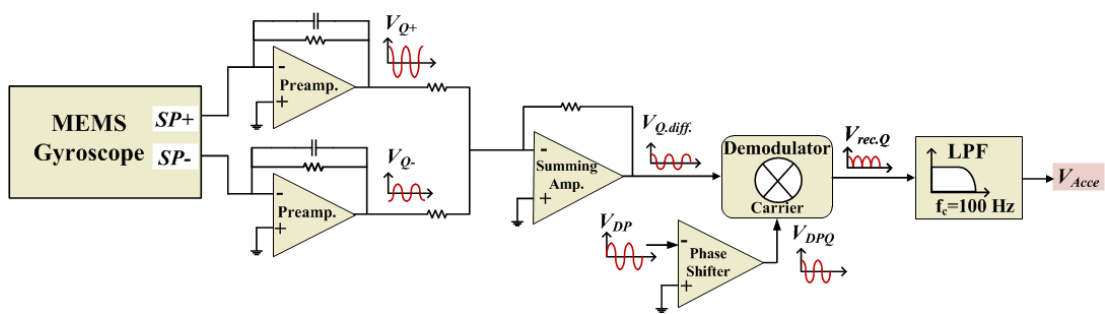


Figure 3.21: Block diagram of the acceleration sensing electronics for the mismatch operation.

The main motivation behind the acceleration sensing and compensation method is to sense the static acceleration acting on the sense-axis and eliminate the effect on the acceleration on the gyroscope output using the experimental relation between the

acceleration and gyroscope output. Referring to Figure 3.21, the acceleration output which is picked from the low pass filter output can be written as,

$$V_{acce} = (I_{SP+} + I_{SP-})Z_{pre}A_{summing} \frac{2}{\pi} \quad 3.16$$

where I_{SP+} and I_{SP-} are the differential sense mode channel output currents, $\frac{2}{\pi}$ denotes the rms value of the rectified sinus with a unity gain modulator, and Z_{pre} and $A_{summing}$ are the gain of the preamplifier and summing amplifier stages, respectively. Combining Equation 2.4, 2.18, 3.14 and 3.16, the acceleration output of gyroscope can be indicated in terms of the applied acceleration and known parameters for the small acceleration displacement as,

$$V_{acce} \cong V_{quad_set} \frac{A_{summing}}{A_{instr}} \frac{2a}{D_{gap}w_s^2} \quad 3.17$$

where V_{quad_set} is the offset voltage given to the input of the quadrature controller op-amp, A_{instr} is the gain of the instrumentation amplifier used in the sense mode electronics, D_{gap} is the gap spacing of the sense mode electrodes, w_s is the sense mode resonance frequency, and a is the amplitude of the acceleration acting on the sense axis of the gyroscope. Equation 3.17 implies that the acceleration output of the gyroscope is linearly proportional with the amplitude of the static acceleration for the small acceleration displacement.

Although the acceleration acting along the sense-axis affects the rate output of the gyroscope in different ways as mentioned in Section 2.6, it is possible to extract a relation between the rate output and acceleration experimentally. For small amplitudes of acceleration, the change in the capacitive electrode gaps would also be small. Thus, a linear relation can be assumed between the rate output variation of the gyroscope and the applied acceleration. The same assumption is also valid for the acceleration output, as shown in Equation 3.17. Under these assumptions, the rate and acceleration outputs of the gyroscope can be represented as follows;

$$V_{rate} \cong A.a + B.\Omega + Vrateroffset \quad 3.18-a$$

$$V_{acce} \cong C.a + D.\Omega + Vacce.offset$$

where “ a ” is the external acceleration and “ Ω ” is the input angular rate. A is the g -sensitivity of the gyroscope, B is the gyro scale factor, C is the accelerometer scale factor and D is the rate sensitivity of the accelerometer output. According to these expressions, the rate and acceleration outputs are functions of both the angular rate and the static acceleration. The reason of the change in the acceleration output with the angular rate is the unavoidable phase error in the electronics. These acceleration and rate constants for a specific gyroscope are determined by the static acceleration and angular velocity tests. Then, the effect of the acceleration on the gyroscope output is compensated [31].

In this method, there is no need for the controller design since the circuit is operated in the open loop mode. However, the acceleration sensing electronics is modeled using the real circuit and sensor parameters in MATLAB SIMULINK to analyze the transient behavior of system in response to the applied static acceleration. As being different from the previous simulations and system models, all control loops are implemented together and operated simultaneously to be able to see the effect of the acceleration on the gyroscope operation. Figure 3.22 shows the SIMULINK model of the open loop acceleration sensing electronics with the other control loops.

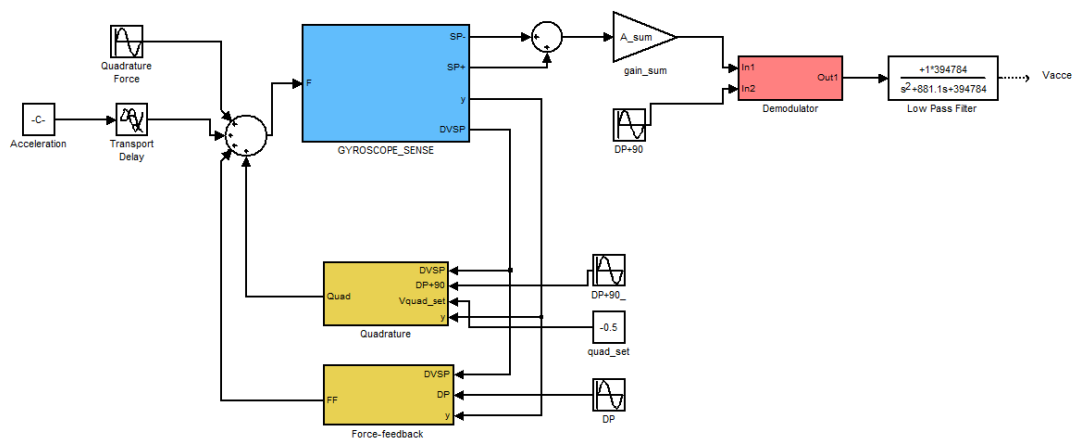


Figure 3.22: SIMULINK model of the open loop acceleration sensing circuit with the force-feedback and quadrature cancellation loops.

Using the SIMULINK model in Figure 3.22, 1g acceleration is applied to the system at 0.5 sec. It should be noted that a sustained quadrature error is provided to the system throughout the simulation by applying an offset voltage to the input of the quadrature cancellation controller. Figure 3.23 shows that the transient behavior of the acceleration output which is picked from the low pass filter output of the acceleration sensing circuit. When 1g acceleration is applied to the system, the acceleration output jumps to 0.48 mV which is a consistent value with Equation 3.17. Figure 3.24 depicts the transient behavior of the sense mode displacement. As seen in Figure 3.24, the static 1g acceleration causes the sense mode displacement axis to shift.

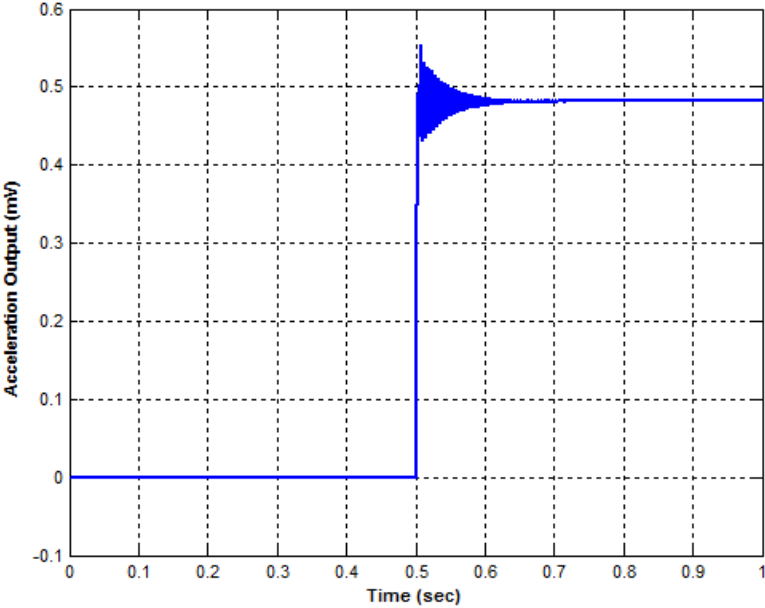


Figure 3.23: Transient behavior of the acceleration output which is picked from the low pass filter output of the acceleration sensing circuit as response to 1 g acceleration using the first acceleration compensation method.

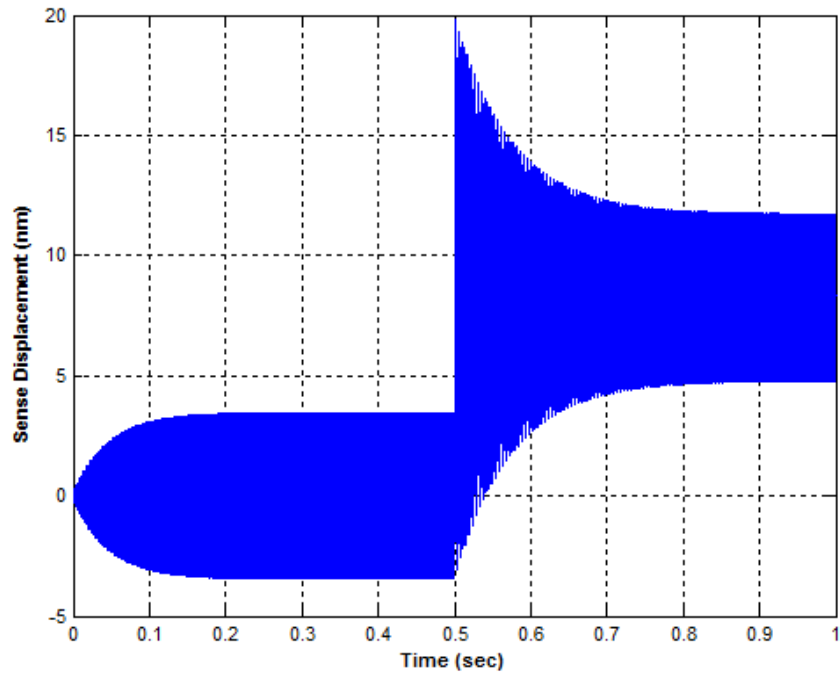


Figure 3.24: Transient behavior of the sense mode displacement which shifts when the 1g acceleration is applied using the first acceleration compensation method.

3.5.2 Closed Loop Acceleration Cancellation Electronics Using Sense Mode Electrodes

This method aims to eliminate the effect of the static acceleration on the gyroscope output in operation by applying differential feedback voltages to the sense mode electrodes using the non-inverting inputs of the preamplifiers. In this method, the acceleration force acting on the sense axis is balanced by generating a DC force on the sense mode electrodes. Figure 3.25 shows the block diagram of the closed loop acceleration cancellation electronics which utilizes the sense mode electrodes for the generation of the acceleration cancellation voltage for the mismatch operation. As opposed to the open loop operation of the acceleration compensation circuit, the output of the low pass filter is fed to the controller. The controller generates a DC voltage applied to the sense mode electrodes via the non-inverting inputs of the sense mode preamplifiers differentially.

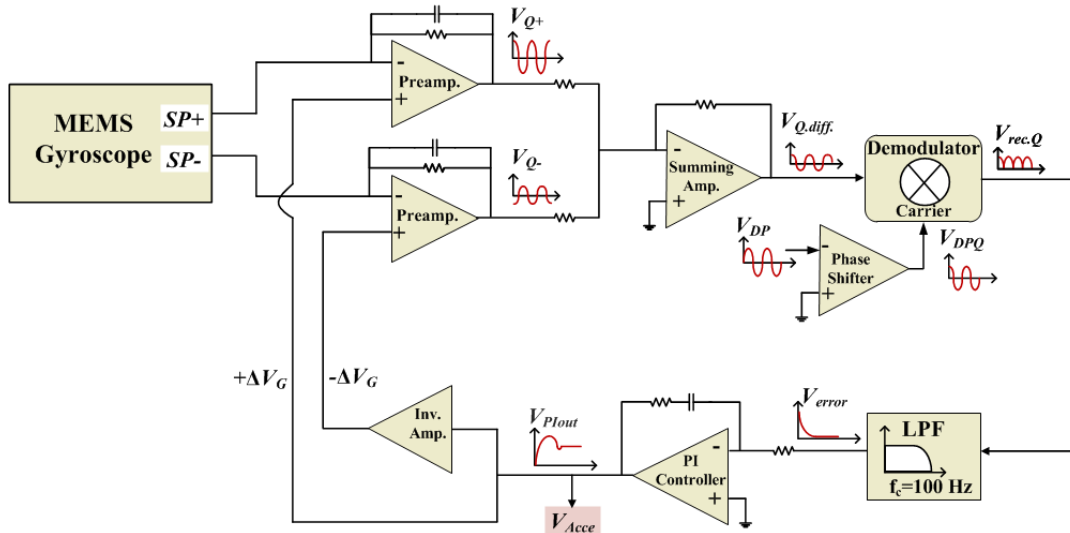


Figure 3.25: Block diagram of the closed loop acceleration cancellation electronics which utilizes the sense mode electrodes for the generation of the acceleration cancellation voltage for the mismatch operation.

Although this method is an improved version of the open loop acceleration compensation method, it still has certain drawbacks. First of all, the effect of the acceleration cannot be completely suppressed during the gyroscope operation because of the working principle of the acceleration sensing electronics. In this thesis study, the acceleration is sensed by comparing the amplitudes of the sustained quadrature signals on the sense mode electrodes as mentioned in Section 3.5.1. However, the amplitude of these signals depends on both the gap spacing and DC voltages of the electrodes. When the feedback voltage is applied to the sense mode electrodes, the position of the sense axis and the potential difference on the sense capacitances change together. Since two agents simultaneously try to make the same error signal zero in this system, the controller settles before the force generated by the sense mode electrodes equals to the acceleration force. Thus, it is mathematically impossible to cancel the effect of the acceleration on the gyroscope output in operation using this method. Moreover, changing the voltage of the non-inverting inputs of the preamplifiers affect the operation of the all other control loops because the operation of the all control circuits starts with the same sense pick signals.

Using a similar approach with the other controller designs, an integral control is implemented instead of the PI controller not to degrade the low pass characteristic of

the system. In the controller design, K_P is set to zero and K_I is optimized as 10 to achieve the system requirements.

The transient behavior of the closed loop acceleration cancellation system proposed in this method is analyzed in MATLAB SIMULINK by modeling the sense system using the second order sensor model with the real sensor and controller values. Similar to the previous compensation method, all control loops are implemented together and operated simultaneously to be able to see the effect of the acceleration on the gyroscope operation. Figure 3.26 shows the SIMULINK model of the open loop acceleration sensing electronics with the other control loops.

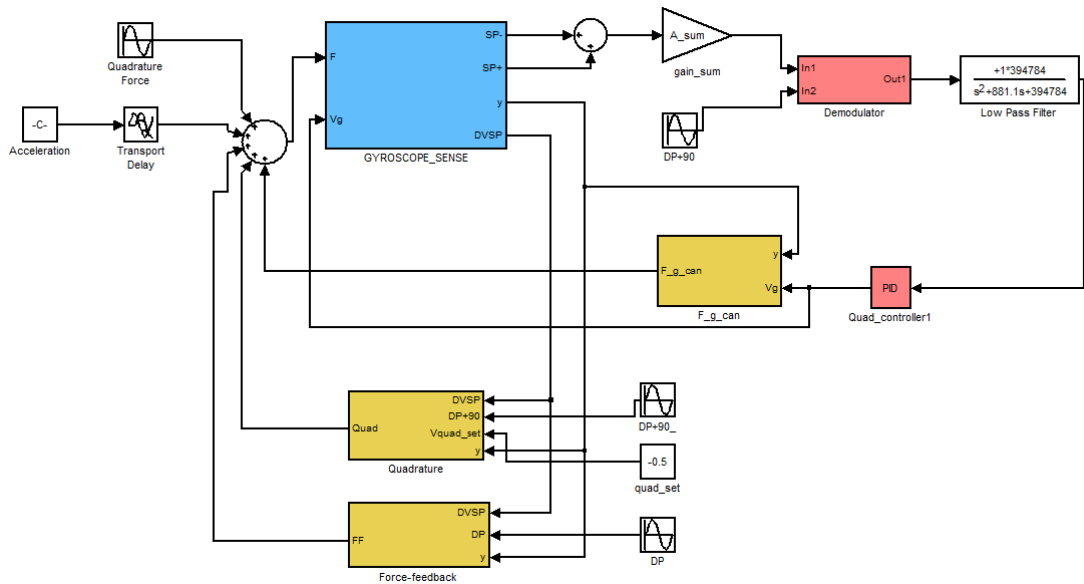


Figure 3.26: SIMULINK model of closed loop acceleration compensation circuit which utilizes the sense mode electrodes for the generation of the acceleration cancellation voltage.

Using the SIMULINK model in Figure 3.26, 1g acceleration is applied to the system at 0.5 sec. Similar to the previous case, a sustained quadrature error is provided to the system throughout the simulation by applying an offset voltage to the input of the quadrature cancellation controller. Figure 3.27 shows that the transient behavior of the acceleration output which is picked from acceleration controller output. When 1g acceleration is applied to the system, the acceleration output jumps to 12 mV which

is a consistent with experimental value. Figure 3.28 shows the transient behavior of the sense mode displacement. Although the closed loop acceleration controller tries to pull the sense axis back in this method, it cannot eliminate the effect of the acceleration due to the reasons mentioned above.

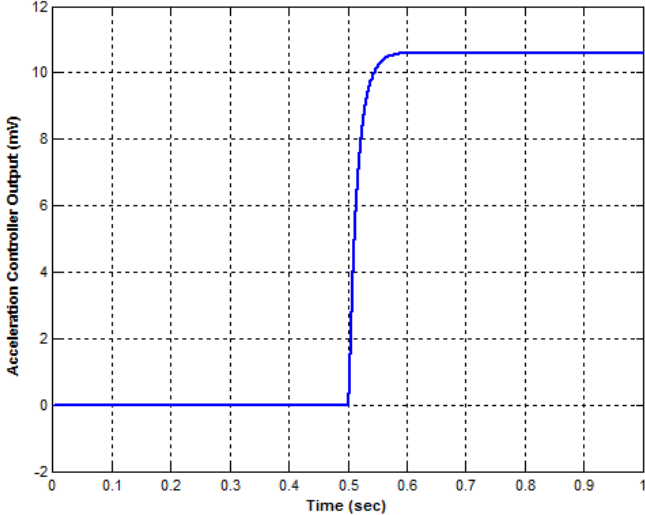


Figure 3.27: Transient behavior of the acceleration controller output as response to 1 g acceleration using the second acceleration compensation method.

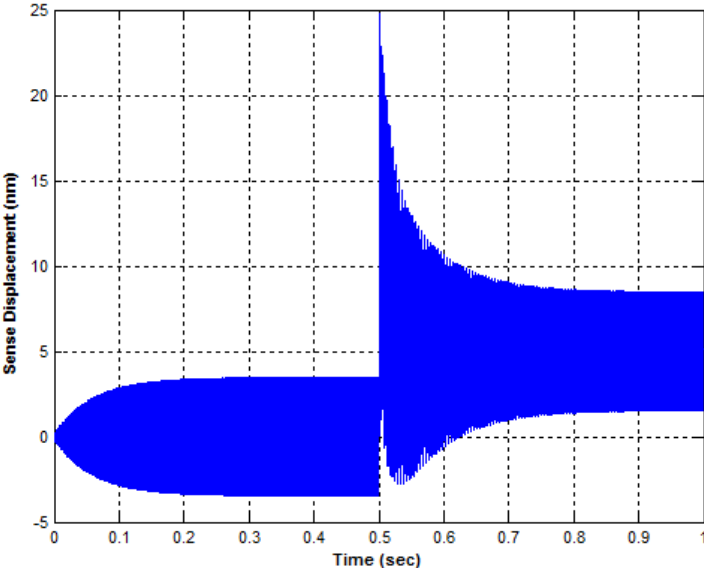


Figure 3.28: Transient behavior of the sense mode displacement as response to 1 g acceleration using the second acceleration compensation method.

3.5.3 Closed Loop Acceleration Cancellation Electronics Using Acceleration Cancellation Electrodes

In this method, the effect of the acceleration on the gyroscope output is suppressed by counterbalancing the acceleration force with the aid of the acceleration cancellation electrodes. Figure 3.29 shows the block diagram of the closed loop acceleration cancellation electronics which employs the dedicated electrodes for the generation of the acceleration cancellation voltage for the mismatch operation. In this method, the feedback voltage is applied to the dedicated electrodes instead of the sense mode electrodes to overcome the problems mentioned in the previous method. The utilization of the additional acceleration cancellation electrodes isolates the operation of the acceleration cancellation circuit from the other control loops. The related equations with this method are given in Section 2.6.4 in details.

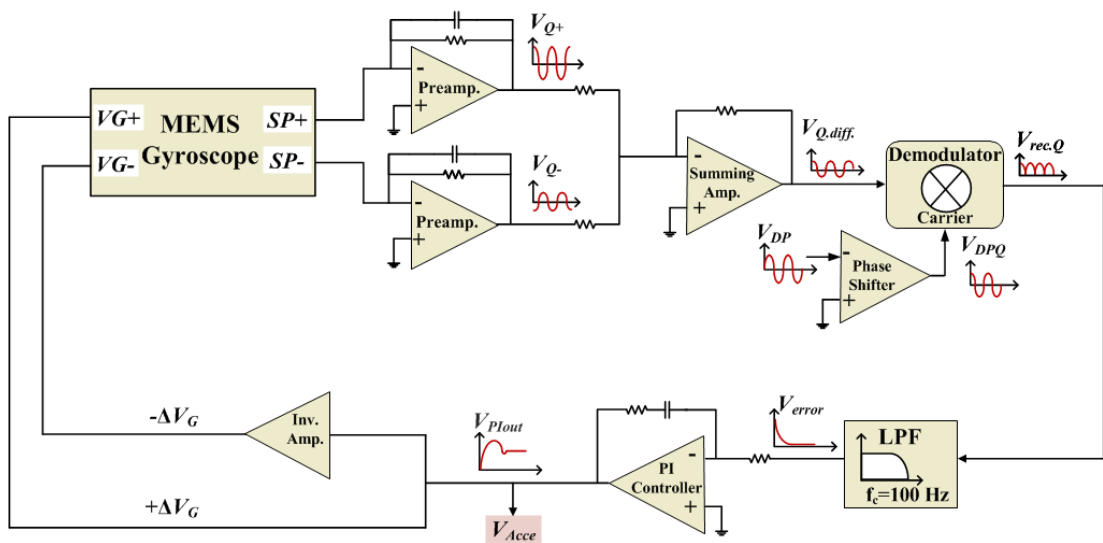


Figure 3.29: Block diagram of the closed loop acceleration cancellation electronics which employs the dedicated electrodes for the generation of the acceleration cancellation voltage for the mismatch operation.

In the controller design, an integral control is implemented instead of the PI controller not to degrade the low pass characteristic of the system, using a similar approach with previous controller designs. For this method, K_P is set to zero and K_I is

optimized as 300 to achieve the sufficient phase margin, minimum settling time and minimum overshoot for the operation.

The transient behavior of the closed loop acceleration cancellation system proposed in this method is analyzed in MATLAB SIMULINK by modeling the sense system using the second order sensor model with the real sensor and controller values. Similar to the previous compensation methods, all control loops are implemented together and operated simultaneously to be able to see the effect of the acceleration on the gyroscope operation. Figure 3.30 shows the SIMULINK model of the open loop acceleration sensing electronics with the other control loops.

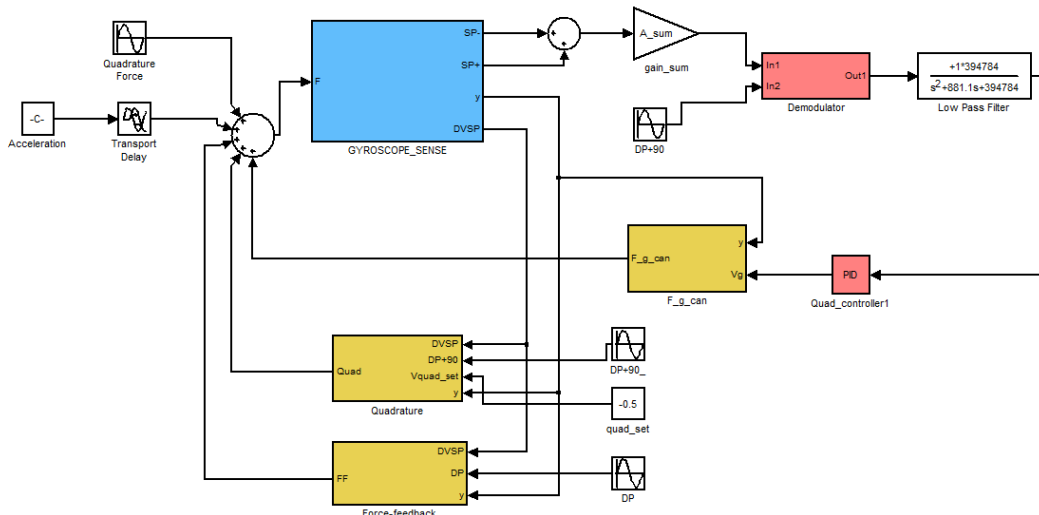


Figure 3.30: SIMULINK model of closed loop acceleration compensation circuit which employs the dedicated electrodes for the generation of the acceleration cancellation voltage.

Using the SIMULINK model in Figure 3.30, 1g acceleration is applied to the system at 0.5 sec. Similar to the previous case, a sustained quadrature error is provided to the system throughout the simulation by applying an offset voltage to the input of the quadrature cancellation controller. Figure 3.31 shows that the transient behavior of the acceleration output which is picked from acceleration controller output. When 1g acceleration is applied to the system, the acceleration output jumps to 240mV which

is a consistent value with Equation 2.25. Figure 3.32 depicts the transient behavior of the sense mode displacement. In this method, the closed loop acceleration controller completely eliminates the effect of the acceleration on the sense mode displacement.

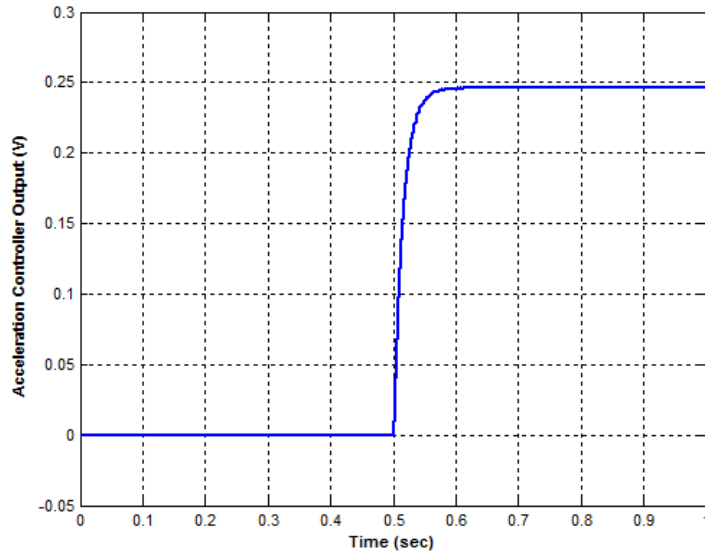


Figure 3.31: Transient behavior of the acceleration controller output as response to 1 g acceleration using the third acceleration compensation method.

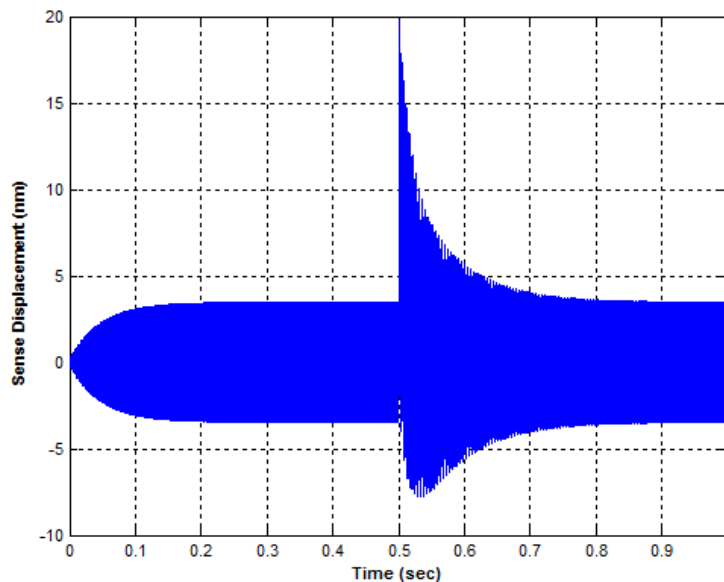


Figure 3.32: Transient behavior of the sense mode displacement for acceleration compensation method. In this method, the closed loop controller completely eliminates the effect of the static acceleration on the sense mode displacement.

CHAPTER 4

FABRICATION OF MEMS GYROSCOPES

The gyroscopes used in this study are fabricated through modified SOG (silicon-on-glass) micromachining process and wafer-level hermetically encapsulated using SOI cap wafers with vertical feedthroughs. SOG process is an attractive way of fabricating MEMS sensors by anodically bonding of a silicon wafer to a glass wafer. In the modified SOG process proposed in [32], first, the recesses and electrical interconnects are formed on the glass wafers. Then, the formation of the device layer is performed on the SOI wafer using deep reactive ion etching (DRIE). Finally, glass wafer and SOI wafer are combined through the anodic bonding. The modified SOG process has some certain advantages. Firstly, constructing device layer on an insulating layer significantly decreases the parasitic capacitances. Moreover, electrical interconnects can easily formed over glass substrates. Furthermore, the use of SOI wafer provides uniform etch profile on the structure, higher production yield, and lower proof mass voltage needed for the gyroscope operation.

SOI cap wafers are used for the wafer level vacuum packaging of the fabricated sensor wafers. In the cap wafer process, first, via openings are formed on the handle layer of SOI cap wafer. Then, vertical feedthroughs and sealing walls are simultaneously constructed on the device layer of the wafer. Sealing of the sensor wafer with the SOI cap wafer is achieved either through the anodic bonding process or the eutectic bonding process. The process steps for both bonding processes are same but the sequence of the steps is different. The main advantage of using vertical feedthroughs in these encapsulation processes is that it does not require any complex via-refill or trench- refill processes [33].

This chapter continues as follows, Section 4.1 provides the detailed information about the modified SOG process used for the sensor wafer fabrication. Section 4.2 describes the wafer level hermetic encapsulation processes for both anodic bonding version and eutectic bonding version. Section 4.3 presents the fabrication results. Finally, Section 4.4 summarizes this chapter.

4.1 Fabrication of Sensor Wafer Using Modified SOG (M-SOG) Process

The modified SOG process starts with an empty glass wafer to form anchors and metallic interconnects. The first step is the anchor formation. The anchors are the bonding regions on the glass wafer where will be connected to the device layer of the SOI wafer during the anodic bonding. Chromium/Gold (Cr/Au) is used as masking material instead of photoresist (PR) during the anchor formation process in the hydrofluoric acid (HF) since the etch rate of HF to PR is very high. The anchor formation begins with metal deposition. Cr/Au is deposited on the glass wafer through the thermal evaporation process. Cr/Au is used instead of only Au because Cr layer functions as adhesion layer between the glass wafer and Au layer. Next, Cr/Au layer is patterned using wet etchants. Then, glass is etched in the pure HF solution to construct the anchor structures. The etch rate of HF for the glass is highly depend on the ambient temperature so etching process should be conducted by measuring the depth of the anchors in a controlled manner. After the glass etch is completed, Cr/Au is stripped in the wet etchants.

The second step of the glass wafer process is the formation of the electrical interconnects. Cr/Au is deposited by the thermal evaporation. Then, Cr/Au is patterned to form the pad metallization using wet chemical etchants. Finally, glass wafer is cleaned in the piranha solution composing of $\text{H}_2\text{SO}_4:\text{H}_2\text{O}_2$ with ratio of 1:1 before the anodic bonding. This is the last step of the glass wafer process.

SOI wafer process also includes two main steps: shallow etch and structure formation. The first step is the shallow edge process on the device layer of SOI wafer. The purpose of this step is to prevent the sealing bonding region on the glass wafer from attaching to the SOI wafer during first anodic bonding. The PR is also removed by using the oxygen plasma in the DRIE. After the DRIE process, the

piranha cleaning is performed for the SOI wafer. The second process step of the SOI wafer is the formation of sensor structure on the device layer using the DRIE. DRIE provides anisotropic etching; thus, it is the best way for the formation of the device structure having critical dimension. The PR is again removed by using the oxygen plasma in the DRIE. After the DRIE process, the piranha cleaning is performed for the SOI wafer to completely clean the polymer residuals on the wafer.

After the glass and SOI wafers are prepared, these wafers are bonded using the anodic bonding technique presented in [45]. Before the anodic bonding process, the native oxide layer on the silicon substrate should be removed for a good quality of bonding. After the anodic bonding, the handle layer of the SOI wafer is removed by the DRIE process. Finally, the device layer bonded to the glass wafer is released by removing the buried oxide layer in the BHF solution. This is the last step of the sensor wafer fabrication process. Figure 4.1- Figure 4.8 show the fabrication steps of the sensor wafer based on the modified SOG process.

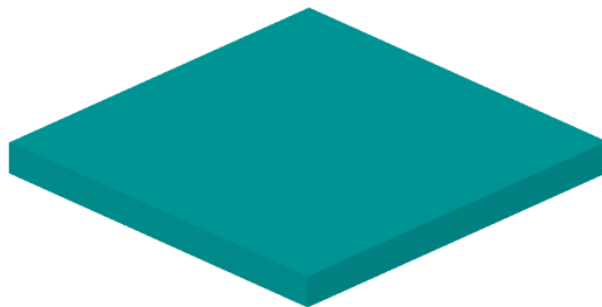


Figure 4.1: Empty glass wafer

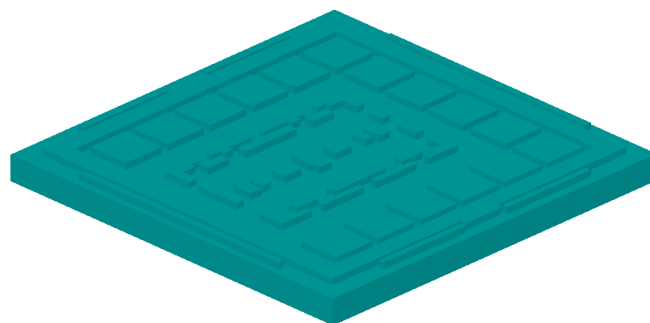


Figure 4.2: Anchor formation

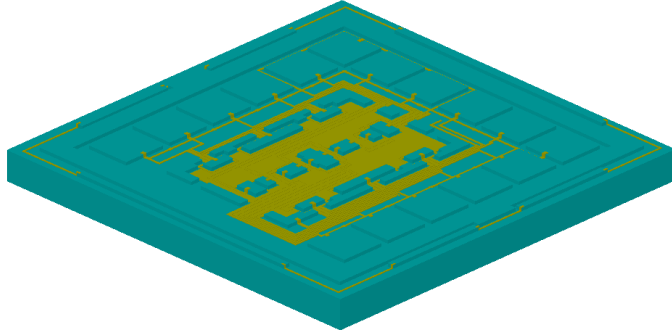


Figure 4.3: Formation of the electrical interconnects

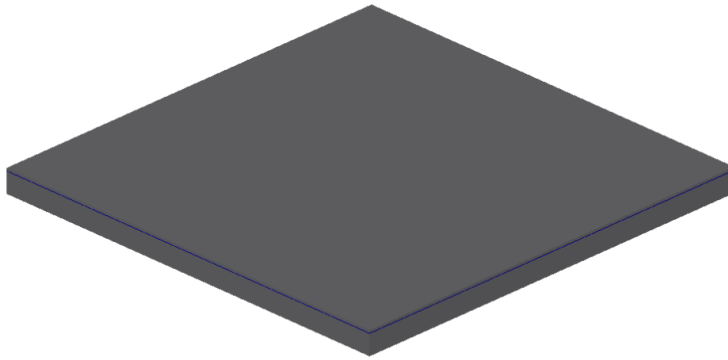


Figure 4.4: Empty SOI wafer

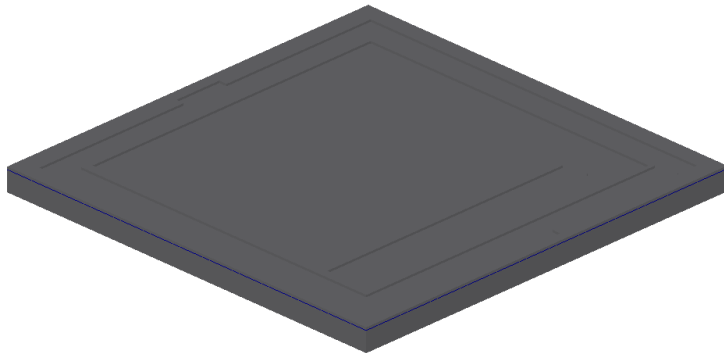


Figure 4.5: Shallow etch on the device layer

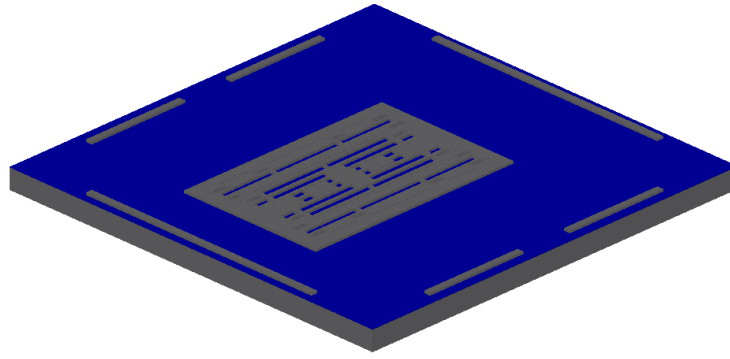


Figure 4.6: Formation of the sensor structure

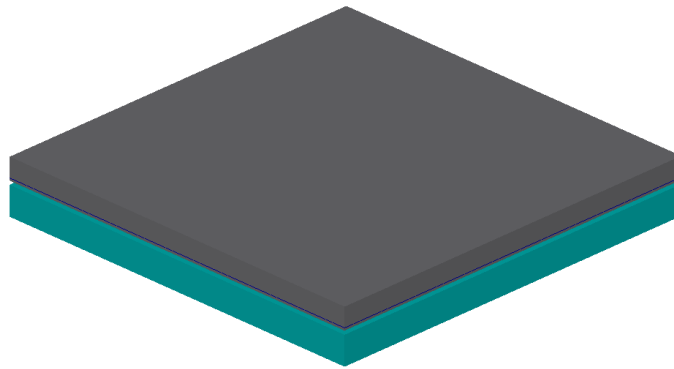


Figure 4.7: Anodic bonding of glass and SOI wafers

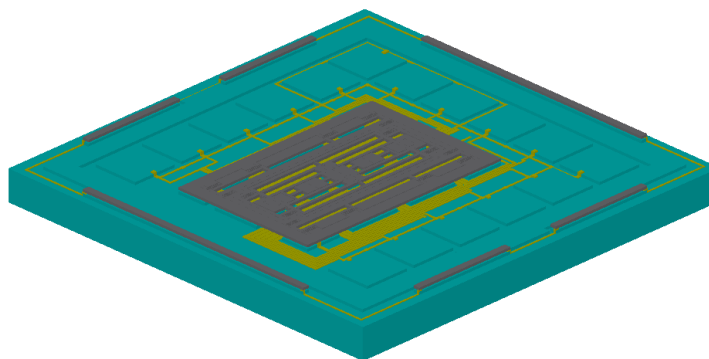


Figure 4.8: Release of the device structure after anodic bonding

4.2 Wafer Level Hermetic Encapsulation of MEMS Gyroscopes using SOI Cap Wafers with Vertical Feedthroughs

Hermetic encapsulation of the sensor wafer is achieved using an SOI cap wafer, and the electrical contacts on the sensor wafers are transferred to the outside world via the vertical feedthroughs. SOI cap wafer is composed of highly doped device and handle layers, and both sides of the wafer is deposited with the thermal oxide layer. Fabrication process of the SOI cap wafer for the packaging is comprised of four process masks. The process details of the SOI cap wafer process can be found in [33], [46] and [47].

After completing the fabrication of the sensor wafer and SOI cap wafer, these wafers are bonded for the vacuum packaging of the sensor wafer. The hermetic sealing of the sensor wafer can be achieved using two different bonding methods: anodic bonding technique or Au-Si eutectic bonding technique. The detailed information about the wafer level hermetic encapsulation process using the anodic and Au-Si eutectic bonding methods can be found in [33], [46] and [47]. Figure 4.9 - Figure 4.15 show the fabrication steps of SOI cap wafer and packaging process.

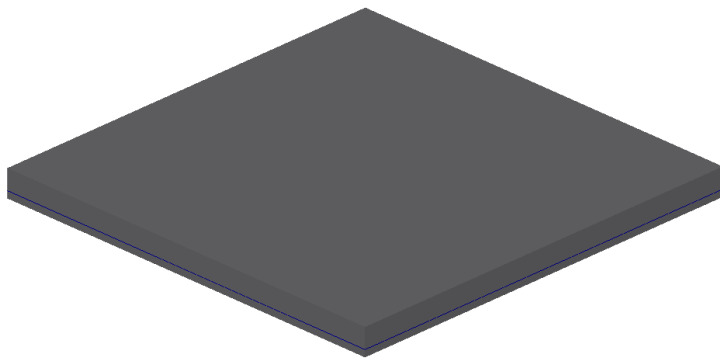


Figure 4.9: Empty SOI cap wafer

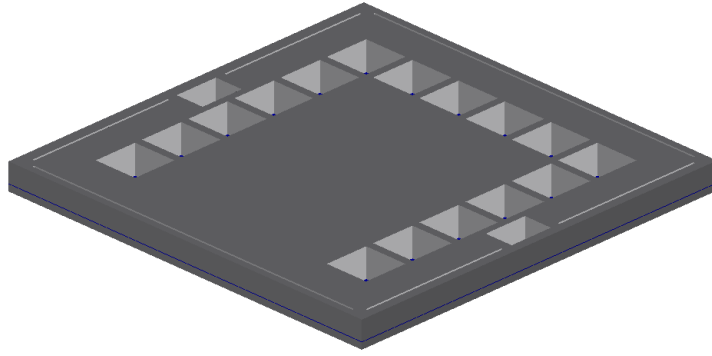


Figure 4.10: Formation of the via openings on the handle layer

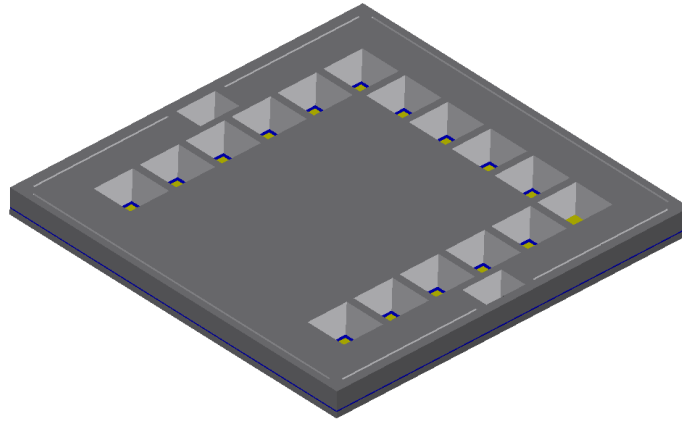


Figure 4.11: Formation of the wire bonding pads

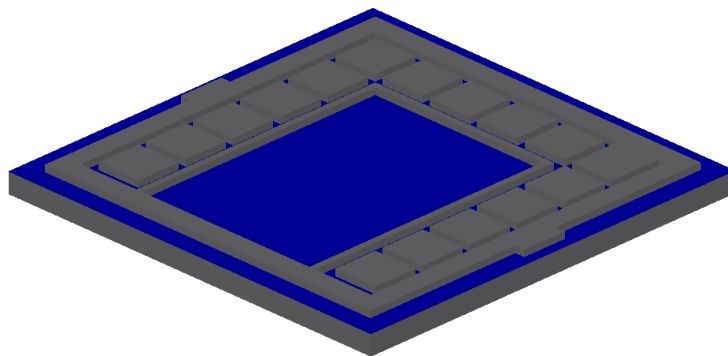


Figure 4.12: Formation of the vertical feedthroughs and sealing walls on the device layer

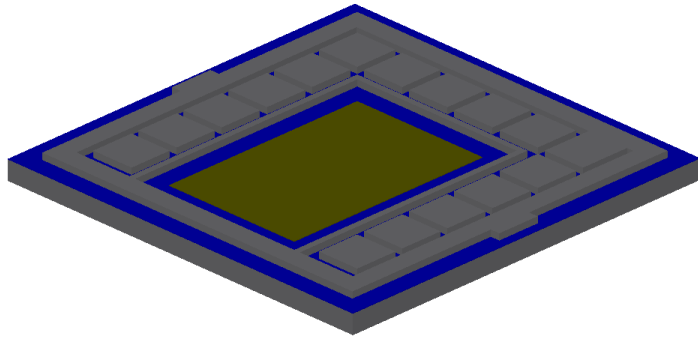


Figure 4.13: Getter deposition

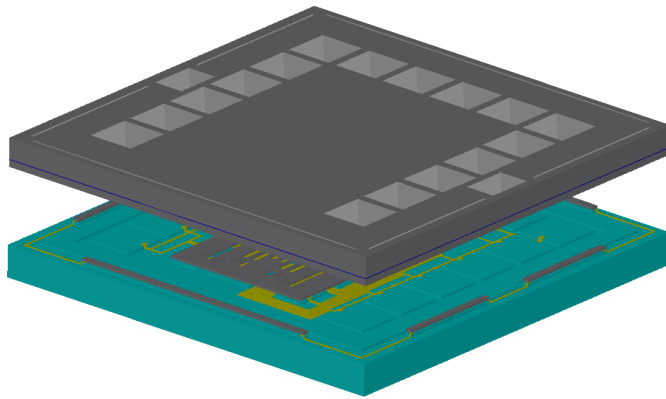


Figure 4.14: Anodic/Eutectic bonding of cap wafer and sensor wafer for packaging

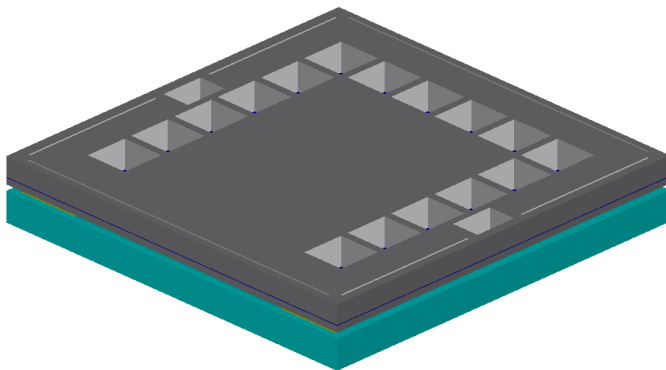


Figure 4.15: Final view of the wafer level vacuum packaged sensor wafer

4.3 Fabrication Results

Despite the optimization of the process steps during the fabrication of the vacuum packaged sensor wafer, the fabrication imperfections are unavoidable in the process. The most important fabrication imperfection is the loss in the critical sensor dimension. The lithography tolerances and the undercut during the DRIE process of the structure mask cause a thinning in the widths of the springs and fingers. The change in the spring dimensions causes a change in the mechanical resonance frequencies of the gyroscope. Figure 4.16 depicts the SEM pictures of the double-folded and half-folded springs used in the drive mode, and the clamped-guided-end spring used in the sense mode after the fabrication of the sensor wafer.

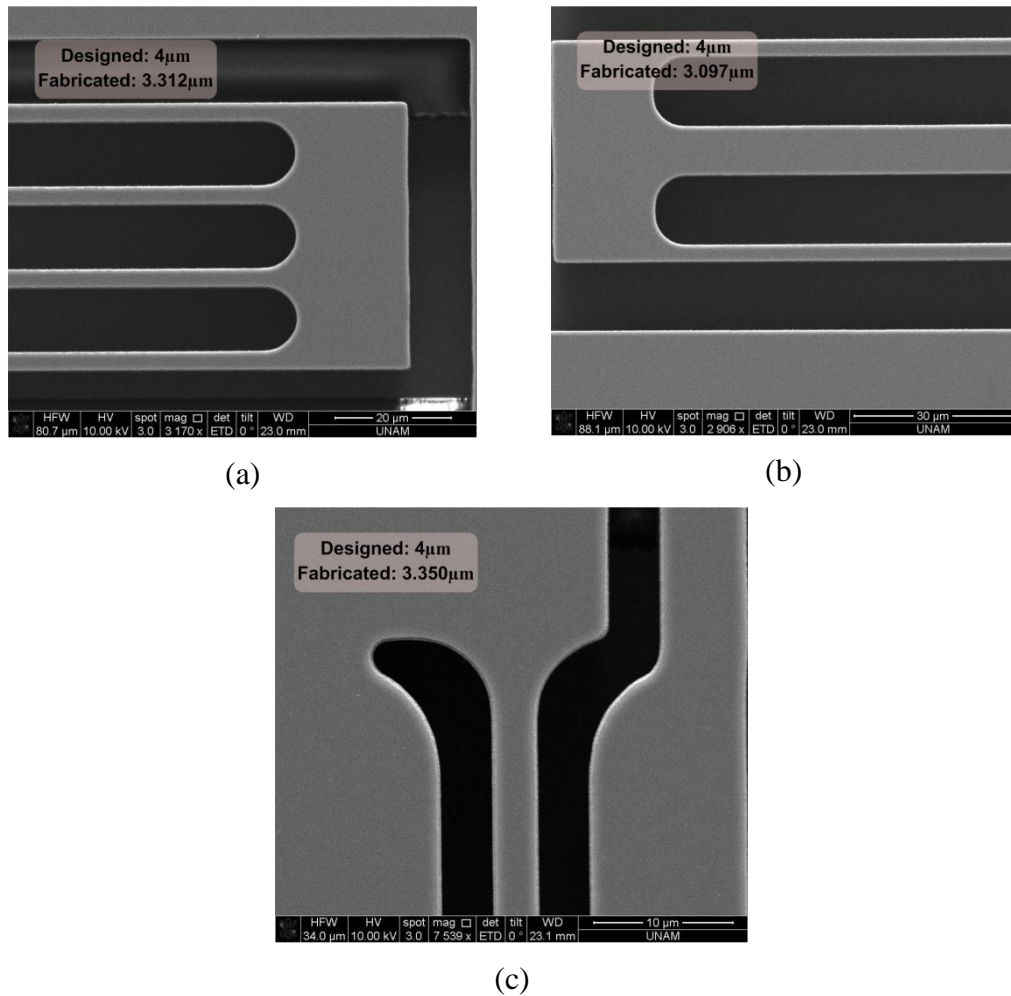


Figure 4.16: SEM pictures of (a) double-folded, (b) half-folded, and (c) clamped guided springs after the fabrication.

After the fabrication, the width of the drive and sense mode springs are measured to be much narrower than the designed value as seen in Figure 4.16. But, the thinning of the springs is estimated during the design stage of the gyroscope so the mechanical resonance frequencies of the drive and sense modes are determined considering the fabrication imperfections before the fabrication. Thus, the change in the spring widths does not significantly affect the operation of the gyroscope.

Similarly, the gap spacing of the fingers gets wider after the fabrication. Particularly, the change in the dimensions of the sense, quadrature and acceleration cancellation electrodes affects the capabilities of the corresponding control loops. Figure 4.17 depicts the SEM pictures of the sense, quadrature and acceleration cancellation electrodes after the fabrication.

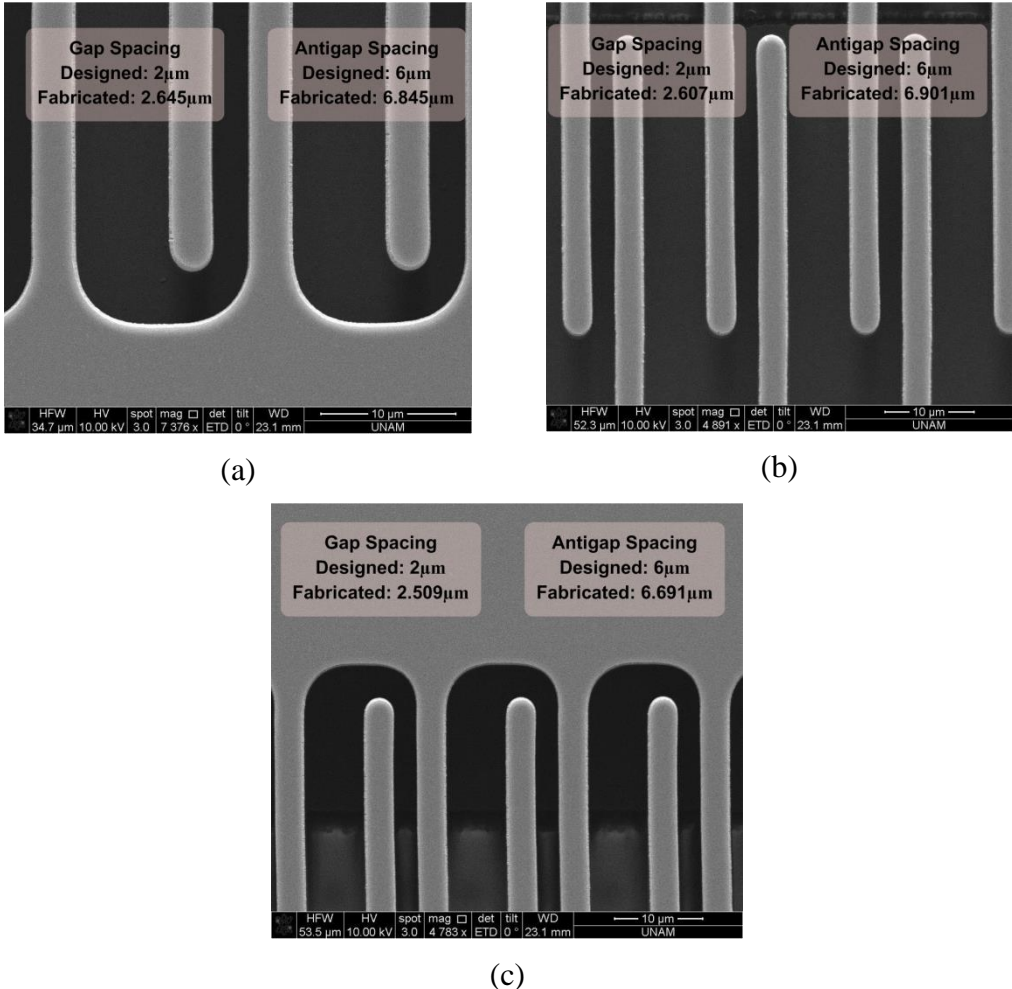


Figure 4.17: SEM pictures of (a) sense, (b) quadrature, and (c) acceleration cancellation electrodes after the fabrication.

Figure 4.18 shows the SEM picture of the fabricated single-mass fully-decoupled gyroscope including the acceleration cancellation electrodes which are used to generate force to balance the acceleration force. In this study, the frequency tuning electrodes are also included in the gyroscope structure to adjust the resonance frequency of sense mode considering the mode-matched operation; however, the gyroscope is operated in the mismatch condition during the system level tests.

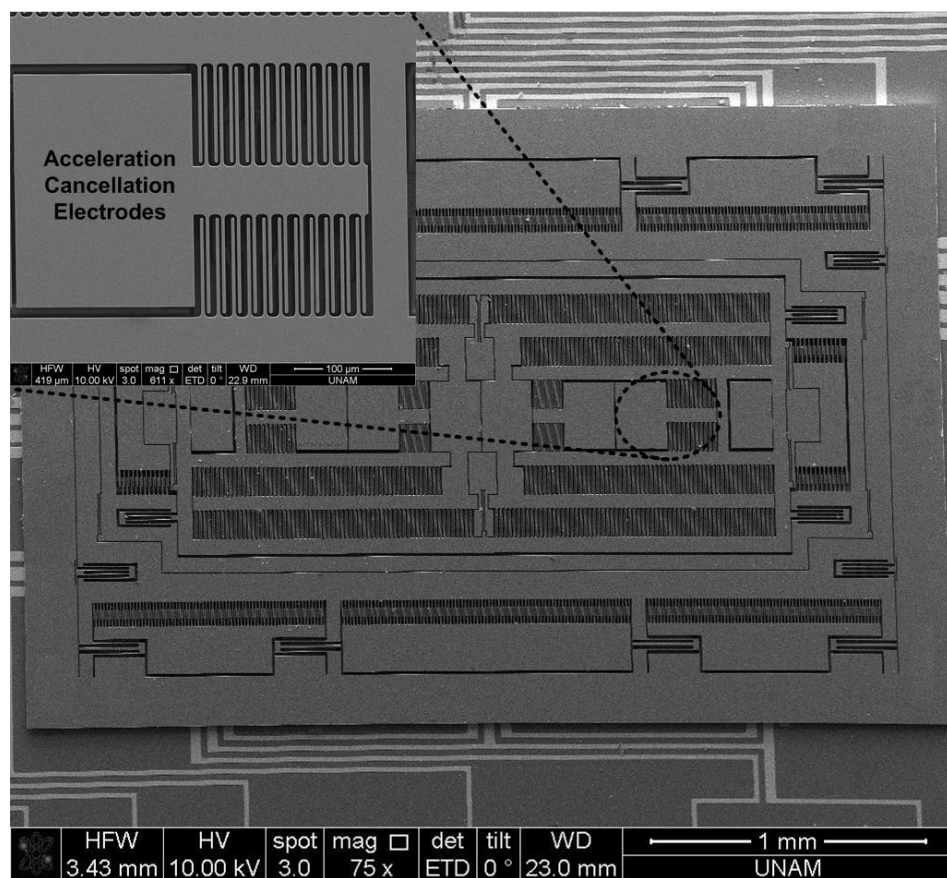


Figure 4.18: SEM picture of the fabricated single-mass fully-decoupled gyroscope including the acceleration cancellation electrodes.

After the packaging process of the sensor wafer using the SOI cap wafer, one of gyroscope die is diced to see the cross sectional view of the fabricated gyroscope. Figure 4.19 shows the SEM picture of the vacuum packaged MEMS gyroscope, providing the details of via openings and vertical feedthroughs.

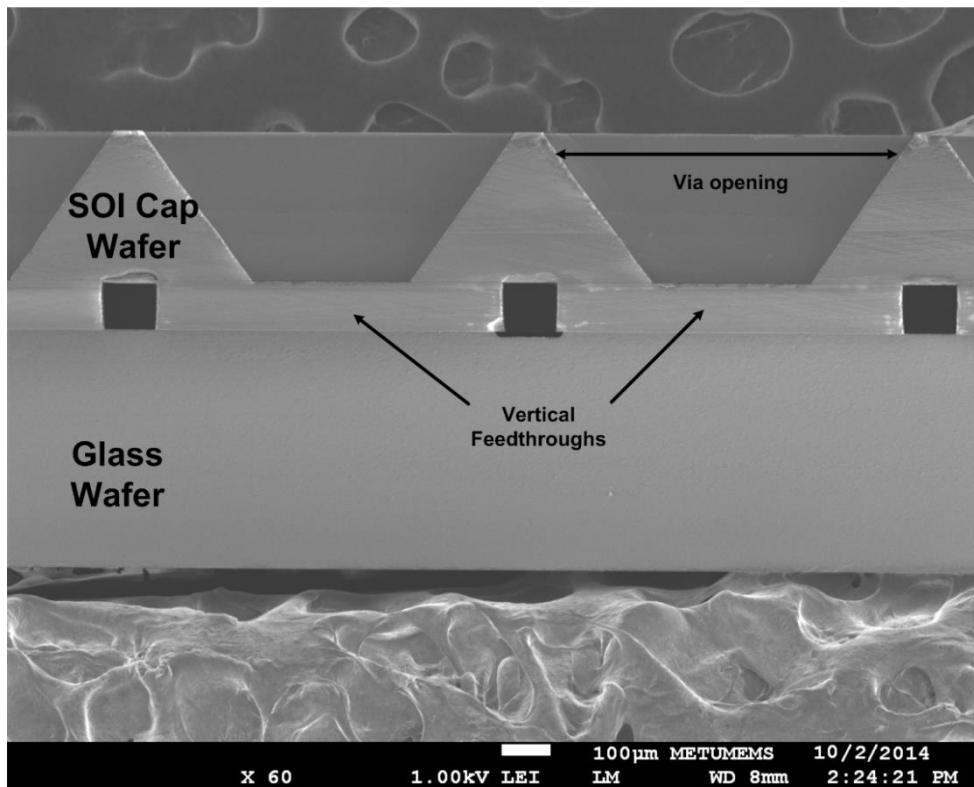


Figure 4.19: SEM picture of the cross sectional view of the packaged sensor.

4.4 Summary

This chapter first describes the fabrication steps of the sensor wafer based on the modified SOG process. Then, the wafer level vacuum packaging processes of the sensor wafer are presented with the detailed process steps for anodic and Au-Si eutectic bonding methods. Finally, the fabrication results are discussed.

CHAPTER 5

TEST RESULTS

This chapter provides the test results of the studied gyroscope. Section 5.1 presents the resonance characterization procedure for the MEMS gyroscopes. Section 5.2 demonstrates the test setup for system level tests of the studied gyroscopes. Section 5.3 gives the test data about the static acceleration tests. Section 5.4 presents test results for the centrifugal acceleration tests. Section 5.5 provides the performance test results of the studied gyroscopes. Finally, Section 5.6 summarizes this chapter.

5.1 Characterization and Test Procedure of Gyroscopes

After the MEMS gyroscopes are fabricated, the resonance tests are conducted by randomly choosing the sensors from the different places of the wafer. If the drive and sense modes of the gyroscopes are functional, the wafer is diced. The die level gyroscopes are tested separately in the probe station. Figure 5.1 shows the test set-up for the die level resonance tests. As seen in Figure 5.1, the electrical connection of the sensor to the outside world is provided by using special probes in the probe station. Then, the sensor is driven from the dynamic signal analyzer (DSA) which gives an AC signal with a varying frequency around the resonance frequency of the gyroscope. The output of the gyroscope is a current signal in response to the actuation signal, and the output current is converted to the voltage by a preamplifier op-amp. The output voltage is fed to the DSA, and the resonance characteristics of the gyroscope are extracted by looking at the input-output ratio in the frequency domain. These tests are conducted for both the drive and sense mode of the gyroscope separately to obtain the sensor parameters such as the gain, resonance frequency and quality factor. After the die level resonance tests, the gyroscopes having the desired resonance characteristics are chosen to be used.

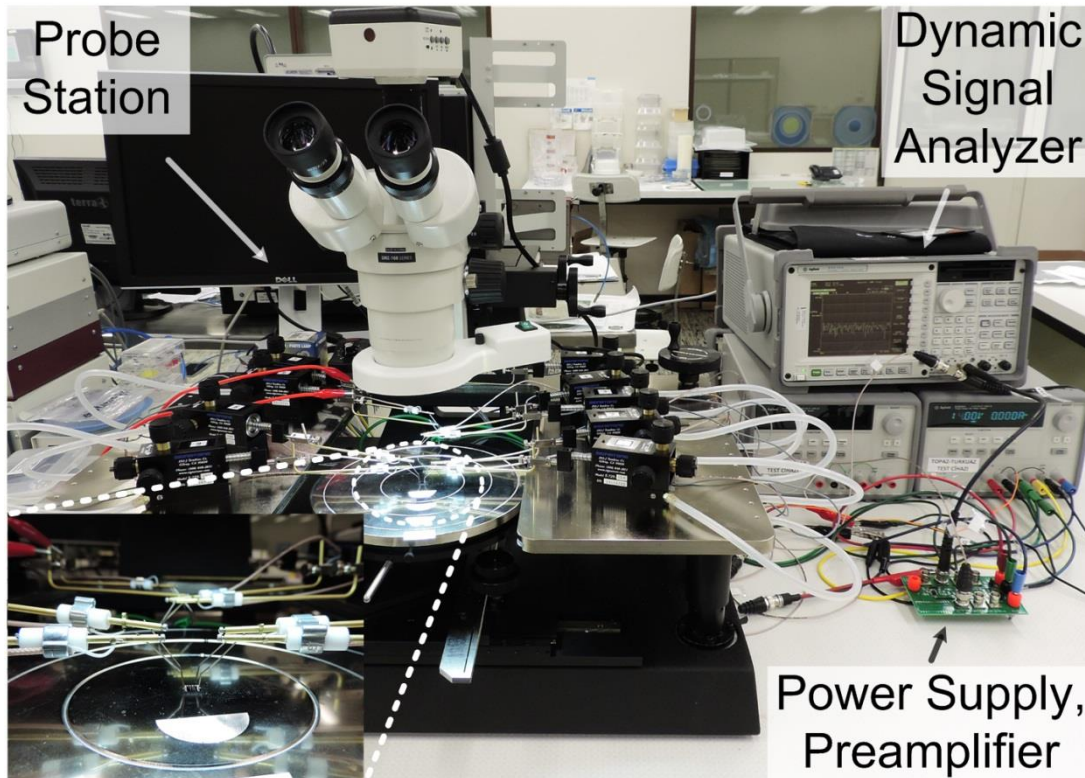


Figure 5.1: Resonance test set-up for the die level gyroscope test.

After the die level resonance test, the gyroscope is connected with the front-end electronics on a special hybrid glass substrate. Figure 5.2 depicts a gyroscope integrated with the front-end electronics inside a hybrid package. The front-end electronics includes the drive and sense mode preamplifier stages, and instrumentation amplifier. Since the output current of the gyroscope is very small, the gyroscope and preamplifier stages should be in the same hybrid package to avoid from the parasitic effects and noise. Before connecting the gyroscope to the package, the functionality test of the front-end electronics is done to ensure that the circuit works properly. If the gyroscope is fabricated using the wafer level vacuum packaging process as mentioned in Chapter 4, there is no need for the vacuum packaging of the hybrid package. However, if the gyroscope is not vacuum packaged during the process, then, the package is vacuumed with the front-end electronics and gyroscope using a technique called projection welding. In this thesis work, the gyroscopes used in the first and second phases of the study are vacuum packaged

using the projection welder, and the gyroscopes used in the third phase of the study are fabricated using the wafer-level vacuum packaging process.

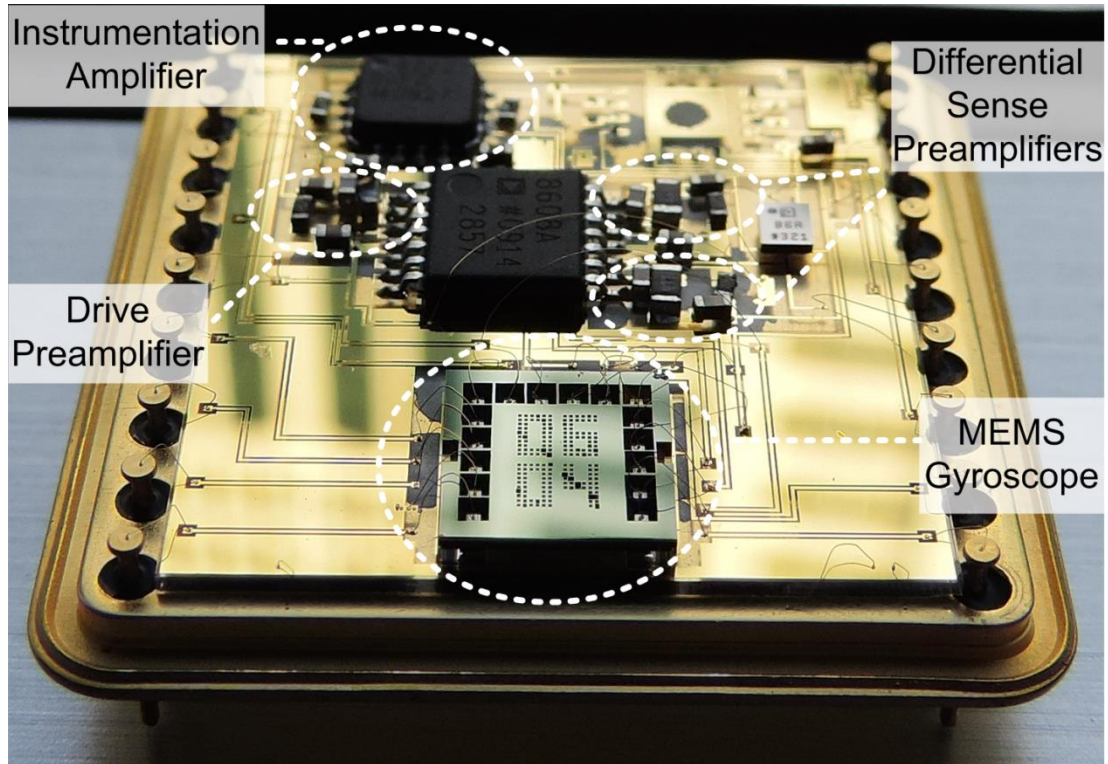


Figure 5.2: Gyroscope integrated with the front-end electronics on the hybrid glass substrate.

After the vacuum packaging of the gyroscopes is completed, the resonance tests are repeated with the front-end electronics to extract the sensor parameters such as the resonance frequency, gain and quality factors. These parameters are needed during the design of the control electronics. Table 5.1 and Table 5.2 represents the drive and sense mode resonance characteristics of the vacuum packaged gyroscopes with the front-end electronics studied in this theses, respectively. The resonance test results indicate that the vacuum condition of the gyroscopes fabricated with wafer level vacuum packaging process is much better compared to the gyroscopes packaged with the projection welding method.

Table 5.1: Drive mode resonance characteristics of the vacuum packaged gyroscopes studied in this thesis.

Gyro ID	Proof Mass (V)	Res. Freq. (Hz)	Res. Gain (dB)	Quality Factor	Packaging Type
E02	10	12209	3.3	25200	Projection Welding
H02	10	12495	1.5	19320	Projection Welding
0803	14	10747	16.0	51100	Wafer Level-Anodic
1207	14	10813	16.3	48000	Wafer Level-Eutectic

Table 5.2: Sense mode resonance characteristics of the vacuum packaged gyroscopes studied in this thesis.

Gyro ID	Proof Mass (V)	Res. Freq. (Hz)	Res. Gain (dB)	Quality Factor	Packaging Type
E02	10	12473	25.7	1480	Projection Welding
H02	10	12809	24.3	1120	Projection Welding
0803	14	10735	40.5	3070	Wafer Level-Anodic
1207	14	10594	38.8	3100	Wafer Level-Eutectic

5.2 System Level Test Setup for the Acceleration and Performance Tests of the Studied MEMS Gyroscopes

After the characterization of the gyroscope mounted in a hybrid package, the sensor module is connected with the drive, sense, quadrature cancellation and acceleration cancellation modules on a test PCB to perform the system level tests. Figure 5.3 shows the test setup for the system level tests of the studied gyroscopes. Since the main objective of this thesis study is to suppress the static acceleration sensitivity of MEMS gyroscopes, special test setups are prepared for the acceleration tests. Two basic acceleration tests performed in this study are the static acceleration test on the rotation table and centrifugal acceleration test on the rate table.



Figure 5.3: Test setup for the system level tests.

5.3 Test Results of the Studied MEMS Gyroscopes for Static Acceleration Tests

The static acceleration test is performed by rotating the gyroscope about its out-of-plane axis to determine its effect on the rate output of the gyroscope. Figure 5.4 depicts the static acceleration test setup used in this study. During the test, the rate and acceleration data are collected with a step angle of 30° under the gravitational ($1g$) acceleration condition. The g -acceleration (a) acting on the gyro sense-axis can be directly computed by $a=g*\sin\theta$, where θ is the rotation angle. During the test, the gyroscope is exposed to the static acceleration varying from $-1g$ to $1g$. The purpose of the static acceleration test is to see the effect of the static acceleration on the bias

of the gyroscope output and to determine the efficiency of acceleration cancellation methods explained in Section 3.5 for suppressing this effect.

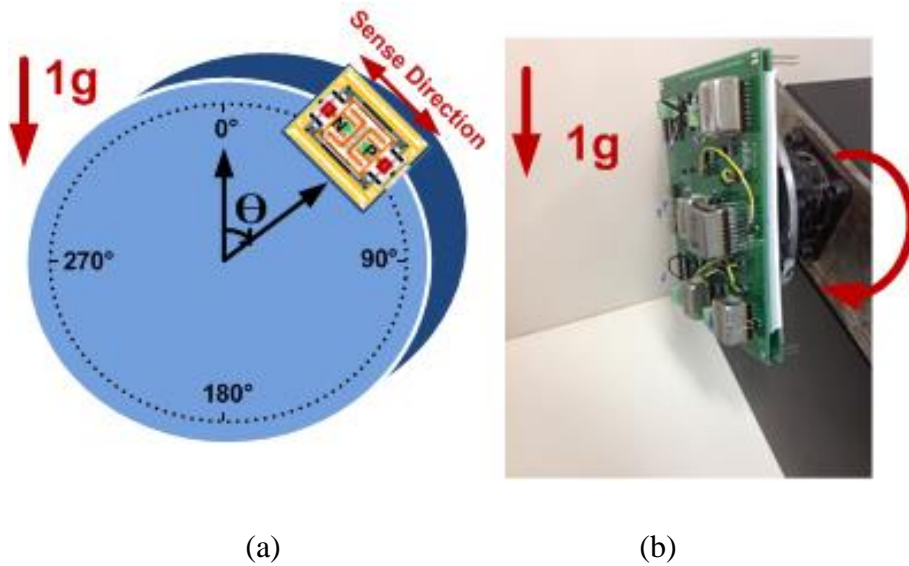


Figure 5.4: (a) Schematic and (b) actual views of test setup for the static acceleration tests on the rotation table.

In the first phase of this study, the acceleration cancellation circuit is operated in open loop mode using the gyroscope (E02) in the mismatched condition, as mentioned in 3.5.1 (Method-1). It should be noted that the mismatch operation is particularly preferred in thesis study to ensure that there is no additional phase error exists between the drive and sense signals due to the mode of operation. During the static acceleration test, the gyroscope is rotated with a step angle of 30° under the gravitational (1g) acceleration condition as shown in Figure 5.4; as a result, the sense axis of the gyroscope is subjected to the static acceleration varying from -1g to 1g as a function of the rotation angle. For the proper operation of the acceleration sensing circuit, there should exist a certain level residual quadrature signal in the sense mode of the gyroscope. Otherwise, the resultant signal obtained by summing the out of phase sense mode output signals cannot be distinguished from the noise. For this reason, the set point of the quadrature cancellation controller is set to 500mV. In this method, the rate output data and acceleration output data which is the output of the acceleration sensing circuit are simultaneously collected during the test. The data are

collected for at least 10 seconds at each angle step. Then, the collected data are processed to determine the average values of the rate output and acceleration output for each rotation angle. After finding a linear relation between the rate output and acceleration output according to the static acceleration test data, the rate output is corrected in the software to compensate the effect of the static acceleration.

Figure 5.5 shows the measured rate output (blue one), compensated rate output (blue-dashed one) and acceleration output (red one) as a function of the rotation angle for the gyroscope (E02). In this test, the g-sensitivity of the gyroscope (E02) is measured to be $2120^{\circ}/\text{hr}/\text{g}$ before the acceleration compensation. Moreover, the acceleration output linearly changes with the applied acceleration, and its scale factor is measured to be $0.53\text{mV}/\text{g}$, which is consistent with the value estimated from the theoretical expression shown in Equation 3.17. Assuming both the rate output and acceleration output linearly changes with the static acceleration, the necessary constants in Equation 3.18 are determined using the static acceleration test data. Then, the measured rate output is corrected to eliminate the effect of the acceleration in the software. The g-sensitivity of the gyroscope (E02) is calculated to be $192^{\circ}/\text{hr}/\text{g}$ after the acceleration compensation. That is, the effect of the static acceleration on the rate output of the studied gyroscope is suppressed by 91% with the use of the compensation method proposed in this work.

The drawback of the first method is that it requires an additional computation process in the software to compensate the rate output so it cannot reduce the acceleration sensitivity of the gyroscope during the operation.

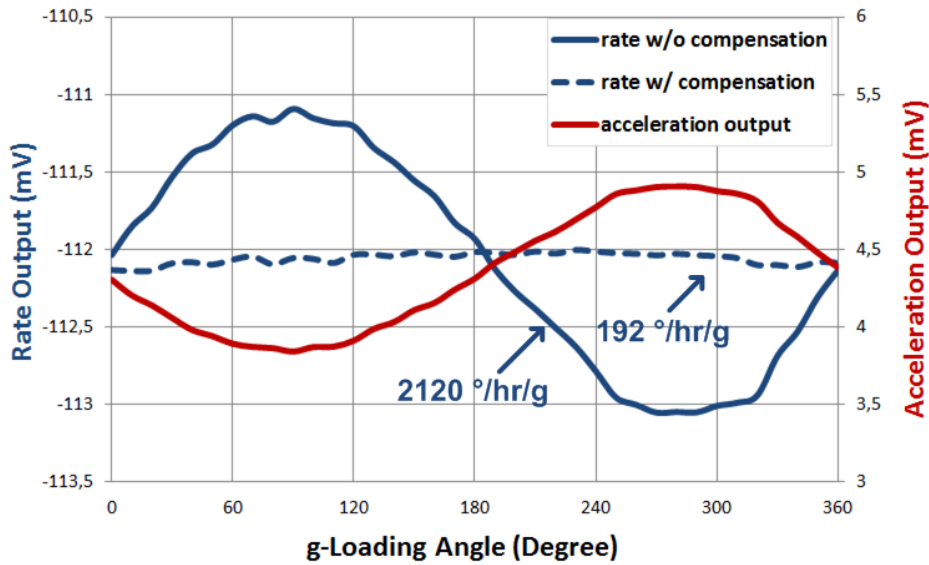


Figure 5.5: Measured (blue one) and compensated (blue-dashed one) rate outputs, and acceleration output (red one) as a function of the rotation angle for the gyroscope (E02) using the compensation Method-1.

In the second phase of the study, the acceleration cancellation circuit is operated in closed loop mode using the gyroscope (H02) in the mismatched condition by applying feedback voltage to the non-inverting inputs of the preamplifiers, as mentioned in 3.5.2 (Method-2). The purpose of this method is to suppress the g-sensitivity of the gyroscope output in operation by generating a counter force to the acceleration force on the sense mode-electrodes. Static acceleration tests for this method are conducted in two steps. Firstly, the rate output data of the gyroscope is collected as a function of the rotation angle without connecting the acceleration cancellation circuit to measure the raw g-sensitivity of the gyroscope. Then, the acceleration cancellation circuit is integrated to the system, and rate output data and acceleration controller output data are collected simultaneously. The acceleration controller output is used to determine the amplitude of the applied acceleration. During the test, the set point of the quadrature cancellation controller is set to 500mV for the proper operation of the acceleration cancellation circuit

Figure 5.6 shows the uncompensated rate output (blue one), compensated rate output (blue-dashed one) and acceleration controller output (red one) as a function of the rotation angle for the gyroscope (H02). Before connecting the acceleration

cancellation circuit, the g-sensitivity of the gyroscope (H02) is measured to be $1216^{\circ}/\text{hr}/\text{g}$. After integrating the acceleration cancellation electronics to the gyroscope system, the g-sensitivity of the gyroscope (H02) is determined to be $416^{\circ}/\text{hr}/\text{g}$. In other words, the effect of the static acceleration on the rate output of the studied gyroscope is suppressed up to 3 times with the use of the acceleration cancellation method proposed in this work. Actually, it is difficult to get a better improvement in the g-sensitivity of the gyroscope using this method because it is theoretically impossible to completely eliminate the effect of the g-sensitivity by this technique as explained in Section 3.5.2 in details. However, the results are still promising for the next step of the acceleration cancellation study. Moreover, the acceleration controller output almost linearly changes with the applied acceleration, and its scale factor is measured to be $13.1\text{mV}/\text{g}$. Therefore, the acceleration acting on the sense axis of the gyroscope can be determined by looking at the output of the acceleration cancellation controller.

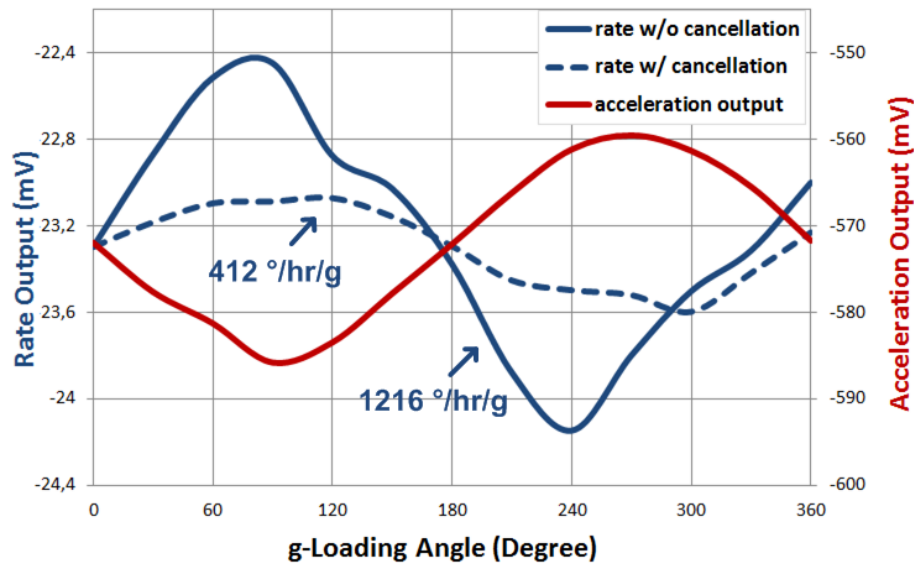


Figure 5.6: Rate outputs without (blue one) and with (blue-dashed one) acceleration cancellation circuit, and acceleration controller output (red one) as a function of the rotation angle for the gyroscope (H02) using the compensation Method-2.

In the third phase of the study, the mechanical structure of the gyroscope is modified and the dedicated acceleration cancellation electrodes are added to the gyroscope. In

this method, the acceleration cancellation circuit is operated in closed loop mode using the gyroscopes (0803) and (1207) in the mismatched condition. In this case, the feedback voltage is applied to the acceleration cancellation electrodes instead of the sense mode electrodes to isolate the operation of the acceleration cancellation circuit from the remaining part of the gyroscope, as mentioned in Section 3.5.3 (Method-3). The purpose of this method is to suppress the g-sensitivity of the gyroscope output in operation by generating a counter force to the acceleration force on the dedicated electrodes. Static acceleration tests are conducted in two steps as in the previous method. Firstly, the rate output data of the gyroscope is collected as a function of the rotation angle without connecting the acceleration cancellation circuit; then, the acceleration cancellation circuit is integrated to the gyroscope system. During the test, the set point of the quadrature cancellation controller is set to 500mV for the proper operation of the acceleration cancellation circuit. These tests are separately conducted for the gyroscopes (0803) and (1207).

Figure 5.7 and Figure 5.10 show the static acceleration test data of the gyroscopes (0803) and (1207), respectively. Without the acceleration cancellation electronics, the g-sensitivity of the gyroscope (0803) is measured to be $1121^{\circ}/\text{hr}/\text{g}$. After integrating the acceleration cancellation electronics to the gyroscope system, the g-sensitivity of the gyroscope (0803) is measured to be $91^{\circ}/\text{hr}/\text{g}$. This test result indicates that there is a significant improvement in the g-sensitivity of the gyroscope (0803) up to 12 times with the use of the acceleration cancellation method proposed in this work. Similarly, the g-sensitivity of the gyroscope (1207) is reduced from $1072^{\circ}/\text{hr}/\text{g}$ to $103^{\circ}/\text{hr}/\text{g}$. Moreover, the acceleration controller outputs of the gyroscopes (0803) and (1207) almost linearly changes with the applied acceleration, and their scale factor are measured to be $411\text{mV}/\text{g}$ and $305\text{mV}/\text{g}$, respectively. In this technique, the outputs of the acceleration cancellation controllers also give information about the acceleration acting on the sense axis of the gyroscopes. Finally, Table 5.3 summarizes the static acceleration test results of the gyroscopes studied in this thesis.

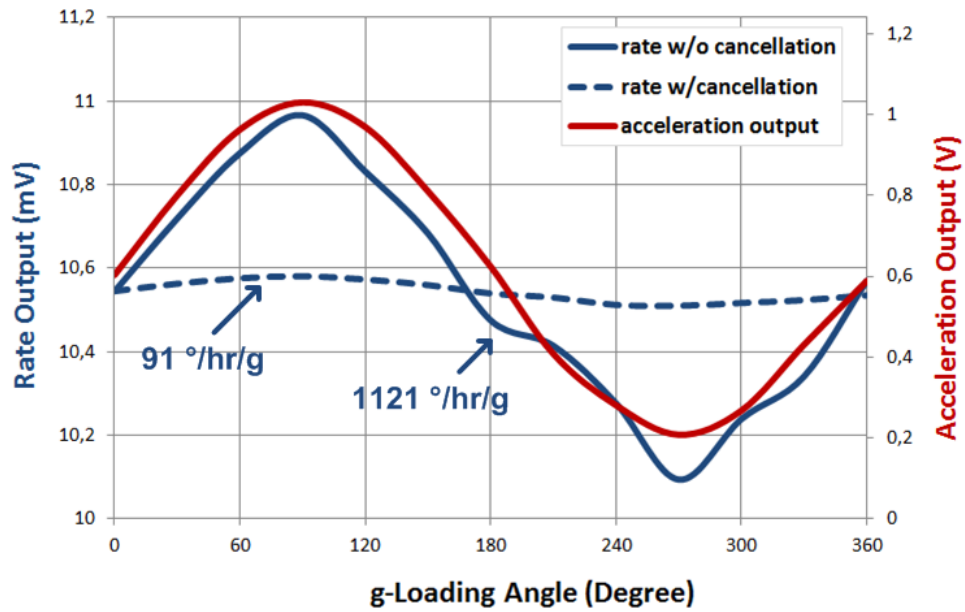


Figure 5.7: Rate outputs without (blue one) and with (blue-dashed one) acceleration cancellation circuit, and acceleration controller output (red one) as a function of the rotation angle for the gyroscope (0803) using the compensation Method-3.

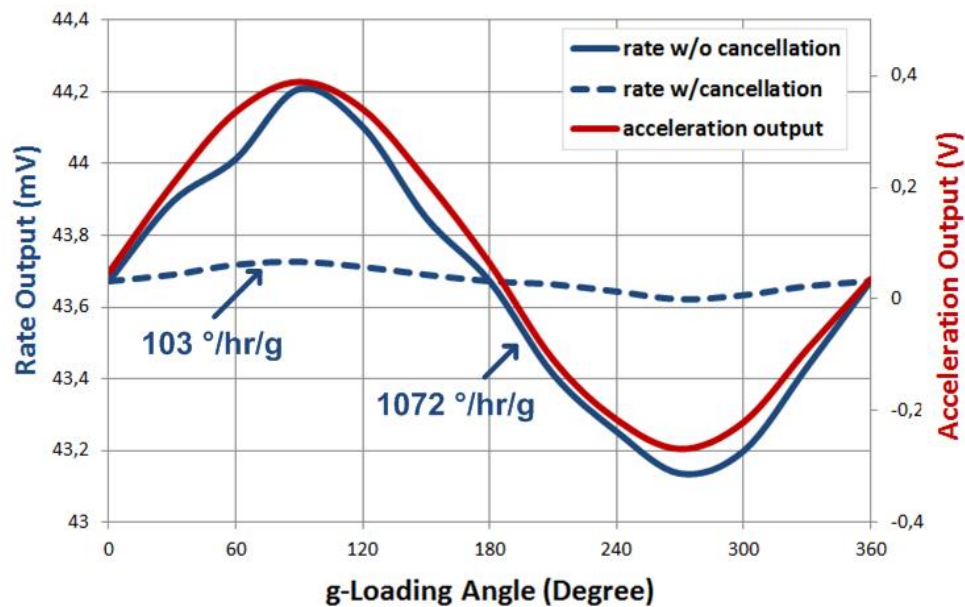


Figure 5.8: Rate outputs without (blue one) and with (blue-dashed one) acceleration cancellation circuit, and acceleration controller output (red one) as a function of the rotation angle for the gyroscope (1207) using the compensation Method-3.

Table 5.3: Summary of the static acceleration test results for the gyroscopes studied in this thesis.

Gyro ID	Acceleration Compensation Method	Quad. Contr. Set Voltage (V)	G-sensitivity w/o Cancel. (°/hr/g)	G-sensitivity w/ Cancel. (°/hr/g)	Scale Factor of Acceleration Output (mV/g)
E02	Method-1	0.5	2120	192	0.5
H02	Method-2	0.5	1216	412	13.1
0803	Method-3	0.5	1121	91	411
1207	Method-3	0.5	1072	103	305

In the concept of this thesis study, the static acceleration tests are performed for the different quadrature controller set voltages to investigate the relation between the quadrature signal level and the g-sensitivity of the gyroscope. As the set voltage of the quadrature controller changes, the amount of the quadrature error in the gyroscope system varies. First, the acceleration controller electronics is not integrated to the gyroscope (1207), and the g-sensitivity is measured for the different quadrature offset voltages. Figure 5.9 show the g-sensitivity of the gyroscope (1207) as a function of the quadrature controller set voltage. As seen in Figure 5.9, the g-sensitivity of the gyroscope increases with increasing quadrature error, indicating that the acceleration sensitivity of the gyroscope is highly depended on the amount of the quadrature error. Moreover, even if the set point of the quadrature controller is adjusted to zero, the gyroscope has a nonzero g-sensitivity.

In the second step of this test, the acceleration cancellation circuit is integrated to the gyroscope system and the static acceleration tests are repeated for the different quadrature signal level. Table 5.4 represents the measured g-sensitivity of the gyroscope (1207) with and without the g-cancellation circuit for the different quadrature set voltages. As seen in Table 5.4, the acceleration cancellation circuit suppresses the g-sensitivity of the gyroscope more effectively as the quadrature signal level increases because the working principle of the g-cancellation circuit is based on the residual quadrature signal. In other words, as the amplitudes of the differential quadrature signals gets larger, the acceleration is sensed more precisely in the g-cancellation circuit. However, the g-sensitivity of the gyroscope also

increases with increasing quadrature error. Therefore, the acceleration cancellation circuit should be operated at the minimum residual quadrature signal level possible to obtain the minimum g-sensitivity for a specific gyroscope.

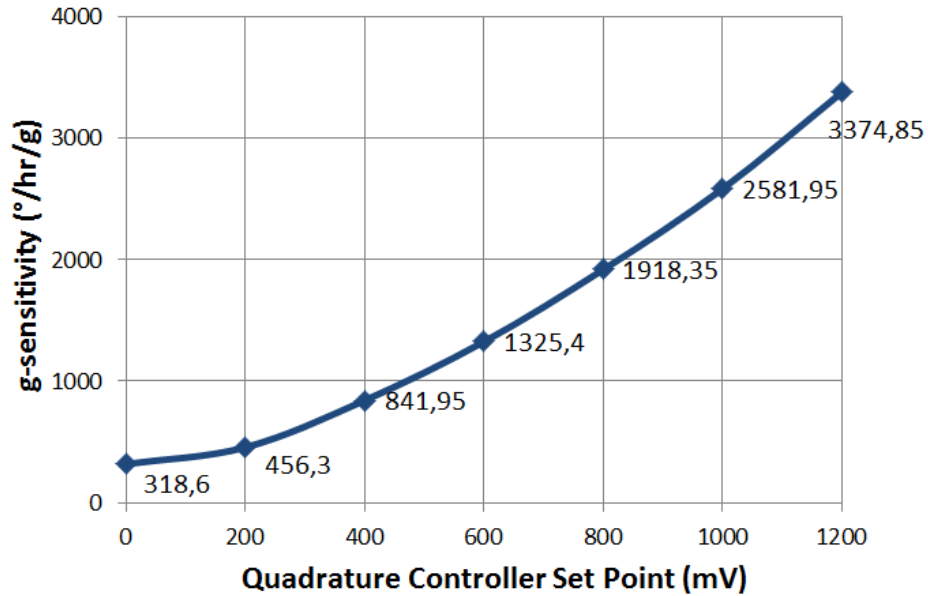


Figure 5.9: G-sensitivity of the gyroscope (1207) as a function of the quadrature controller set voltage using Method-3.

Table 5.4: Measured g-sensitivity of the gyroscope (1207) with and without the acceleration cancellation electronics for the different quadrature set voltages.

Quad. Controller Set Voltage (mV)	Acceleration Compensation Method	G-sensitivity w/o g-cancellation (°/hr/g)	G-sensitivity with g-cancellation (°/hr/g)	Suppression of g-sensitivity (%)
200	Method-3	456,3	61,8	86,4
400	Method-3	841,95	93,2	88,9
600	Method-3	1325,4	119,4	90,1

5.4 Test Results of the Studied MEMS Gyroscopes for Centrifugal Acceleration Tests

In the centrifugal acceleration tests, the angular velocity is applied to the sensor in two different positions on the rate table: centered and off-centered. Figure 5.10 shows (a) the schematic and (b) actual views of the test setup for the centrifugal acceleration test. The sense-axis of the sensor is purely subjected to the Coriolis force in the centered position, whereas both the centrifugal and Coriolis forces act on this axis in the off-centered position. In the off-centered position, the sensor is placed 2 inches (5 cm) far away from the rotation axis. The centrifugal acceleration (a) acting on the gyroscope is dependent on the angular rate (w) and radius (r) by $a=w^2r$.

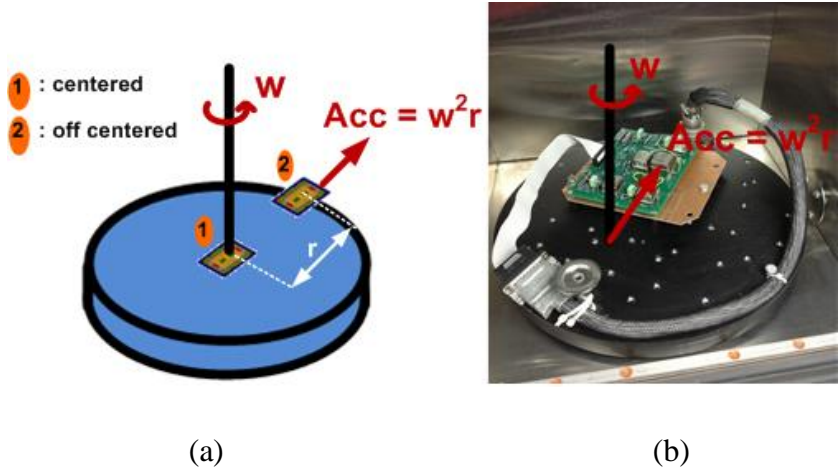


Figure 5.10: (a) Schematic and (b) actual views of test setup for the centrifugal acceleration tests on the rate table.

The purpose of the static acceleration test is to observe the effect of the acceleration on the scale factor of the rate output and to verify the efficiency of the acceleration cancellation electronics under the both the centrifugal and Coriolis acceleration. In this study, the centrifugal acceleration test is performed using the gyroscope (1207) under the mismatch operation. The set point of the quadrature cancellation controller is set to 500mV for the proper operation of the acceleration cancellation circuit.

Firstly, the gyroscope is placed on the center of the rate table without integrating the acceleration cancellation circuit, as shown in Figure 5.10. During the centrifugal

acceleration test, the rate is applied to the system in a range of the $\pm 600^\circ/\text{sec}$. Under this condition, the sense axis of the gyroscope is subjected to only the Coriolis force. In the centered position, the nonlinearity in the scale factor of the rate output is measured to be 0.34%. Then, the gyroscope is placed at 2 inches (5cm) far away from the rotation axis, without connecting the acceleration cancellation circuit to the system. In the off-centered position, the sense axis of the gyroscope is exposed to maximum 0.5g acceleration for the rate signal in a range of the $\pm 600^\circ/\text{sec}$. Under this condition, the nonlinearity in the scale factor of the rate output is measured to be 0.53%. That is, the centrifugal acceleration makes the nonlinearity of the scale factor worse compared to the result in the centered position. Finally, the acceleration cancellation circuit is integrated to the system in the off-centered position, and the same test is repeated. The nonlinearity in the scale factor of the rate output is decreased to 0.36% with the acceleration cancellation electronics in the off-centered position. Figure 5.11 shows the centrifugal acceleration test result for the gyroscope (1207).

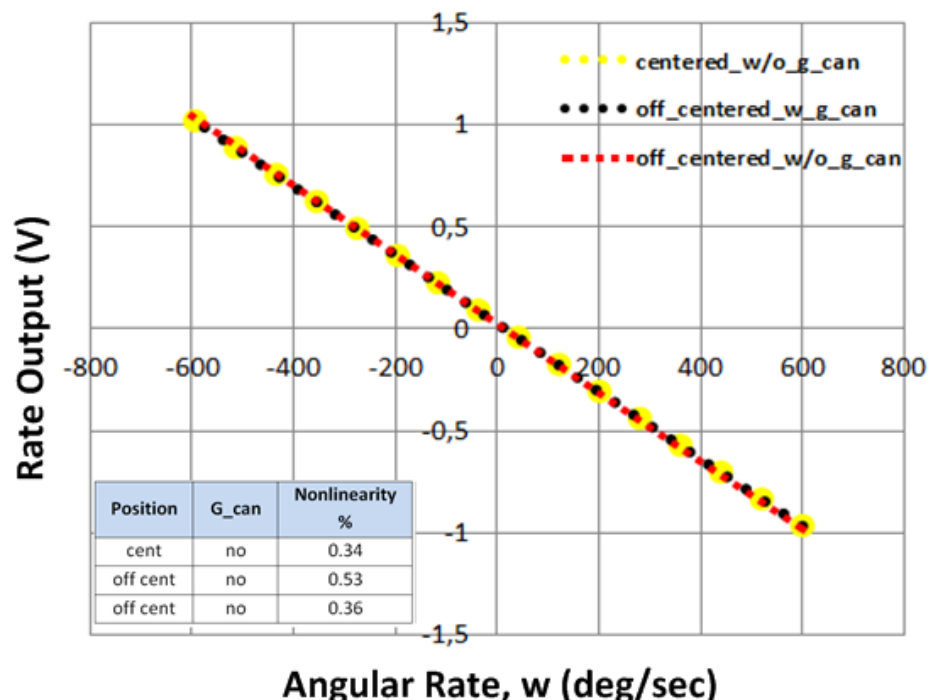


Figure 5.11: Rate output responses of the gyroscope (1207) to the angular rate in the centered and off-centered position on the rate table using the acceleration compensation Method-3.

The centrifugal acceleration test results show that the static acceleration gives rise to a shift in the scale factor of the rate output. Although the centrifugal acceleration causes the nonlinearity of the gyroscope output to change from 0.34% to 0.53%, the g-cancellation circuit suppresses this effect by improving the nonlinearity up to 0.36% for the angular input range of $\pm 600^\circ/\text{sec}$. The maximum acceleration acting on the sense axis of the gyroscope is limited by the test setup conditions. If this test was performed on a rate table having a larger radius, the effect of the centrifugal acceleration on the rate output would be more significant.

5.5 Test Results of the Studied MEMS Gyroscopes for Performance Tests

The Allan Variance tests are performed to determine the bias instability and angle random walk (ARW) performances of the studied MEMS gyroscopes with and without the acceleration control electronics. The purpose of these tests is to determine whether the proposed g-compensation methods deteriorate the performance of the gyroscopes or not. ARW indicates the input referred rate-equivalent white noise, and bias instability shows the minimum detectable angular rotation rate. Figure 5.12 depicts a typical Allan Variance graph. In this graph, the minimum point of Allen deviation refers to the bias instability, and the intersection point of the line with the slope of -0.5 and averaging time of 1 gives the angular random walk.

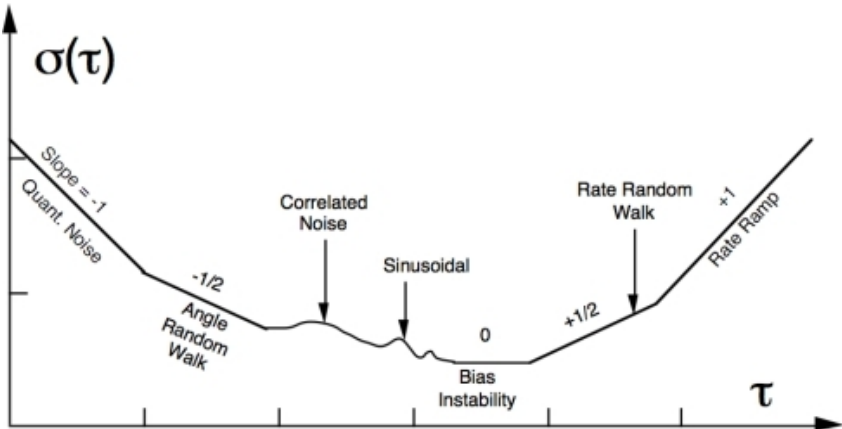


Figure 5.12: A typical Allan Variance graph.

Before the Allan Variance tests, the scale factors of the gyroscopes are measured by the scale factor tests on the rate table. Table 5.5 represents the scale factor of the studied gyroscopes with and without the acceleration cancellation circuits. As seen in Table 5.5, the first (E02) and third (0803 and 1207) methods have no effect on the scale factor of the gyroscope, but the scale factor changes in the second (H02) method.

Table 5.5: Scale factor measurement results of the studied single-mass gyroscopes with and without the acceleration cancellation electronics for the mismatch operation.

Gyro ID	Acceleration Compensation Method	Drive Disp. (μm)	V_{PM} (V)	Scale Factor w/o g-can (mV $^{\circ}$/sec)	Scale Factor w/ g-can (mV $^{\circ}$/sec)
E02	Method-1	4.5	10.5	1.8	1.8
H02	Method-2	4.5	10.5	2.0	1.9
0803	Method-3	4	14.3	1.4	1.4
1207	Method-3	4	14.0	1.8	1.8

In the Allan Variance test, the zero-rate output data of the gyroscope is collected by using the data acquisition card with the sampling frequency of 1 kHz for a certain period. Then, the collected data is evaluated in “AlaVar 5.2” program by doing necessary unit conversion according to the scale factor. Figure 5.13 shows the Allan Variance graph of the gyroscope (1207) with and without the acceleration cancellation circuit. The bias instability and ARW performances of the gyroscope without the acceleration cancellation circuit are found as $1.9^{\circ}/\text{hr}$ and $2^{\circ}/\text{hr}\sqrt{\text{Hz}}$, respectively. When the acceleration cancellation circuit is connected, the bias instability and ARW performances of the same gyroscope are calculated to be $1.8^{\circ}/\text{hr}$ and $1.9^{\circ}/\text{hr}\sqrt{\text{Hz}}$, respectively, which are very close to the previous case. Therefore, the acceleration circuit proposed in Section 3.5.3 has no significant effect on the gyroscope performances as expected.

The unit of ARW can also be converted to $^{\circ}/\sqrt{\text{hr}}$ by dividing the ARW in $^{\circ}/\text{hr}\sqrt{\text{Hz}}$ by 60, which is generally preferred in the literature. It should be also noted that the portion of the Allan Variance plot where the sampling time (τ) smaller than 0.01 sec should be ignored because the cut-off frequency of low pass filter in the force-feedback loop is 100Hz.

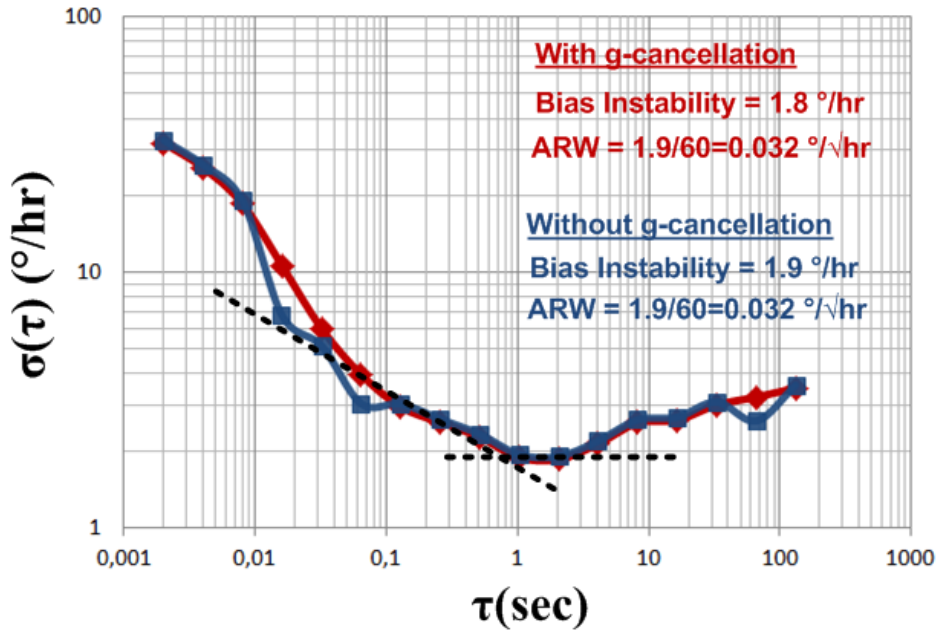


Figure 5.13: Allan Variance graph of the gyroscope (1207) with and without the acceleration cancellation circuit for the mismatch operation.

In this study, the Allan Variance plots are not given for all studied gyroscopes. Instead, the bias instability and ARW performances of the gyroscopes with and without the acceleration compensation methods are represented in Table 5.6. According to the Table 5.6, the first (E02) and third (0803 and 1207) acceleration compensation methods proposed in this work do not significantly affect the bias instability and ARW performances of the gyroscope. However, the second acceleration cancellation method which is implemented on the gyroscope (H02) deteriorates the gyroscope performance.

Table 5.6: ARW and bias instability performances of the single-mass fully decoupled MEMS gyroscopes studied in this thesis.

Gyro ID	Acceleration Compensation Method	Drive Disp. (μm)	w/o G-Cancellation		w/ G-Cancellation	
			ARW ($^{\circ}/\sqrt{\text{hr}}$)	Bias Ins. ($^{\circ}/\text{s}$)	ARW ($^{\circ}/\sqrt{\text{hr}}$)	Bias Ins. ($^{\circ}/\text{s}$)
E02	Method-1	4.5	0.040	2.3	0.038	2.2
H02	Method-2	4.5	0.032	2.2	0.055	4.1
0803	Method-3	4	0.034	2.0	0.035	2.1
1207	Method-3	4	0.031	1.8	0.032	1.9

In the proposed acceleration compensation methods, it is possible to obtain the amplitude of the static acceleration acting along the sense axis of the gyroscopes as mentioned in Section 3.5. Therefore, the low pass filter output of the acceleration sensing circuit in the open loop operation and the acceleration cancellation controller output in the closed loop operation can be used as an accelerometer in the gyroscopes. In this study, the Allan Variance tests are performed for the acceleration outputs of the gyroscope.

Figure 5.14 shows the Allan Variance graph of the acceleration controller output of the gyroscope (1207) for 500mV quadrature offset. The bias instability and velocity random walk (VRW) performances of the acceleration controller output are found as 1.1 mg and $1.2 \text{ mg}/\sqrt{\text{Hz}}$, respectively. The accelerometer performance of the acceleration controller output gets better as the level of the quadrature signal increases.

The Allan Variance plots of the acceleration outputs are not given for all studied gyroscopes. Instead, the bias instability and VRW performances of the acceleration outputs of the studied gyroscopes are represented in Table 5.7. Although these performances are very good for the high-end applications, obtaining data about the amplitude of the acceleration acting along the sense axis of the gyroscope simultaneously in operation is one of the benefits of the proposed acceleration compensation methods.

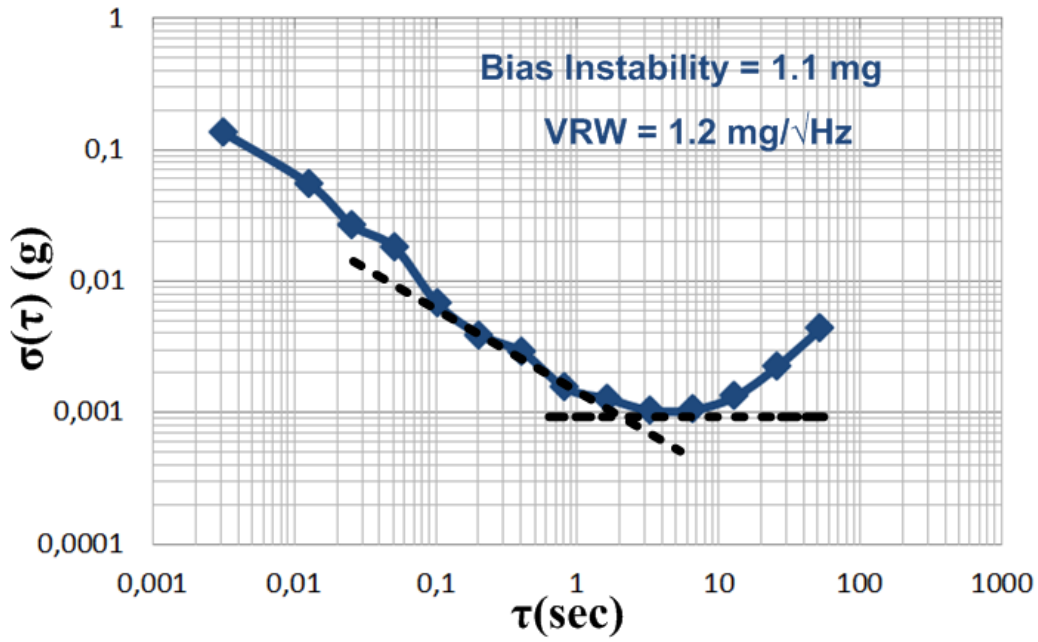


Figure 5.14: Allan Variance graph of the acceleration controller output of the gyroscope (1207).

Table 5.7: ARW and bias instability performances of the acceleration outputs of the single-mass fully decoupled MEMS gyroscopes studied in this thesis.

Gyro ID	Acceleration Compensation Method	Quad. Set Voltage (mV)	Bias Instability (mg)	VRW (mg/ $\sqrt{\text{Hz}}$)
E02	Method-1	500	3.3	4.1
H02	Method-2	500	24.5	53.1
0803	Method-3	500	2.2	3.1
1207	Method-3	500	1.1	1.2

5.6 Summary

This chapter provides the acceleration and performance test results of the studied MEMS gyroscopes. After the characterization of the vacuum packaged gyroscopes mounted on a hybrid glass substrate with the front-end electronics, the drive, sense,

quadrature cancellation and acceleration cancellation controllers are connected to the gyroscope on the test PCB to perform the system level tests.

To verify the efficiency of the proposed acceleration compensation methods, the static and centrifugal acceleration tests are performed. In the static acceleration test, the sense axis of the gyroscope is subjected to the acceleration varying from -1g to 1g by rotating it about its out-of-plane axis on the rotation table. In the centrifugal acceleration test, the gyroscope is exposed to both the Coriolis and centrifugal accelerations on the rate table.

This thesis study is conducted in three phases, in which three different acceleration compensation methods are verified. These methods are not completely different from each other, but an improved version of the previous method is implemented at each step. In the first phase of this study, the acceleration sensing circuit is implemented in the open loop mode using the single-mass gyroscope (E02). In this method, the acceleration acting on the sense axis of the gyroscope is measured by comparing the amplitudes of the residual quadrature signals on the sense mode electrodes. During the acceleration test, the rate and acceleration outputs of the gyroscope are simultaneously collected. Then, assuming a linear relation between the rate output and acceleration output, the effect of the acceleration on the rate output is compensated in the software. By this technique, the sensitivity of the rate output to the static acceleration is reduced from $2120^\circ/\text{hr}/\text{g}$ to $192^\circ/\text{hr}/\text{g}$ for the gyroscope (E02).

In the second acceleration compensation method, the acceleration sensing circuit proposed in the first method is operated in the closed loop mode by applying feedback voltage to the sense mode electrodes from the non-inverting inputs of the sense mode preamplifiers. The purpose of this method is to improve the g-sensitivity of the gyroscope during the operation. This method is verified by using the gyroscope (H02). By this technique, the sensitivity of the rate output of the gyroscope (H02) to the static acceleration is reduced from $1216^\circ/\text{hr}/\text{g}$ to $412^\circ/\text{hr}/\text{g}$. Although changing the input voltage of the sense mode preamplifiers deteriorates the operation of the force-feedback and quadrature cancellation controllers, the acceleration test results are promising for the future study.

In the third acceleration compensation method, the dedicated acceleration cancellation electrodes are utilized instead of the sense mode electrodes to overcome the problems encountered in the second method. This method is verified by using the gyroscopes (0803) and (1207). By this technique, the g-sensitivity of the gyroscope (0803) is reduced from $1121^{\circ}/\text{hr}/\text{g}$ to $91^{\circ}/\text{hr}/\text{g}$ in operation. Similarly, the g-sensitivity of the gyroscope (1207) is reduced from $1072^{\circ}/\text{hr}/\text{g}$ to $103^{\circ}/\text{hr}/\text{g}$.

In this study, the static acceleration test is conducted for the different amount of quadrature error using the gyroscope (1207) to understand the effect the quadrature error on the g-sensitivity of the gyroscope. According to the test results, the g-sensitivity of the gyroscope gets worse as the level of the quadrature signal rises. However, the efficiency of the acceleration cancellation circuit also increases with the increasing quadrature error. Therefore, the acceleration cancellation circuit should be operated with the minimum quadrature signal to obtain the best g-sensitivity performances for a gyroscope.

The centrifugal acceleration test is performed using the gyroscope (1207). It is verified from the test results that the nonlinearity in the scale factor of the gyroscope increases from 0.34% to 0.53% due to the centrifugal acceleration without the acceleration cancellation circuit. The nonlinearity in the scale factor is reduced to 0.36% under the centrifugal acceleration when the acceleration cancellation circuit is integrated to the system.

Finally, the effect of the proposed acceleration cancellation methods on the bias instability and ARW performances of the studied gyroscopes are verified. According to the performance test results, the first and third acceleration compensation methods do not affect the bias and noise performances of the gyroscope; whereas, the second method corrupts the operation of the gyroscope.

CHAPTER 6

CONCLUSIONS AND FUTURE WORK

This work presents the compensation methods for the quasi-static acceleration sensitivity of MEMS gyroscopes and demonstrates the effectiveness of these methods providing experimental data. In the first acceleration compensation method, the amplitude of the static acceleration acting on the sense axis of the gyroscope is measured by comparing the amplitudes of the sustained quadrature signals on the differential sense mode electrodes. In this method, the acceleration sensing circuit is operated in the open loop without using any controller. During the operation, the acceleration and rate output data are simultaneously collected. Then, the measured rate output is corrected by using the measured acceleration output data in the software. This method requires the additional process of the collected data to eliminate the effect of the acceleration from the rate output. In the second method, the acceleration compensation circuit is operated in the closed loop mode to suppress the effect of the acceleration during gyroscope operation. In addition to the circuit proposed in the first method, an integral controller is implemented in the acceleration compensation system, which the feedback voltage is applied to the sense mode electrodes by using the non-inverting inputs of the sense mode preamplifiers. The advantage of this method compared to the first one is that it does not require any additional data process thanks to the closed loop controller. However, this method cannot completely suppress the quasi-static acceleration of the gyroscope due to the working principle of the acceleration sensing electronics. Moreover, changing the voltage of the non-inverting inputs of the preamplifiers destroys the operation of the all other control loops because the operation of the all control circuits starts with the same sense pick signals. Finally, the third acceleration compensation method is implemented, which the feedback voltages are applied to the dedicated acceleration

cancellation electrodes to suppress the g-sensitivity of the gyroscope. This method requires the utilization of the dedicated electrodes in the mechanical design of the gyroscope to balance the acceleration force. But, it overcomes the problem encountered in the second acceleration compensation method. This study mainly focuses on the third acceleration compensation method which gives the best result.

In this study, firstly, the governing equation for the drive mode, sense mode and acceleration cancellation electrodes are derived. Moreover, the effect of the acceleration on the gyroscope operation is analytically examined in details to investigate the source of the acceleration sensitivity. Then, the single-mass fully decoupled gyroscopes including the acceleration cancellation electrodes are designed. FEM simulations are conducted to determine the mode shapes and the corresponding resonance frequencies of the gyroscope. After that, the gyroscopes are fabricated using modified SOG process and wafer level vacuum packaging process. Then, the closed loop drive, force feedback, quadrature and acceleration cancellation controllers are designed and verified using the SIMULINK design software. Each controller packages and sensor package are prepared in the special hybrid packages by creating a modular system, and all control packages are connected with the gyroscope package on a PCB. Finally, the static acceleration, centrifugal acceleration and performance tests are conducted to verify the effectiveness of the proposed acceleration compensation methods.

Results and major achievements of this study are the followings:

1. There are various methods in the literature to minimize the acceleration sensitivity of MEMS gyroscopes; however, these approaches aim to suppress the high frequency acceleration or vibration sensitivity of the gyroscope rather than the static acceleration sensitivity. Moreover, most of the techniques in the literature are based on the mechanical design of the gyroscope. This work proposes a novel acceleration sensing circuit which utilizes the amplitude difference information between the residual quadrature signals on the differential sense-mode electrodes to sense the static acceleration acting on the sense axis of the gyroscope. In the improved version of the acceleration sensing circuit, the static acceleration sensitivity of the gyroscope is reduced in operation by applying feedback voltage to either

sense mode electrodes or additional acceleration cancellation electrodes, for the first time in the literature.

2. Design of the single-mass fully-decoupled gyroscope including the acceleration cancellation electrodes are accomplished to suppress the g-sensitivity of the gyroscope without affecting the operation of the other control loops. The acceleration cancellation electrodes generate a counter force to balance the acceleration force acting on the sense axis. Therefore, it prevents the shift of the sense mode axis due to the static acceleration. The expression of the generated electrostatic force for the acceleration cancellation electrodes and the scale factor of the acceleration cancellation controller are derived. Furthermore, the mode shapes of the gyroscope and the effect of the higher order modes are investigated by performing FEM simulations.
3. The effect of the static acceleration on the gyroscope operation is analytically examined. The expressions for the sense mode, quadrature cancellation and force-feedback electrodes are derived including the effect of the static acceleration. Moreover, the relation between the sense mode springs and g-sensitivity is discussed.
4. Closed loop drive, force feedback, quadrature cancellation, and acceleration cancellation controllers are designed. The closed loop controllers except the acceleration controller are firstly optimized using the open loop characteristics of the loops. In these analyses, the settling time, overshoot and phase margin of the control systems are determined. Then, the closed loop behaviors of the controllers are analyzed by constructing the appropriate SIMULINK models. For each acceleration compensation method, a separate SIMULINK model is designed. All control loops are implemented together to analyze the acceleration compensation circuits. The consistency between the simulation results and derived expressions is verified.
5. The fabrication of the single-mass fully-decoupled gyroscope is done using the modified SOG process. Moreover, the gyroscopes are vacuum packaged

at the wafer level using the wafer level vacuum packaging process. The gyroscopes are vacuum packaged both using the anodic bonding process and eutectic bonding process. The gyroscopes are hermetically sealed and vacuum condition inside the sensors is achieved by the wafer level process. However, although all process steps are optimized during fabrication, wider capacitive gaps and narrower spring widths are observed compared to the design ones after the fabrication. This causes a shift in the designed resonance frequencies and decreases the force generation capability of the drive, quadrature cancellation and acceleration cancellation electrodes.

6. The tested gyroscopes are combined with the front-end electronics using the hybrid packages. Then, the controller modules are integrated to the gyroscope package on the test PCB. The control modules are prepared using the discrete electronics components on the hybrid metal package for low noise measurement. Firstly, the static acceleration tests are conducted using the rotation table for three different acceleration compensation methods. In these tests, the gyroscope system is tested with and without the acceleration compensation circuits to verify the effectiveness of the proposed method. According to static acceleration test results, the g-sensitivity of the gyroscope E02 is suppressed up to 11 times with the use of the first compensation method. Using the second acceleration compensation method, the g-sensitivity of the gyroscope H02 is suppressed up to 3 times. Using the third acceleration compensation method, the g-sensitivities of the gyroscope 0803 and 1207 are suppressed up to 12 times and 10 times, respectively. Moreover, an experimental data is provided to show the relation between the g-sensitivity and quadrature signal level using the gyroscope 1207. Finally, the centrifugal acceleration test is conducted on the gyroscope 1207 with and without the acceleration compensation circuit. By this test, the effect of the centrifugal acceleration on the nonlinearity is observed, and the effectiveness of the acceleration cancellation circuit is proven.
7. Allan variance tests are also performed to determine effects of the proposed acceleration compensation methods on the noise performances of the

gyroscopes. It is experimentally shown that while the first and third acceleration compensation methods have not a significant effect on the bias instability and ARW performances of the gyroscopes, the second method deteriorates these performance values. Moreover, the Allen Variance analysis is done for the acceleration output of the tested gyroscopes which indicates the amplitude of the static acceleration acting on the sense axis of the gyroscope. These outputs can be also used as the accelerometer.

The major achievement of this study is to suppress of the quasi-static acceleration sensitivity of the MEMS gyroscope instantly during the gyroscope operation by using the control electronics rather than employing complex mechanical design. The proposed acceleration compensation methods can be easily applied to any single-mass or mechanically connected double-mass gyroscope without making any significant change in the mechanical design. To further increase the reliability and performance of the gyroscopes, the following research topics should be studied:

1. Vibration or high frequency acceleration sensitivity of the gyroscopes should be minimized. This can be achieved by employing complex mechanical designs which are immune to the vibration or shock. Moreover, special suspended beams functioning as the mechanical low pass filter can be placed under the gyroscope structure to eliminate the effect of the vibration.
2. Temperature compensation should be done for the gyroscope output to achieve better gyro performances. The rate output of the gyroscope drifts with temperature in time. If the temperature dependency of the gyroscope output is decreased, the bias and noise performances of the gyroscope can be improved.
3. The control electronics of the gyroscope should be implemented in the digital domain. The digital control system provides flexibility in the controller design. If the digital control system is implemented in a single chip, the overall size of the control electronics significantly reduced.

REFERENCES

- [1] S. Nasiri, M. Lim, and M. Housholder, "A Critical Review of the Market Status and Industry Challenges of Producing Consumer Grade MEMS Gyroscopes," Available online: <http://invensense.com/mems/whitepapers> (accessed on 5 September 2014).
- [2] E. Tatar, S. E. Alper, and T. Akin, "Effect of Quadrature Error Compensation and Corresponding Effects on the Performance of Fully Decoupled MEMS Gyroscopes," *IEEE/ASME Journal of Micro Electro Mechanical Systems*, Vol. 21, No.3, pp. 656-667, June 2012.
- [3] S. Sonmezoglu, S. E. Alper, and T. Akin, "High Performance Automatic Mode Matched MEMS Gyroscope with an Improved Thermal Stability of the Scale Factor," *The 17th International Conference on Solid-State Sensors, Actuators and Microsystems (TRANSDUCERS 2013)*, pp. 2519-2522, Barcelona, Spain, June 2013.
- [4] H. Weinberg, "Gyro Mechanical Performance: The Most Important Parameter," *Tech. art., Analog Devices*, Sep. 2011.
- [5] K. Azgin, "High Performance MEMS Gyroscopes," *M.Sc. Thesis*, Middle East Technical University, February 2007.
- [6] S. E. Alper, "MEMS Gyroscopes for Tactical-Grade Inertial Measurement Applications," *Ph.D. Dissertation*, Middle East Technical University, September 2005.
- [7] R. I. Shakoor, S. A. Bazaz, M. Burnie, Y. Lai, and M. M. Hasan, "Electrothermally Actuated Resonant Rate Gyroscope Fabricated Using the MetalMUMPs," *Journal of Microelectronics*, Vol. 42, No.4, pp. 585-593, 2011.
- [8] N. Yazdi, F. Ayazi, and K. Najafi, "Micromachined Inertial Sensors," *Proceedings of the IEEE*, Vol. 86, No. 8, pp.1640-1659, August 1998.
- [9] IEEE Standard for Inertial Sensors Terminology, *IEEE Std 528-2001*, November 2001.
- [10] S. Nasiri, "A Critical Review of MEMS Gyroscopes Technology and Commercialization Status," Available online: <http://invensense.com/mems/whitepapers> (accessed on 7 September 2014).

- [11] C. Acar, and A. M. Shkel, "MEMS Vibratory Gyroscopes: Structural Approaches to Improve Robustness," *Springer Publisher*, 2009.
- [12] P. Greiff, B. Boxenhorn, T. King, and L. Niles, "Silicon Monolithic Micromechanical Gyroscope," 6th International Conference of Solid-State Sensors and Actuators, pp. 966-968, San Francisco, CA, June 1991.
- [13] J. Bernstein, S. Cho, A. T. King, A. Kourepenis, P. Maciel, and M. Weinberg, "A Micromachined Comb-Drive Tuning Fork Rate Gyroscope," Proc. of IEEE Micro Mechanical Systems Workshop, pp. 143-148, Fort Lauderdale, FL, February 1993.
- [14] M. W. Putty and K. Najafi, "A Micromachined Vibrating Ring Gyroscope," *Solid-State Sensor and Actuator Workshop*, Hilton Head Island, SC, USA, pp. 213-220, Hilton Head Island, SC, USA, June 1994.
- [15] A. Selvakumar and K. Najafi, "High Density Vertical Comb Array Microactuators Fabricated Using a Novel Bulk/Poly-silicon Trench Refill Technology," *Solid-State Sensor And Actuator Workshop*, Hilton Head Island, pp. 138-141, SC, USA, 1994.
- [16] I. D. Hopkin, "Vibrating Gyroscopes (Automotive Sensors)," *IEEE Colloquium on Automotive Sensors*, pp. 1-4, Solihull, UK, September 1994.
- [17] F. Ayazi and K. Najafi, "A HARPSS Polysilicon Vibrating Ring Gyroscope," *Journal of Microelectromechanical Systems*, Vol. 10, No. 2, pp. 169-179, June 2001.
- [18] M. Lutz, W. Golderer, J. Gerstenmeier, J. Marek, B. Maihofer, S. Mahler, H. Munzel, and U. Bischof, "A Precision Yaw Rate Sensor in Silicon Micromachining," *I Tech. Dig. 9th Int. Conf. Solid-State Sensors and Actuators (Transducers'97)*, pp. 847-850, Chicago, IL, June 1997.
- [19] R. Voss, K. Bauer, W. Ficker, T. Gleissner, W. Kupke, M. Rose, S. Sassen, J. Schalk, H. Seidel, and E. Stenzel, "Silicon Angular Rate Sensor for Automotive Applications with Piezoelectric Drive and Piezoresistive Read-out," *Tech. Dig. 9th Int. Conf. Solid-State Sensors and Actuators (Transducers'97)*, pp. 847-850, Chicago, IL, June 1997.

- [20] D. Karnick, G. Ballas, L. Koland, M. Secord, T. Braman, and T. Kourepenis, "Honeywell Gun-Hard Inertial Measurement Unit (IMU) Development," *Position Location and Navigation Symposium, PLANS 2004*, pp. 49 - 55, April 2004.
- [21] K. Tanaka, Y. Mochida, S. Sugimoto, K. Moriya, T. Hasegawa, K. Atsuchi, and K. Ohwada, "A Micromachined Vibrating Gyroscope," *Proceedings of the International Conference on Micro Electro Mechanical Systems*, pp. 278-281, Netherlands, January 1995.
- [22] H. Luo, X. Zhu, H. Lakdawala, L. R. Carley, and G. K. Fedder, "A Copper CMOS-MEMS Z-Axis Gyroscope," *Proceedings of the International Conference on Micro Electro Mechanical Systems*, pp. 631-634, Las Vegas, January 2001.
- [23] J. A. Geen, S. J. Sherman, J. F. Chang, and S. R. Lewis, "Single-Chip Surface-Micromachining Integrated Gyroscope with 50 deg/hour Root Allan Variance," *IEEE International Conference on Solid-State Circuits*, pp. 426-427, San Francisco, CA, Feb. 2002.
- [24] H. Xie and G. K. Fedder, "Fabrication, Characterization, and Analysis of a DRIE CMOS-MEMS Gyroscope," *IEEE Sensors Journal*, Vol. 3, No. 5, pp. 622-631, 2003.
- [25] C. Acar, and A. Shkel, "Inherently Robust Micromachined Gyroscopes with 2-DOF Sense-Mode Oscillator," *Journal of Microelectromechanical Systems*, Vol. 15, No. 2, pp. 380-387, 2006.
- [26] A. A. Trusov, A. R. Schofield, and A. M. Shkel, "New Architectural Design of a Temperature Robust MEMS Gyroscope with Improved Gain-Bandwidth Characteristics," *Hilton Head Work-shop in Solid State Sensors, Actuators, and Microsystems*, Jun. 1-5, 2008.
- [27] M. F. Zaman, A. Sharma, Z. Hao, and F. Ayazi, "A Mode-Matched Silicon-Yaw Tuning-Fork Gyroscope With Subdegree-Per-Hour Allan Deviation Bias Instability," *Journal of Microelectromechanical Systems*, Vol. 17, No. 6, pp.1526-1536, December 2008.

- [28] Ajit Sharma, Mohammad Faisal Zaman, and Farrokh Ayazi, "A Sub 0.2° /hr Bias Drift Micromechanical Gyroscope With Automatic CMOS Mode-Matching," *IEEE Journal of Solid State Circuits*, Vol. 44, No. 5, pp.1593-1608, May 2009.
- [29] B. Chaumet, B. Leverrier, C. Rougeot, S. Bouyat, "A New Silicon Tuning Fork Gyroscope for Aerospace Applications," *Symposium Gyro Technology*, pp. 1.1-1.13, Karlsruhe, Germany, September 2009.
- [30] S. Sonmezoglu, "A High Performance Automatic Mode-Matched MEMS Gyroscopes," *M.Sc. Thesis*, Middle East Technical University, September 2012.
- [31] S. Sonmezoglu, H. D. Gavcar, K. Azgin, S. E. Alper, and T. Akin, "Simultaneous Detection of Linear and Coriolis Accelerations on a Mode-Matched MEMS Gyroscope," *The 27th IEEE International Conference on Micro Electro Mechanical Systems (MEMS 2014)*, pp. 32-35, San Francisco, U.S.A., January 2014.
- [32] M. M. Torunbalci, E. Tatar, S. E. Alper, and T. Akin, "Comparison of Two Alternative Silicon-on-Glass Microfabrication Processes for MEMS Inertial Sensors," *Euroensors XXV*, Athens, Greece, September 2011.
- [33] M. M. Torunbalci, S. E. Alper, and T. Akin, "Wafer Level Hermetic Encapsulation of MEMS Inertial Sensors using SOI Cap Wafers with Vertical Feedthroughs," *IEEE Int. Symposium on Inertial Sensors and Systems (ISISS'14)*, pp. 1-2, Laguna Beach, California, USA, February 2014.
- [34] J. A. Geen, "Progress in Integrated Gyroscopes," *Proceedings position, location, and navigation symposium (PLANS)*, pp.1-6, Monterey, 2004.
- [35] M. F. Zaman, A. Sharma, F. Ayazi, "High Performance Matched-mode Tuning Fork Gyroscope", *The 19th IEEE International Conference on Micro Electro Mechanical Systems (MEMS 2006)*, pp. 66-69, Istanbul, Turkey., January 2006.
- [36] H. Weinberg, "Gyro Mechanical Performance: The Most Important Parameter," *Tech. art.*, Analog Devices, Sep. 2011.
- [37] A. R. Schofield, A. A. Trusov, and A.M. Shkel, "Multi-degree of Freedom Tuning Fork Gyroscope Demonstrating Shock Rejection," *IEEE Sensors*, pp.120-123, Oct. 2007.

- [38] K. Azgin, Y. Temiz, and T. Akin, "An SOI-MEMS Tuning Fork Gyroscope with Linearly Coupled Drive Mechanism," *The 20th IEEE International Conference on Micro Electro Mechanical Systems (MEMS 2007)*, pp. 607-610, Kobe, Japan, January 21-25, 2007.
- [39] S. W. Yoon, S.W. Lee, and K. Najafi, "Vibration-Induced Errors in MEMS Tuning Fork Gyroscopes," *Sensor and Actuators A: Physical*, Vol. 180, pp. 32-34, Jun. 2012.
- [40] S. W. Yoon, "Vibration Isolation and Shock Protection for MEMS," *Ph.D. Dissertation*, Uni. of Michigan, 2009.
- [41] Analog Devices, "ADXRS450 High Performance, Digital Output Gyroscope," *Datasheet*, 2011.
- [42] E. Tatar, "Quadrature Error Compensation and Its Effects on the Performance of Fully Decoupled MEMS Gyroscopes," *M.Sc. Thesis*, Middle East Technical University, September 2010.
- [43] S. E. Alper, K. Sahin, and T. Akin, "An Anaysis to Improve Stability of Drive-Mode Oscillations in Capacitive Vibratory MEMS Gyroscopes," *The 22nd IEEE International Conference on Micro Electro Mechanical Systems (MEMS 2009)*, pp. 817-820, Sorrento, Italy, Jan. 2009.
- [44] B. Eminoglu, S. E. Alper, and T. Akin, "An Optimized Analog Drive-Mode Controller for Vibratory MEMS Gyroscopes," *Euroensors XXV*, Athens, Greece, September 2011.
- [45] E. Tatar, M. M. Torunbalci, S. E. Alper, and T. Akin, "A Method and Electrical Model for the Anodic Bonding of SOI and Glass Wafers," *The 25th IEEE International Conference on Micro Electro Mechanical Systems (MEMS 2012)*, pp. 68-71, Paris, France, Jan. 29-Feb.2, 2012.
- [46] M. M. Torunbalci, S. E. Alper, and T. Akin, "A Method of Fabricating Vacuum Packages with Vertical Feedthroughs in a Wafer Level Anodic Bonding Process," *Euroensors XXVIII*, Brescia, Italy, September 2014.

[47] S. E. Alper, M. M. Torunbalci, and T. Akin, "Method of wafer level hermetic packaging with vertical feedthroughs," PCT/TR2013/000298, September 2013.